New Techniques for Time-Reversal-Based Ultra-wideband Microwave Pulse Compression in Reverberant Cavities

Zachary Benjamin Drikas

Dissertation submitted to the faculty of the Virginia Polytechnic Institute and State University in partial fulfillment of the requirements for the degree of

Doctor of Philosophy
In
Electrical Engineering

Sanjay Raman, Chair
T. Charles Clancy
Guoqiang Yu
Steven Ellingson
Jonathan Black

Sept 30th, 2020
Arlington, Virginia

Keywords: Ultra-short pulse (USP), pulse compression, ultra-wideband (UWB), time-reversal, reconfigurable cavity, dispersive cavity

New Techniques for Time-Reversal-Based Ultra-wideband Microwave Pulse Compression in Reverberant Cavities

Zachary Benjamin Drikas

ABSTRACT

Generation of high-peak power, microwave ultra-short pulses (USPs) is desirable for ultra-wideband communications and remote sensing. A variety of microwave USP generators exist today, or are described in the literature, and have benefits and limitations depending on application. A new class of pulse compressors for generating USPs using electromagnetic time reversal (TR) techniques have been developed in the last decade, and are the topic of this dissertation. This dissertation presents a compact TR microwave pulse-compression cavity that has ultra-wide bandwidth (5 GHz – 18 GHz), and employs waveguide feeds for high-peak power output over the entire band. The system uses a time-reversal-based pulse compression scheme with one-bit processing (OBTR) to achieve high compression gain. Results from full-wave simulations are presented as well as measurements showing compression gain exceeding 21.2 dB, 22% efficiency, and measured instantaneous peak output powers reaching 39.2 kW. These are all record results for this type of pulse compressor. Additionally presented is new analysis of variation in compression gain due to impulse response recording time and bandwidth variation, new experimental work on the effect of mode stirrer position on compression gain, and a novel RF switch-based technique for reducing time-sidelobes while using OBTR. Finally, a new technique is presented that uses a reverberant cavity with only one feed connected to an ultra-wideband circulator (6.5 GHz to 17 GHz) to perform TRPC. Prior to this work, TRPC has only been demonstrated in electromagnetics using two or more feeds and a reverberant cavity acting as the time-reversal mirror. This new 1-port technique is demonstrated in both simulation and measurement. The proposed system achieves up to a measured 3 dB increase in compression gain and increased efficiency. Also, a novel application of the random coupling model (RCM) to calculate compression gain is presented. The cavity eigenfrequencies are modeled after eigenvalues of random matrices satisfying the Gaussian orthogonal ensembles (GOE) condition. Cavity transfer functions are generated using Monte Carlo simulations, and used to compute the compression gains for many different cavity realizations.

New Techniques for Time-Reversal-Based Ultra-wideband Microwave Pulse Compression in Reverberant Cavities

Zachary Benjamin Drikas

GENERAL AUDIENCE ABSTRACT

Generation of high-peak power, microwave ultra-short pulses (USPs) is desirable for ultra-wideband communications and remote sensing. A variety of microwave USP generators exist today, or are described in the literature, and have benefits and limitations depending on application. A new class of pulse compressors for generating USPs using electromagnetic time reversal (TR) techniques have been developed in the last decade, and are the topic of this dissertation. This dissertation presents a compact TR-based microwave pulse-compression cavity that has unique features that make it optimal for high-power operations, with results from simulations as well as measurements showing improved performance over other similar cavities published in the literature with a record demonstrated peak output power of 39.2 kW. Additionally, new analysis on the operation and optimization of this cavity for increased performance is also presented. Finally, a new technique is presented that uses a cavity with only one feed that acts as both the input and output. This 1-port technique is demonstrated in both simulation and measurement. The proposed system achieves a two-times increase in compression gain over its 2-port counterpart. In conjunction with these measurements and simulations, a novel technique for predicting the performance of these cavities using Monte Carlo simulation is also presented.

To my wife and son, Jennifer Sue Curry and Benjamin Oliver Curry-Drikas

Acknowledgements

The work in this dissertation was sponsored by the U.S. Naval Research Laboratory (NRL)

First, and most importantly, I am thankful to my family. Thank you for your constant and continuing support, inspiration, love, and encouragement during this long journey.

Also, I would like to express my sincere appreciation and gratitude to my advisor, Dr. Sanjay Raman. Thank you very much for giving me the opportunity to earn my Ph.D., and thank you for all your help, advice, and guidance during my studies. As well, I would like to thank my advisory committee members for their help and support.

Also, I am deeply grateful to my colleagues at NRL, Dr. Bisrat Addissie, Mr. Victor Mendez, Dr. Tim Andreadis, and Mr. Mark Gengenbach for all of their help and insightful discussion over the years.

Table of Contents

Acknowledgements ..... **v**

List of Figures ..... **viii**

List of Tables ..... **xv**

List of Abbreviations ..... **xvi**

Chapter 1 - Introduction **1**

1.1 - Motivation and State-of the Art 1

1.2 - What is an Ultrashort Pulse? 2

1.3 - Ultra-wideband Microwave Pulse Compression using Time-Reversal Techniques 7

1.4 - Dissertation Organization and Objectives 7

Chapter 2 – Time Reversal Theory **9**

2.1 - Early Experiments in Communications and Acoustics 9

2.2 - Electromagnetic Time-Reversal 11

2.3 - Time Reversal for Wideband Electromagnetic Pulse Compression in Cavities 13

2.4 - Summary 16

Chapter 3 - A Compact High-gain, High-power Ultra-wideband Pulse Compressor **17**

3.1 - Cavity Design and Simulation 17

3.2 - Cavity Fabrication and Experimental Set-up 21

3.3 - Measurement of the Cavity Compression Gain 24

3.4 - Analysis of Cavity Efficiency from Simulated and Measured Results 26

3.5 - Investigation of the Effect of Variation of IR Recording Time and Signal Bandwidth on Compression Gain 28

3.6 - Cavity Geometry Optimization 31

3.7 - Summary 34

Chapter 4 - Cavity Input-Output Fidelity and Time-Sidelobe Reduction **35**

4.1 - Time-Sidelobe Reduction for OBTR 38

4.2 - Summary 40

Chapter 5 - Pulse Compression using Time Reversal Techniques in a Single-Port Cavity **41**

5.1 - Motivation for Single-Port Pulse Compression 43

5.1.1 - On the Potential for Increased Power by Using One Port for both Transmitting and Receiving *43*
5.1.2 - On the Increase in Loaded Quality Factor from Removing the Second Port *45*
5.2 - Compression Gain Modeling 48
5.2.1 - Cavity Transfer Function Modeling using the Random Coupling Model *48*
5.2.2 - Modeling Compression Gain *52*
5.3 - Compression Gain Simulations For 1-Port And 2-Port Cavities 57
5.4 - Pulse Compression Measurements 63
5.5 - Analysis and Discussion 67
5.5.1 - The Statistical Nature of Predictions of Compression Gain *67*
5.5.2 - Cavity Efficiency *69*
5.6 - Summary 70
Chapter 6 - Conclusions and Future Work 72
6.1 - Conclusions 72
6.2 - Future Work 75
Appendix A - Multiple-Post Height Optimization 76
A.1 - Genetic Algorithms for Post Height Optimization 76
A.2 - Fabrication of Post-Grid Optimization Apparatus 77
Appendix B - Further Measurements for Time-sidelobe Reduction 80
References 85

List of Figures

Figure 1-1. Trade space of bandwidth and peak power for different USP sources. Time-reversal-based ultra-wideband pulse compression cavities have potential to enable pules generation in the high-bandwidth/high-peak power regime. Legend for USP generator enabling technology: PCSS = Photoconductive Solid State Switch; SRD = Step Recovery Diode; DSRD = Drift Step Recovery Diode; Transistor = Avalanche Transistor; AWG = Arbitrary Waveform Generator; LP TR = Low Power Time-Reversal; Super Lum = Super Luminal; Super Rad = Superradiant; FID = Fast Ionization Dynistor. 2

Figure 1-2. Examples of narrowband waveforms. (a) An approximated continuous wave (CW) waveform and (b) its spectrum (an approximated single frequency). (c) A narrowband waveform and (d) its spectrum. 5

Figure 1-3. Examples of wideband and ultra-wideband waveforms. (a) A damped sinusoid and its spectrum. (b) A Gaussian impulse and its spectrum. (c) A Gaussian monocycle and its spectrum. (d) A sinc (cardinal sinus) pulse and (e) its spectrum. 6

Figure 2-1. TR is simply the reversing of a waveform in time, $(t \longrightarrow -t)$. 9

Figure 2-2. Block diagram of time-reversal system adapted from B. P. Bogert's 1957 paper [24]. An image or impulsive waveform, $f(t)$, is transmitted on a network with transfer function, $H(\omega)$, to produce the response, $h(t)$. This response is time-shifted and time-reversed, and retransmitted over the network resulting in a reconstructed image or impulse, $y(t)$, with, ideally, zero phase. 10

Figure 2-3. Iterative TR Process adapted from Fink, Prada, and Casserau [25]. I the first step of the iterative process, the transducers transmit identical signals to two targets of different size. The backscattered signals are recorded, time-reversed and re-transmitted. After several iterations the response of the smaller scatter is virtually non-existent. 10

Figure 2-4. Wideband time-reversal experiment using multiple antennas in arrays for both the time-reversal mirror and receiver (adapted from [33]). 12

Figure 2-5. 'Leaky' reverberation chamber experimental setup for TR compression of electromagnetic waves in space (adapted from [34]). 12

Figure 2-6. (a) Following the signal flow clockwise from the top left: The low peak power impulse, *f*(*t*), is transmitted through a UWB wideband amplifier into the dispersive cavity

and the impulse response is recorded on an oscilloscope. Then, the IR is time-reversed, normalized, and retransmitted through the UWB amplifier into the PC cavity to obtain the reconstructed impulse. (b) shows the one-bit TR signal, sign[$h(-t)$], that may be used in place of $h(-t)$ to obtain higher compression gain (in practice the large bandwidth that produces the 'square wave' would be filtered by the PC feed to the system bandwidth of 13 GHz.).....14
Figure 3-1. (a) Pulse compression cavity with waveguide feeds and cylindrical scatterer, and (b) reflection coefficient (S11) of the cavity feed from 5 - 18 GHz. 18
Figure 3-2. (a) Cavity excitation impulse is a sinc function with flat bandwidth from 5 – 18 GHz. Pulse width is ~35 ps at FWHM. (b) Simulated impulse reconstruction in PEC cavity showing reconstructed impulse at ~965 ns. 19
Figure 3-3. Tradeoff study of cavity material and impulse response length versus compression gain. 20
Figure 3-4. (a) The pulse compressor cavity is machined out of solid block of aluminum for rigidity to reduce perturbations due to deformation of the cavity, as would happen with thin-plate sides. (b) Pulse compressor (dispersive cavity) outer dimensions are 67 cm x 47 cm x 6 cm with a dual-directional coupler on the input and an attenuation shunt on the output for increased dynamic measurement range on the oscilloscope.....22
Figure 3-5. Experimental setup and signal flow diagram. The attenuation shunt is used to switch attenuation for low output power when measuring impulse response to more attenuation for high output power when measuring one-bit TR output signal. 23
Figure 3-6. OBTR process and pulse reconstruction: (a). USP as programmed in the AWG; (b). Amplified signal transmitted into the cavity and the to-scale impulse response (inset shows zoomed in signals); (c). Spectra of signals in a) and b); (d). TR signal and OBTR signal (filtered to 13 GHz BW) sent to AWG; (e). Amplified OBTR signal and reconstructed impulse response showing 21.2 dB of gain and a peak output voltage of 1400 V; (f) Spectra of OBTR and Reconstructed Impulse. 25
Figure 3-7. (a) Reflectance, absorptance, and transmittance of the pulse compression cavity as a function of frequency for simulate, (b) and measured aluminum cavities. 27
Figure 3-8. Compression gain as a function of *increasing* excitation signal bandwidth. Keeping the *start* frequency at 5 GHz, the *stop* frequency is varied from 5.1 GHz to 18 GHz in 100

MHz increments, and the pulse compression gain is noted. Impulse response length was 1 μs. 29
Figure 3-9. Compression gain as a function of *decreasing* excitation signal bandwidth. Keeping the *stop* frequency at 18 GHz, the *start* frequency is varied from 5.1 GHz to 18 GHz in 100 MHz increments, and the pulse compression gain is noted. Impulse response length was 1 μs. 30
Figure 3-10. Compression gain as a function of *increasing* impulse response recording time. Keeping the bandwidth constant (5 GHz – 18 GHz), the record time is varied from 10 ns to 6 μs in 10 ns increments. 30
Figure 3-11. Compression Gain over 200 different stirrer positions. Mode stirrer is automatically controlled using MATLAB and a stepper motor such that the entire pulse compression process is accomplished through automated equipment control. Gain is seen to vary from 17.6 dB to 19.7 dB with a mean of 18.9 dB. Inset shows single-paddle mode stirrer attached to shaft below lid. 32
Figure 3-12. Compression Gain over 200 different stirrer positions at new stirrer location. Gain is seen to vary from 17.6 dB to 21 dB with a mean of 19.6 dB 33
Figure 4-1. Original waveform, excitation waveform, and reconstructed waveform seen overlaid on each other (top) from the measured cavity. There is good fidelity between the reconstructed impulse and the excitation impulse, but there are certain features of the original impulse sent to the AWG that differ (bottom). 36
Figure 4-2. Excitation impulse, OBTR reconstructed impulse from simulated aluminum cavity, OBTR reconstructed impulse from simulated PEC cavity, and TR reconstructed impulse from simulated PEC cavity (top). Time-sidelobes for all cases in top (bottom left). Zoom in of reconstructed impulse for all cases in top (bottom right). 37
Figure 4-3. Diagram of switch state for OBTR sidelobe reduction. During the interrogation run, switch becomes reflective after forward switching time, $tswF$. During the reconstruction run it remains reflective for the reverse switching time, $tswR$, and becomes 50 ohms for the last period of length $tswF$. 39
Figure 4-4. Impulse response when PIN diode switch was closed for 990 ns out of 1000 ns showing more energy than the impulse response with no PIN-diode switch open the for the whole 1000 ns. 39

Figure 4-5. Time-sidelobe reduction is evident in the inset during the 990 ns period where the switch was closed, and the reconstruction begins after this time. Reconstruction truncation due to PIN-diode switch is also evident and peak power should be 10s of kW, not 10s of W.....40
Figure 5-1. 2-port cavity TRPC process using a dual-feed cavity architecture. 42
Figure 5-2. A 2-port cavity TRPC process using a single-feed and aperture architecture with and external antenna. 42
Figure 5-3. A 1-port TRPC process using a cavity with a single port and a circulator. 44
Figure 5-4. A dispersive, reverberant cavity with two ports. Due to identical transmit and receive locations, the coherent addition of a portion of the transmitted waves at port 1 leads to a doubling in normalized power. Adapted from [17]. 45
Figure 5-5. (a) Frequency dependent loaded quality factor, Ql, from 5 GHz to 18 GHz for 1-port and 2-port cavities calculated using (6). (b) M/Qp for 1-port and 2-port cavities plotted with $1/Qu$ for (6).....47
Figure 5-6. $Z11rad$ of cavity directly simulated in CST full-wave solver. Three walls of the cavity have been removed and replaced with a PML boundary. The lid remains in the simulation, and is only removed here to show detail.....50
Figure 5-7. a) $\boldsymbol{S11}$ of cavity simulated in CST. (b) Inverse Fourier transform (time-domain response of cavity) used to find the time-gating length, $tgate$ for use in finding $\boldsymbol{R}rad$ (Gating time (box) is determined to be 5 ns.).....50
Figure 5-8. $\boldsymbol{Z11}$ of cavity simulated in CST and $Zrad$ as determined using the TGM. 51
Figure 5-9. (a) Radiation resistance, $R11\mathrm{rad}$ and (b) radiation reactance, $X11rad$, determined by both the time gating and the PML simulation methods. 51
Figure 5-10. (a) Excitation signal and (b) it's spectrum for both the compression gain modeling in Section 5.2.2 and the simulations in this section. 54
Figure 5-11. Compression gain over 200 realizations for (a) regular TR for both 1-port and 2-port cavities, and for (b) OBTR for both 1-port and 2-port cavities. For all simulations the impulse response length was 1600 ns. 55
Figure 5-12. Un-truncated, time-reversed impulse responses from (a) the 2-port cavity and (b) the 1-port cavity. The early-time reflections can clearly be seen in the 1-port impulse response while they are absent in the 2-port impulse response. 56

Figure 5-13. (a) Compression gain for 1-port and 2-port cavities after truncating the impulse response to remove the initial prompt reflections in the 1-port response. (b) The difference in gain showing that in fact, 1-port pulse compression is superior even for regular time reversal as long as the waveform has the prompt reflection removed. For all simulations the impulse response length was 1600 ns.....57
Figure 5-14. (a) CST model of 2-port cavity with perturber and (b) 1-port cavity. This 1-port cavity is identical to the 2-port except that port has been replaced by a blank plate (highlighted in red circle). 58
Figure 5-15. (a) Simulation schematics of 2-port, and (b) 1-port cavity as simulated using S-parameters determined in CST full-wave simulation. In both (a) and (b) the 50 Ohm load is the equivalent waveform recording point. 59
Figure 5-16. Measured WRD650 circulator 3-port S-parameters from 6.5 GHz to 17.5 GHz (a) reflection coefficients (b) transmission coefficients, and (c) isolation. Average insertion loss: S21 = 0.93 dB, S32 = 0.85 dB. Average isolation: S12 = 17.1 dB, S31 = 17.5 dB. 62
Figure 5-17. Circuit diagram for Keysight ADS simulation using 3-port s-parameters for the circulator rather the ADS-defined circulator. 63
Figure 5-18. (a) Experimental setup for both 1-port and 2-port measurements. The Attenuation Shunt switches between a low insertion loss (IL) and high IL attenuator to protect the oscilloscope from the high peak power of the reconstructed impulse. (b) System under test (SUT) for 2-port TRPC measurements. (c) SUT for 1-port TRPC measurements. 64
Figure 5-19. Experimental set-up for 'full time-domain' method. Port 2 of the circulator is connected directly to the cavity. Input port and Output port of the TRPC system are labeled Port 1 and Port 2, respectively. 65
Figure 5-20. Compression gain for the 1-port and 2-port cavities for regular *TR*. Plots include modeling results from section 5.2, simulated results from section 5.3, and measured results from section 5.4. Also included are modeling results with insertion loss and losses incurred from non-ideal isolation, and results from simulations using the CST cavity results and S-params from the real circulator. 68
Figure 5-21. Compression gain for the 1-port and 2-port cavities for *OBTR*. Plots include modeling results from section 5.2, simulated results from section 5.3, and measured results from section 5.4. Also included are modeling results with insertion loss and losses incurred

from non-ideal isolation, and results from simulations using the CST cavity results and S-params from the real circulator. 68
Figure 5-22. Simulation and measurement results from 5.3 and 5.4 for (a) compression gain for regular TR for the 1- and 2-port cavities, and (b) compression gain results for the 1-port and 2-port cavities for OBTR. 70
Figure 6-1. Trade space of bandwidth and peak power for different USP sources from Figure 1-1 with high-power TR (HP TR) added to show how this work moves the state-of-the-art in this direction. 73
Figure A-1. Flowchart Describing GA decision process. 78
Figure A-2 - Two linear actuators shown in holders and connected to posts. 79
Figure A-3. Eight-channel relay module (left) controls 4 relays (+12 V, up; -12 V down). Arduino Mega microcontroller (right) controls each relay. 79
Figure B-1. (a) Measurement setup for the interrogation phase where the impulse response is measured, and which corresponds to the switch allowing signal to pass for less than 100 ns. (b) Measurement setup for the reconstruction phase where the reconstructed impulse is measured, and which corresponds to the switch only allows signal to pass during the last 100 ns or less while blocking signal for the first ~900 ns. 81
Figure B-2. Results from measurements using switching scheme from Figure B-1 for (a) Low-power OBTR input signal and reconstructed signal showing no early time-sidelobes and 14.5 dB compression gain. (b) High-power OBTR input showing no early time-sidelobes, but also reduced gain due to limiting of the reconstructed impulse. Switch used is Narda S213D. 82
Figure B-3. Results from measurements using setup from Figure B-1, but with no switching. (a) Low-power OBTR input signal and reconstructed signal showing early time-sidelobes and 14.1 dB compression gain. (b) High-power OBTR input showing early time-sidelobes, but also a limited reconstructed impulse and reduced gain. Switch used is Narda S213D. 82
Figure B-4. (a) Comparison of impulse responses from low-power and high-power measurements and the original impulse when the switch does not block any signal. (b) Comparison of impulse responses from low-power and high-power measurements and the original impulse when the switch performs the switching scheme from Figure B-1. 83

Figure B-5. (a) Low-power OBTR input signal and reconstructed signal showing no early time-sidelobes and 14.3 dB compression gain. Switching is executed according to Figure B-1 for (b) Low-power OBTR input signal and reconstructed signal showing early time-sidelobes and 14.7 dB compression gain. Here, switch always allows signal to pass. Switch use is RF Lambda RFSP2TRDC18G. 83
Figure B-6. (a) Impulse response using RF Lambda RFQ135225 fast microwave switch. (b) Impulse response using Narda S213D fast microwave PIN-diode switch. In both, it is difficult to see the increase in the loaded quality factor when the switching technique is used. 84
Figure B-7. (a) Impulse responses from Figure B-6(b) plus an impulse response with no switch as all with a moving average applied to show an increase in energy (leading to a higher quality factor) in the switching case. (b) Calculated loaded quality factors and time constants from the plots in (a). 84

List of Tables

Table 1-1. Several Standardized Definitions of Ultra-wideband (UWB). 4
Table 1-2. Fractional Bandwidth and Band Ratio Definitions. 4
Table 1-3. Definition of Bandwidths for Electromagnetic Interference (EMI). 4
Table 3-1. Comparison of Other EM TR Pulse Compressors in the Literature with This Work. .28
Table 5-1. Statistics Of Compression Gain Modeling For Regular TR And OBTR 55
Table 5-2. Compression Gain Comparison: 2-Port Vs. 1-Port Cavity: Regular Time-Reversal ... 61
Table 5-3. Compression Gain Comparison: 2-Port Vs. 1-Port Cavity: One-Bit Time-Reversal ... 61
Table 5-4. Compression Gain Vs. Circulator Isolation 62
Table 5-5. Compression Gain Using Measured 3-Port S-Params From Real Circulator 63
Table 5-6. Compression Gain Comparison: 2-Port Vs. 1-Port Cavity: Regular Time-Reversal ... 65
Table 5-7. Compression Gain Comparison: 2-Port Vs. 1-Port Cavity: One-Bit Time-Reversal ... 66

List of Abbreviations

AWG	Arbitrary Waveform Generator
BW	Bandwidth
BWO	Backward Wave Oscillator
CST	Computer Simulation Technology
DSRD	Drift Step Recovery Diode
EMC	Electromagnetic Compatibility
EMI	Electromagnetic Interference
ERP	Effective Radiated Power
FID	Fast Ionization Dynistor
FOM	Figure of Merit
FWHM	Full-Width Half-Maximum
GA	Genetic Algorithm
HP TR	High-Power Time-Reversal
IRA	Impulse Radiating Antenna
LP TR	Low-Power Time Reversal
OBTR	One-bit Time Reversal
MEMS	Micro-electromechanical Systems
MMIC	Monolithic Microwave Integrated Circuit
PC	Pulse Compression
PCSS	Photoconductive Solid State Switch
PEC	Perfect Electric Conductor
PRF	Pulse Repetition Frequency
PRI	Pulse Repetition Interval
PSO	Particle Swarm Optimization
PW	Pulse Width
SRD	Step Recovery Diode
TR	Time Reversal
TRPC	Time-Reversal Pulse Compression

TRM	Time Reversal Mirror
USP	Ultrashort Pulse
UWB	Ultra-wideband
VNA	Vector Network Analyzer

Chapter 1 - Introduction

1.1 - Motivation and State-of the Art

Generation of high-peak power, microwave ultra-short pulses (USPs) is desirable for ultra-wideband communications [1], [2], and radar/remote sensing [3-8]. A variety of microwave USP generators exist today, or are described in the literature, and have benefits and limitations depending on application. These generators are based on technology ranging from anode/cathode-type methods like superluminal generators [9], [10], and superradiant backward wave oscillators (BWOs) [11], [12] to solid state generators employing switches such as step-recovery diodes (SRDs) [13], drift step recovery diodes (DSRDs) [14-16], fast ionization dynistors (FIDs) [17], silicon avalanche transistors [18], and photo-conductive solid-state switches (PCSSs) [19], [20]. There are also pulse compression techniques such as such as the fivefold, helically corrugated waveguide compressor shown in [21]. Other types of microwave pulse compressors exist, but these do not produce sub-nanosecond or near-sub-nanosecond pulses. Finally, a new class of ultra-wideband pulse compressors for generating microwave USPs has been developed in the last decade that use electromagnetic (EM) time-reversal (TR) techniques, and are the topic of this work. These will be described further in section 1.3 and 2.2, but before the techniques described in this dissertation, time-reversal-based USP generators have only been demonstrated in the high-bandwidth/low peak-power regime.

Figure 1-1 summarizes these technologies in terms of peak-power capability and bandwidth such that four categories are delineated: 1) low bandwidth/low peak power, 2) low bandwidth/high peak power, 3) high bandwidth/low peak-power, and 4) high-bandwidth, high-peak power. The dividing lines between the categories are arbitrary, but it can be readily seen from the literature that there is a lack of short pulse and ultra-short pulse generators that increasingly have both high bandwidth and high peak-power. This dissertation focuses on techniques for improving the existing technology of time-reversal pulse compression cavities for operating in the high-bandwidth/high-peak power regime. Before further describing TR techniques and TR-based pulse compressors, section 1.2 discussed how the term ultra-short pulse is defined in this dissertation.

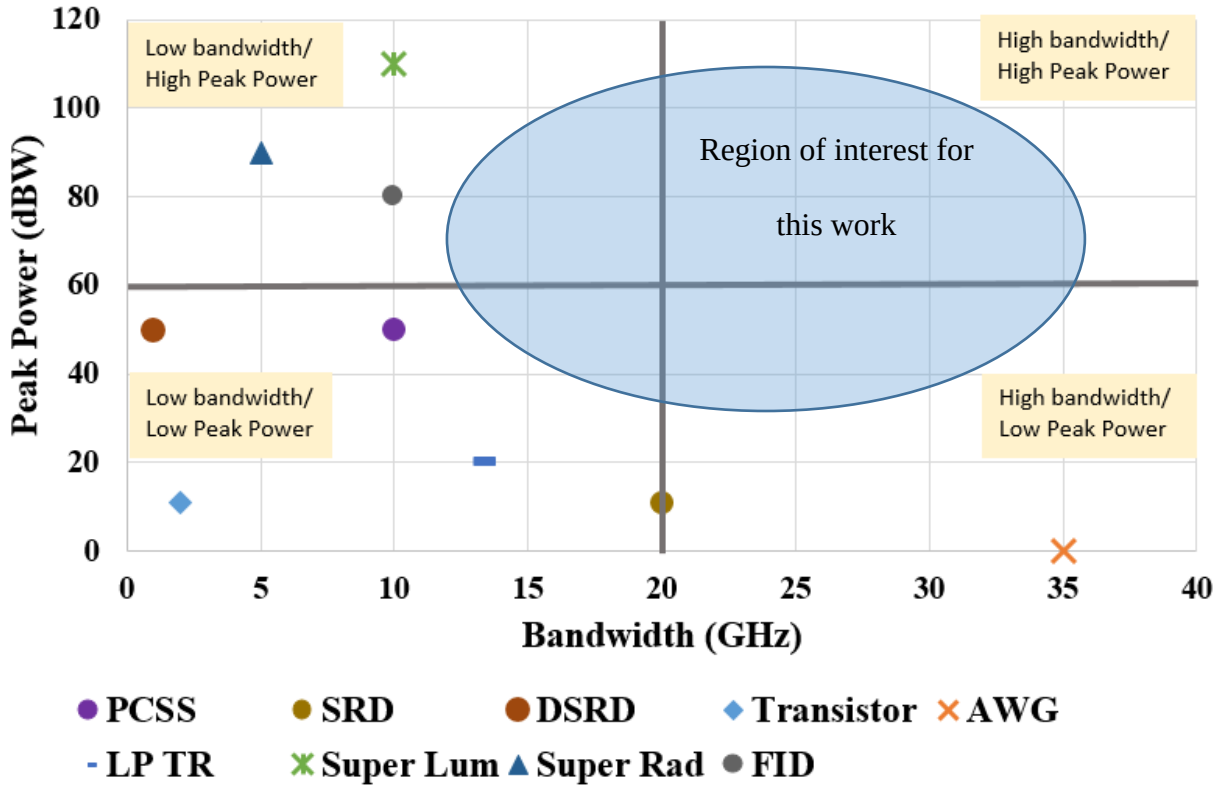

Figure 1-1. Trade space of bandwidth and peak power for different USP sources. Time-reversal-based ultra-wideband pulse compression cavities have potential to enable pules generation in the high-bandwidth/high-peak power regime. Legend for USP generator enabling technology: PCSS = Photoconductive Solid State Switch; SRD = Step Recovery Diode; DSRD = Drift Step Recovery Diode; Transistor = Avalanche Transistor; AWG = Arbitrary Waveform Generator; LP TR = Low Power Time-Reversal; Super Lum = Super Luminal; Super Rad = Superradiant; FID = Fast Ionization Dynistor.

1.2 - What is an Ultrashort Pulse?

The term USP typically refers to optical pulses that are 10s of picoseconds or less in pulse width, though the definition is not standardized [22]. Pulse width is defined here to be the width of the pulse in nanoseconds between the two points of half the peak value, also known as full-width half-maximum (FWHM). Other definitions for pulse width exist, but the definition used here is standard for the type symmetric pulse primarily used in this dissertation. The term USP when applied to pulses in the microwave region is even less standardized. In general, though, the term ‘ultra-short pulse’ is related to the concept of an ultra-wideband (UWB) signal such that an ultra-

short pulse has ultra-wide bandwidth. Definitions of UWB vary, but usually rely on the fractional (percent) or absolute bandwidth (b_f or BW):

$$BW = (f_h - f_l) \quad \text{and} \quad b_f = \frac{BW}{f_c} = \frac{2(f_h - f_l)}{f_h + f_l} \tag{1.1}$$

where f_h is the highest frequency of the signals spectrum, f_l is the lowest frequency, and f_c is the center frequency. The 'band ratio', the ratio of f_h to f_l, is also sometimes used, though this term is less popular in the literature. Using these definitions, several organizations have stipulated the following as UWB, Table 1-1.

In terms of modern high power UWB sources, the bandwidths specified are less useful as UWB waveforms routinely have bandwidths measured in many GHz. Recognizing this, Mokole *et al.* in [23], devised a new description of UWB waveforms shown in Table 1-2. These terms are generally more used in the radar community, whereas it should be noted that the definitions in Table 1-1 were largely developed with the communications industry in mind. Also, for completeness, it is noted that yet other definitions have been devised for use in the electromagnetic compatibility (EMC) community, Table 1-3; these definitions use the same fractional bandwidth and band ratio definitions as in Table 1-2, but use different nomenclature such that 'ultra-wideband' is bisected into 'subhyperband' and 'hyperband.' For the two systems described in this dissertation the bandwidths are 13 GHz with a center frequency of 11 GHz, and 10.5 GHz with a center frequency of 11.75 GHz, respectively. This gives fractional bandwidths of 1.18 and 0.89, respectively, which falls within the definition of UWB according to Table 1-2. Figure 1-2 and Figure 1-3 show examples of narrowband, wideband, and ultra-wideband waveforms including the one studied in this dissertation, which is described by the $sinc(t)$ function, also referred to as the cardinal sinus function.

Table 1-1. Several Standardized Definitions of Ultra-wideband (UWB).

	DARPA	***IEEE STD 1672***	***American FCC***	***European Union***
Limits	NA	-10 dB	-10 dB	NA
b_f	≥ 0.25	≥ 0.25	≥ 0.20	NA
BW	NA	$> 500\ MHz$	$> 500\ MHz$	$> 50\ MHz$

Table 1-2. Fractional Bandwidth and Band Ratio Definitions.

Category	***Factional Bandwidth***	***Band Ratio***
Narrowband (NB)	$0.00 < b_f \leq 0.01$	$1.00 < b_r \leq 1.01$
Wideband (WB)	$0.01 < b_f \leq 0.25$	$1.01 < b_r \leq 1.29$
Ultra-wideband (UWB)	$0.25 < b_f \leq 2.00$	$1.29 \leq b_r \leq \infty$

Table 1-3. Definition of Bandwidths for Electromagnetic Interference (EMI).

Category	***Factional Bandwidth***	***Band Ratio***
Hypoband (NB)	$0.00 < b_f \leq 0.01$	$1.00 < b_r \leq 1.01$
Mesoband (MB)	$0.01 < b_f \leq 0.25$	$1.01 < b_r \leq 1.29$
Sub-Hyperband (SHB)	$0.25 < b_f \leq 1.50$	$1.29 < b_r \leq 7.00$
Hyperband (HB)	$1.50 \leq 2.00$	$7.00 < b_r \leq \infty$

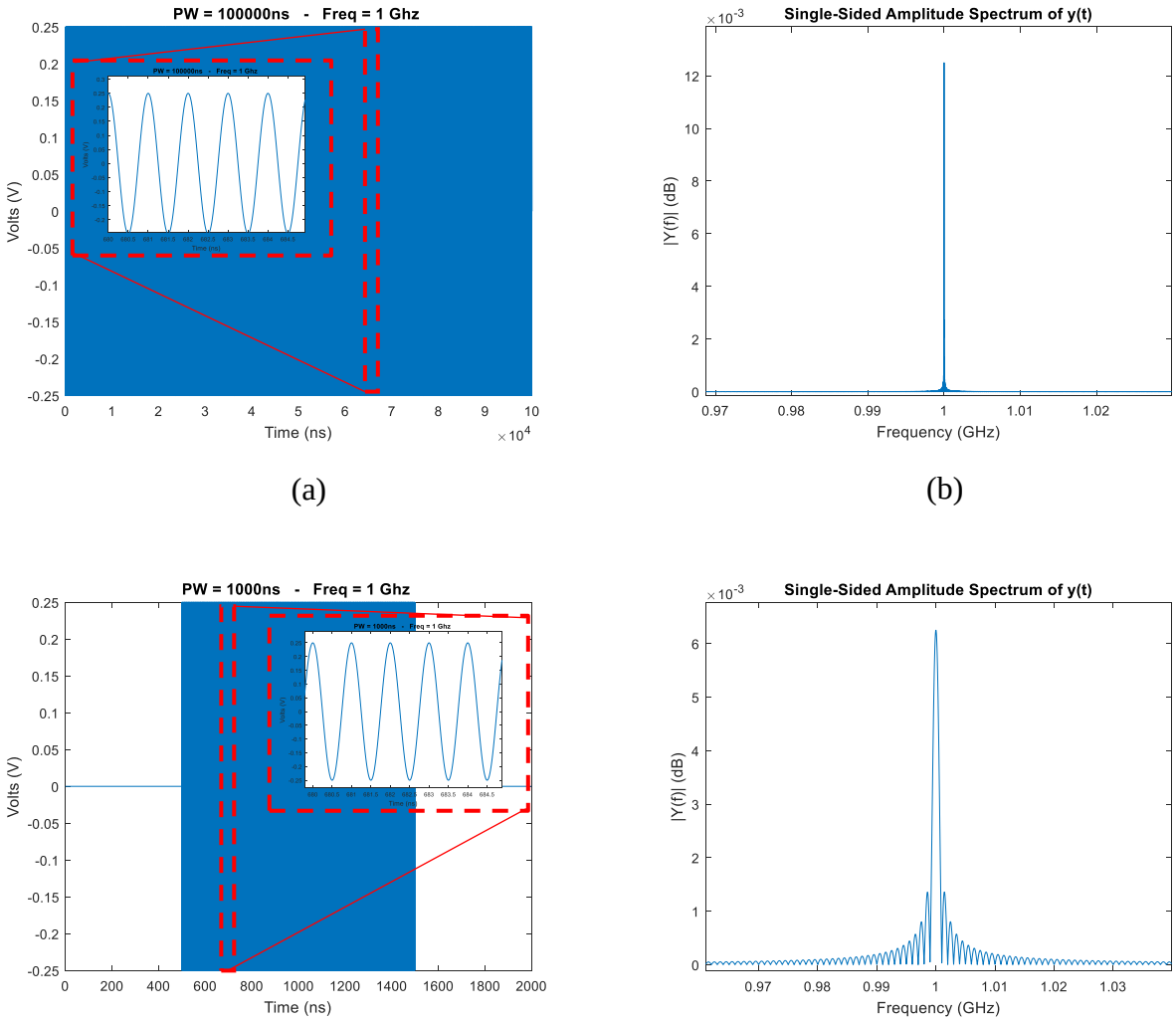

Figure 1-2. Examples of narrowband waveforms. (a) An approximated continuous wave (CW) waveform and (b) its spectrum (an approximated single frequency). (c) A narrowband waveform and (d) its spectrum.

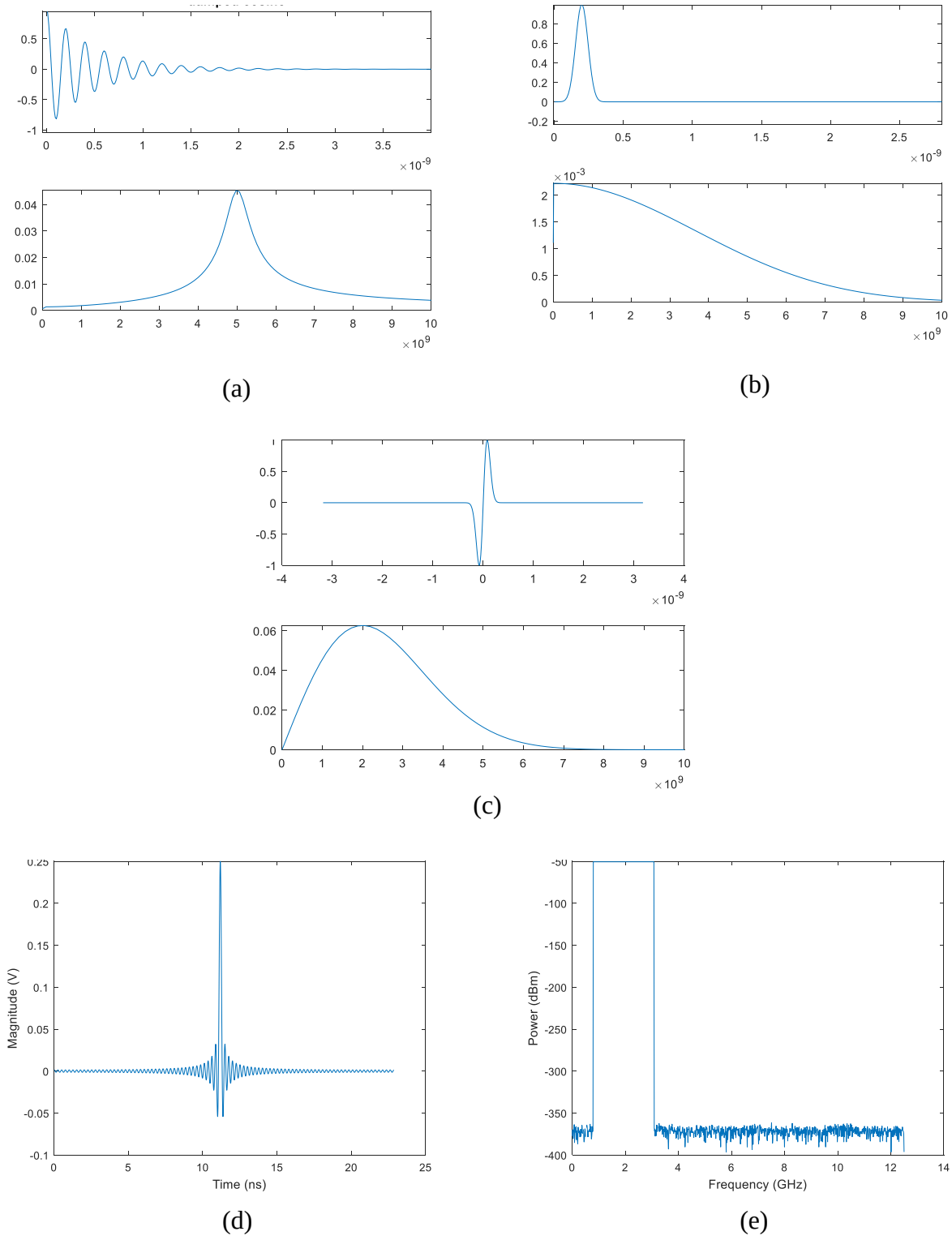

Figure 1-3. Examples of wideband and ultra-wideband waveforms. (a) A damped sinusoid and its spectrum. (b) A Gaussian impulse and its spectrum. (c) A Gaussian monocycle and its spectrum. (d) A sinc (cardinal sinus) pulse and (e) its spectrum.

1.3 - Ultra-wideband Microwave Pulse Compression using Time-Reversal Techniques

As discussed, a new class of ultra-wideband pulse compressors for generating USPs has been developed in the last decade that uses electromagnetic (EM) time-reversal (TR) techniques, and is the topic of this work. TR is the process of substituting a negative time variable for a positive time variable in a general wave equation such that t becomes $-t$. This is a basic signal processing technique that has the effect of the reversing the waveforms profile in time, thus mirroring the waveform with respect to the y-axis. This basic TR variable substitution is mathematically trivial, but has surprising effects when applied to wave transmission in dispersive systems. TR as a technique for overcoming phase distortion in dispersive systems was first presented in [24]. Subsequently, other works showed that spatio-temporal focusing of energy using TR techniques could be achieved in both acoustics [25-27] and electromagnetics [28]. A more detailed discussion of TR theory will be provided in Chapter 2 of this dissertation.

EM pulse compression of low-power, ultra-wideband signals in a compact cavity (0.58 m × 0.32 m × 0.04 m) using TR techniques was first demonstrated experimentally in [29] to create a 130 ps pulse with a center frequency of 5.5 GHz and 7 GHz bandwidth (BW). The same technique was used in a high-power experiment in a larger cavity to create a ~3.3 ns pulse with a center frequency of 1.2 GHz and 300 MHz BW [30]. An ultra-compact (0.254 m × 0.127 m (W × D)), low-power TR pulse-compressor has since been demonstrated in a quasi-2D cavity using copper-plated dielectric boards as the cavity walls to again create a ~130 ps pulse with a center frequency of 6 GHz and 8 GHz BW [31].

1.4 - Dissertation Organization and Objectives

This dissertation builds upon the work in [29] and [30] and presents a compact, high-gain, high-power, TR microwave pulse compressor that has ultra-wide bandwidth (5 GHz – 18 GHz), and waveguide feeds for high-peak power output capability over the entire band. The system uses a time-reversal-based pulse compression scheme with one-bit processing to achieve high peak power. Also presented is a novel technique implementing TR-pulse compression using a single-

port cavity and a microwave circulator. This system is also ultra-wideband (6.5 GHz – 17 GHz). Additionally, new analysis of variation in compression gain due to impulse response recording length and bandwidth variation, new experimental work on the effect of mode stirrer position on compression gain, a first-time comparison of efficiency between simulated and measured results, and a novel technique for reducing time-sidelobes while using OBTR are presented.

This dissertation is organized into seven chapters. Chapter 2 provides an overview of early and acoustic TR work. As well, it provides a review of the relevant electromagnetic TR literature, and a more in depth discussion of previously published TR pulse compressors and their figures of merit (FOM). Chapter 3 presents the design, fabrication, measurement, and analysis of the 2-port, high-gain, high-power pulse compression cavity. Chapter 4 presents a novel technique for reducing time-sidelobes when using one-bit time-reversal. Chapter 5 presents the design, fabrication, measurement, and analysis of the 1-port cavity system. Chapter 6 is a summary of the dissertation and provides avenues for future research.

Chapter 2 – Time Reversal Theory

Mathematically, time-reversal (TR) is the process of substituting a negative time variable for a positive time variable in a general wave equation such that t becomes $-t$. Thus, the impulse response of any system, denoted as $h(t)$, becomes $h(-t)$. Using the Fourier transform to move to the frequency domain, $h(t)$ becomes $\mathcal{F}\{h(t)\} = H(\omega)$, and $h(-t)$ becomes $\mathcal{F}\{h(-t)\} = H^*(\omega)$, the complex conjugate of $H(\omega)$. So, time reversal is also phase conjugation. In this sense 'time-reversal' is really just 'waveform reversal' as in Figure 2-1, that is, TR is simply the reversing of a waveform's profile in time.[1]

2.1 - Early Experiments in Communications and Acoustics

TR as a technique for overcoming delay distortion in dispersive systems has been known since B.P. Bogert's 1957 paper [24]. In this paper, Bogert was interested compensating for delay distortion effects on data, slow speed television, and signature transmission over long distance telephone communication networks. Inspired by similar work undertaken in speech distortion in 1954 [32], he conducted experiments in one of which pictures were transmitted over a 16,600 mile loop from New Jersey to Los Angeles. The original transmission was recorded on a magnetic tape

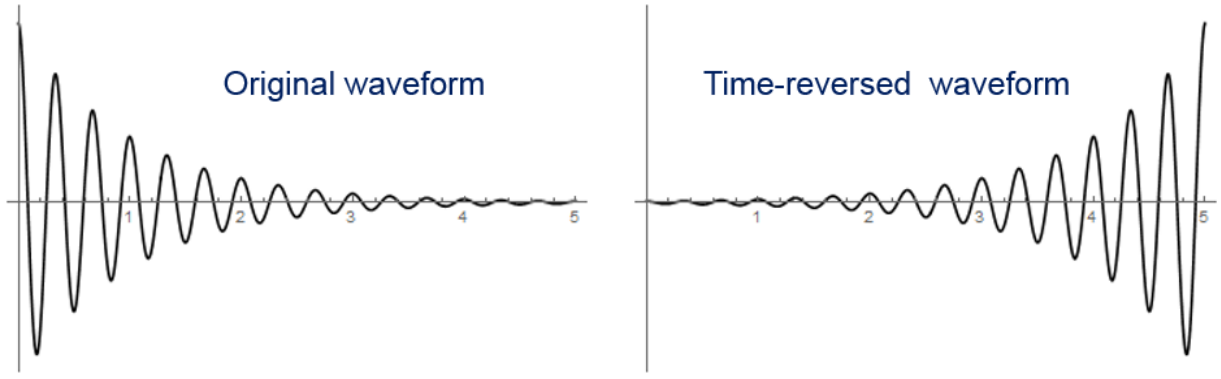

Figure 2-1. TR is simply the reversing of a waveform in time, ($t \longrightarrow -t$).

[1] In fact, in Figure 2.1, there is also a time-shift on the time-reversed waveform such the time reversed waveform is $h(\tau - t)$, but there is no loss in generality in describing this process as simply $h(-t)$.

and then the tape was physically put in backwards for the retransmission such that the tape played in reverse over the magnetic reader head. He shows, in pictures, a dramatic improvement in picture quality between the non-TR transmission and the TR transmission. His block diagram, Figure 2-2, and notation are essentially identical to the way this process is described today. It was not until the 1980's and 1990's that Prada, Fink, Jackson, Dowling, Lerosey, and others showed that spatio-temporal focusing of energy using TR techniques could be achieved in acoustics [25-27]. These papers all describe the use of an array of transducers which transmit towards a target, time-reverse the recorded, backscattered target signal, and then re-transmit. This retransmission then 'reconstructs' both spatially and temporally at the original transmitter. Figure 2-3 shows a diagram of the seminal experiment in [25] with 'time reversal mirrors' and the also the first use of 'iterative time-reversal' to selectively focus on a target. As the iterative TR process is repeated, from the first to the seventh iteration, the lower amplitude resonance is deselected. The work in [27] is also likely the first work to describe the concept of the time-reversal cavity to replace the TR mirror.

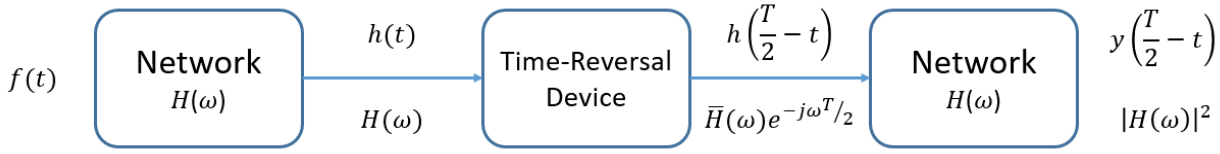

Figure 2-2. Block diagram of time-reversal system adapted from B. P. Bogert's 1957 paper [24]. An image or impulsive waveform, $f(t)$, is transmitted on a network with transfer function, $H(\omega)$, to produce the response, $h(t)$. This response is time-shifted and time-reversed, and retransmitted over the network resulting in a reconstructed image or impulse, $y(t)$, with, ideally, zero phase.

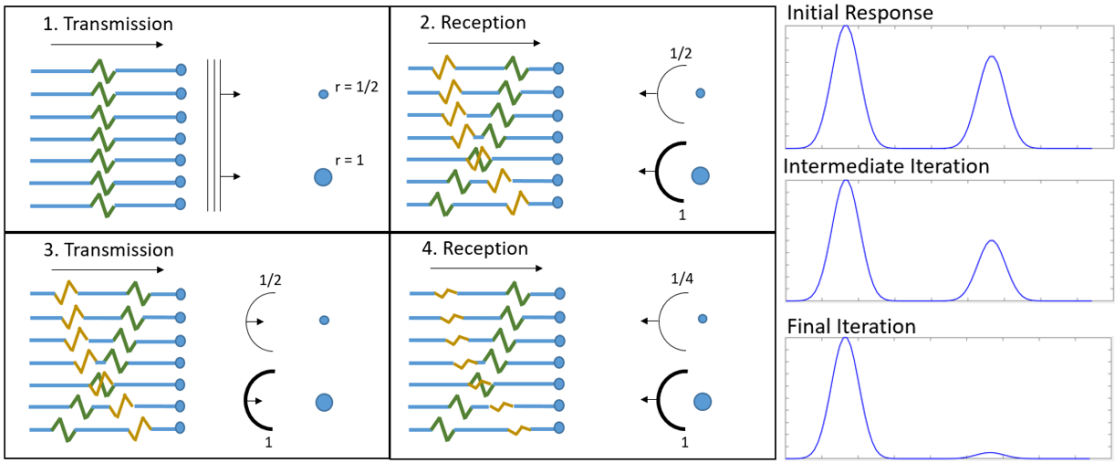

Figure 2-3. Iterative TR Process adapted from Fink, Prada, and Casserau [25]. I the first step of the iterative process, the transducers transmit identical signals to two targets of different size. The backscattered signals are recorded, time-reversed and re-transmitted. After several iterations the response of the smaller scatter is virtually non-existent.

2.2 - Electromagnetic Time-Reversal

The first modern paper describing electromagnetic time-reversal is G. Lerosey's "Time Reversal of Electromagnetic Waves" wherein they use a baseband signal mixed up to ~2.45 GHz to show pulse compression in a reverberant room [28]. Like earlier work in acoustics, it is also shown that the focusing is both spatial and temporal by placing receivers a few wavelengths away and showing no pulse reconstruction at those locations. This was a narrowband experiment. In 2006, with the advent of high-sampling rate arbitrary waveform generators, Lerosey *et al.* performed time reversal with wideband microwave signals [33]. Here, rather than use a cavity, they returned to the experimental setup of the time-reversal mirror (TRM) from [25]. Now, though, instead of acoustic transducers, microwave antennas are used for both transmitting and receiving arrays, Figure 2-4.

Another use of use of cavities for spatio-temporal focusing of electromagnetic waves was demonstrated in [34]. Here, the cavity has a large aperture, Figure 2-5. A transmitter at some distance outside the cavity transmits, and this signal is recorded by a receiving array of omni-directional antenna within the cavity. Upon TR and re-transmission, the radiation waves 'compress' or 'focus' in space at the spot of the original transmission. Hong *et al.* performed a similar experiment in [35], but instead of a receiving array with the cavity, a single monopole antenna was used.

Since these original papers and related studies, there have been hundreds of TR papers published on a variety of topics ranging from overcoming multipath effects in dispersive urban environments [36] to locating faults in power networks [37]. There is a vast literature on TR theory and application but this dissertation focuses solely on wideband and ultra-wideband electromagnetic pulse compression in cavities.

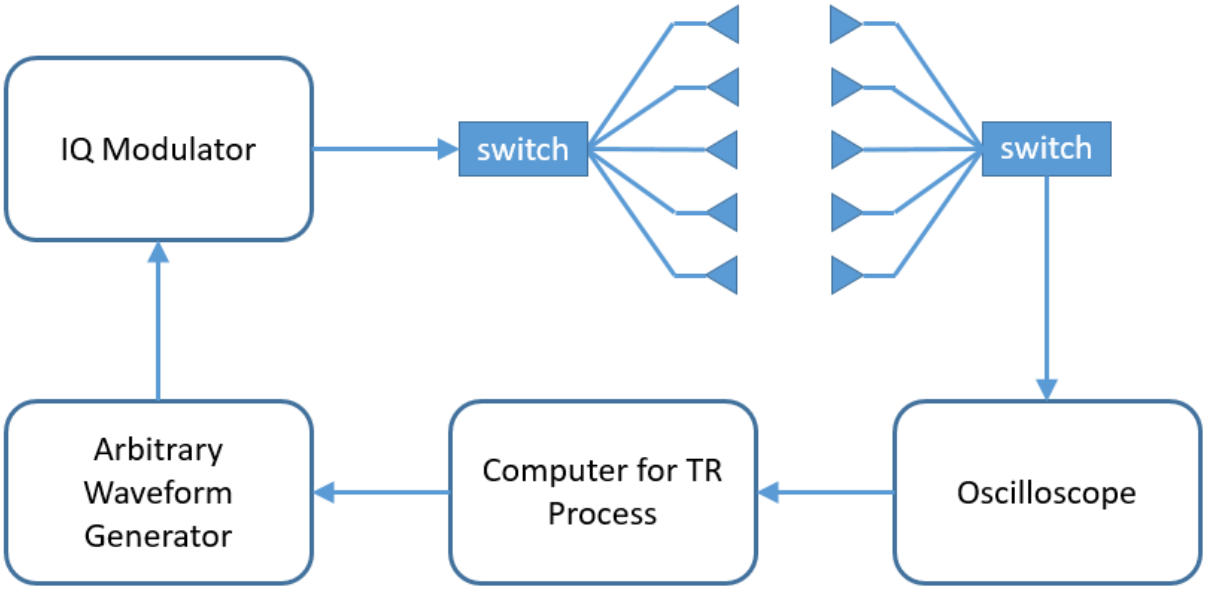

Figure 2-4. Wideband time-reversal experiment using multiple antennas in arrays for both the time-reversal mirror and receiver (adapted from [33]).

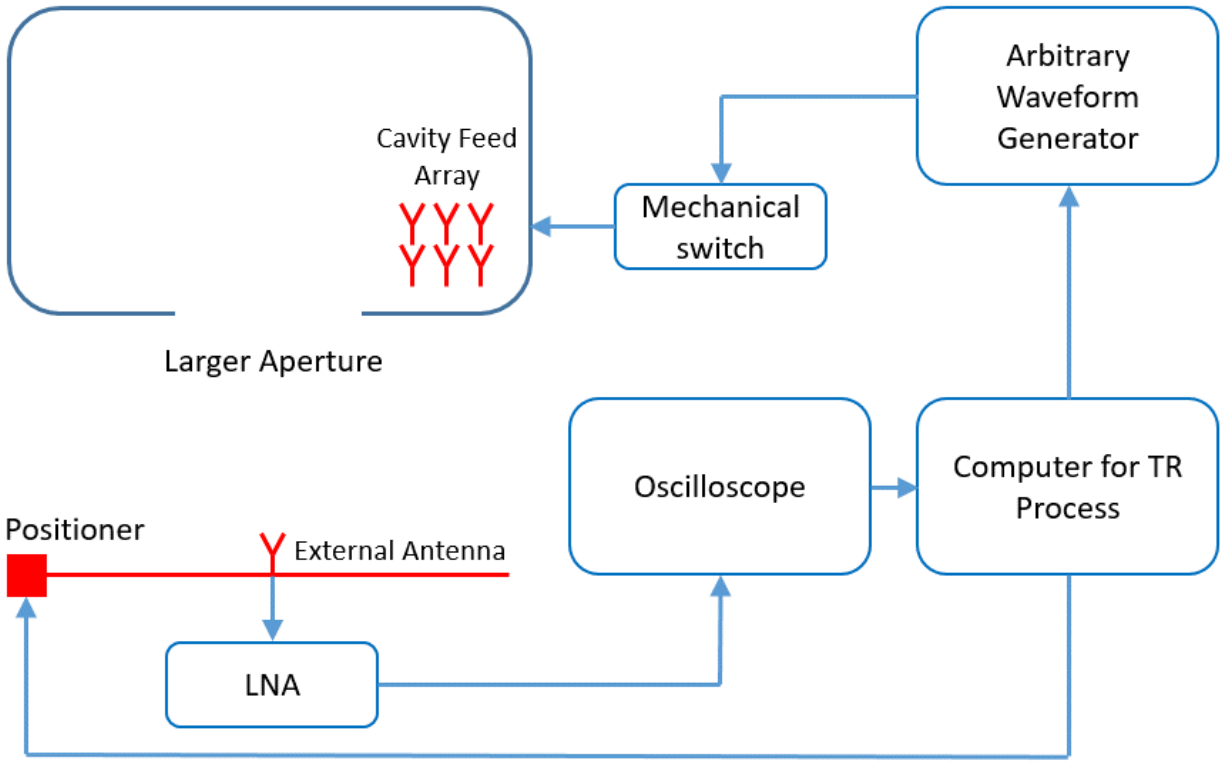

Figure 2-5. 'Leaky' reverberation chamber experimental setup for TR compression of electromagnetic waves in space (adapted from [34]).

2.3 - Time Reversal for Wideband Electromagnetic Pulse Compression in Cavities

In this section TR theory and its relation to pulse compression in dispersive cavities is discussed. The standard method of using a dispersive two-port cavity to take a long-duration, low-peak-power input, and compress it to a short-duration output with a higher peak power is shown in Figure 2-6. If an impulse (a USP), $f(t)$, is amplified by an ultra-wideband amplifier and transmitted into a dispersive cavity, and if the energy in the cavity is conceptualized in terms of rays, then it can be seen, in Figure 2-6(a), that some of the rays from the input will travel a short path to the output, some will travel a longer route, and some will explore most of the cavity before arriving at the output. It is the superposition in time of all these rays arriving at the cavity output that becomes the impulse response, $h(t)$, of the cavity.

By time-reversing this impulse response, $h(-t)$, and re-transmitting it through the UWB amplifier into the cavity, the reconstructed impulse, $y(t)$, can be obtained at the output. This process is shown in Figure 2-6(a). Due to reciprocity in this linear system, either the input or output may be used interchangeably to re-transmit. In the time-domain, the pulse compression process is described by (2.1) as the convolution of the impulse response, $h(t)$, with its own time-reversed profile,

$$y(t) = h(t) * ah(-t) = a\int_0^{\mathrm{T}} h(\tau)\, h(\tau - t)d\tau = \psi_{hh} \tag{2.1}$$

where '$*$' denotes convolution, a is a scaling/amplification factor (usually set to 1 in simulation, but is higher in measurement), and T is the impulse response record length in time. Thus, the pulse compression cavity acts as an autocorrellator for its own time-reversed impulse response. In the frequency domain, the transfer function can be described by its phasor such that $H(\omega) = |H(\omega)|e^{-j\Theta(\omega)}$, $H^*(\omega) = |H(\omega)|e^{j\Theta(\omega)}$, and the autocorrelation process is described as

$$Y(\omega) = H(\omega)H^*(\omega) = |H(\omega)|e^{-j\Theta(\omega)}|H(\omega)|e^{j\Theta(\omega)} = |H(\omega)|^2. \tag{2.2}$$

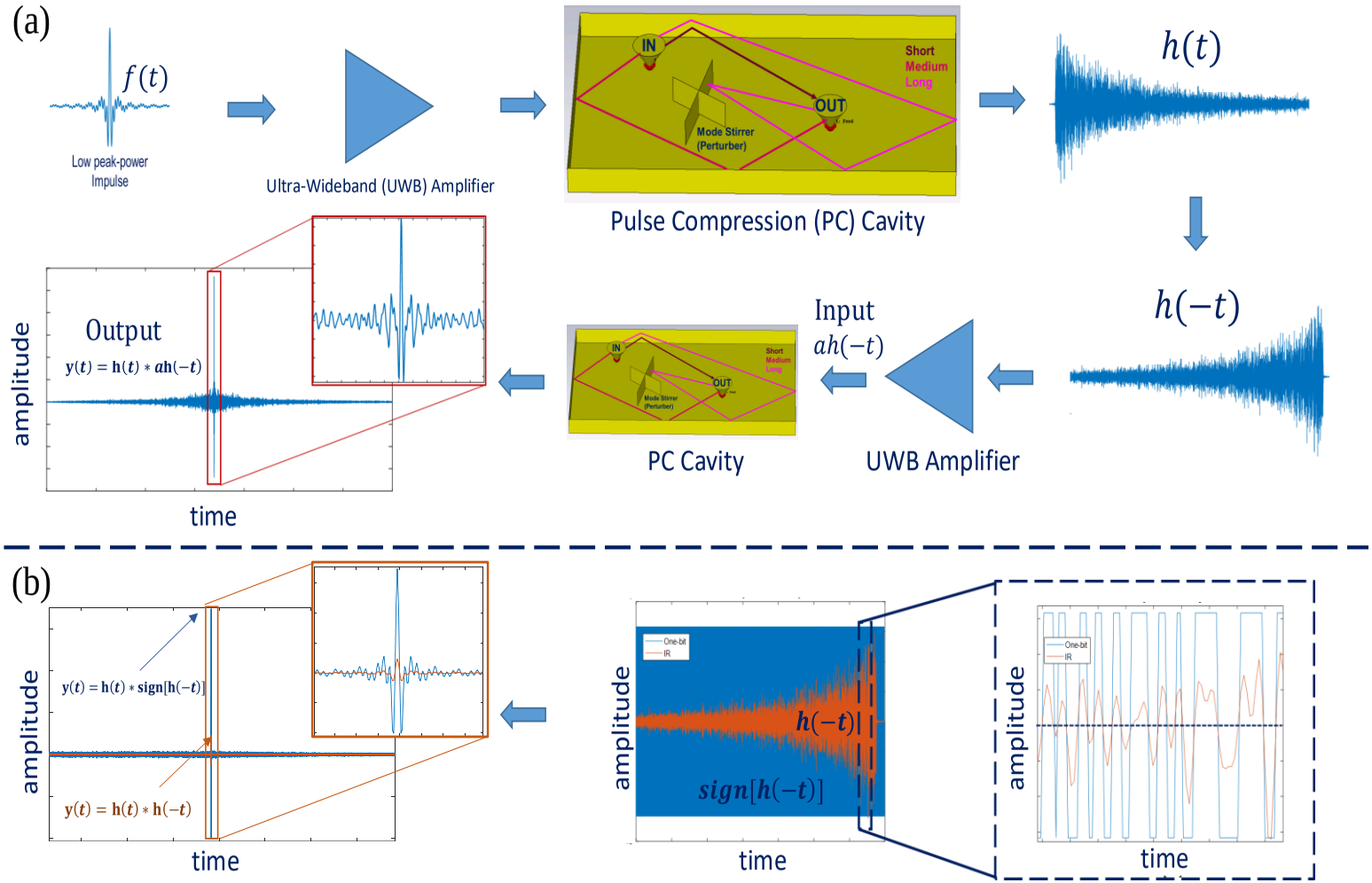

Figure 2-6. (a) Following the signal flow clockwise from the top left: The low peak power impulse, *f*(*t*), is transmitted through a UWB wideband amplifier into the dispersive cavity and the impulse response is recorded on an oscilloscope. Then, the IR is time-reversed, normalized, and retransmitted through the UWB amplifier into the PC cavity to obtain the reconstructed impulse. (b) shows the one-bit TR signal, sign[*h*(-*t*)], that may be used in place of *h*(-*t*) to obtain higher compression gain (in practice the large bandwidth that produces the 'square wave' would be filtered by the PC feed to the system bandwidth of 13 GHz.)

Here, at least ideally, the TR process results in a zero-phase function, which is why the TR process is often referred to as 'undoing' the phase errors caused by wave propagation in a complex (dispersive) environment.[2] This TR pulse compression process, however, only results in a few dB of compression gain [29]. Here, compression gain of the TR cavity, G_{TR}, is defined as the ratio of the peak magnitude of the cavity output signal (in Volts) to the peak magnitude of the cavity input (in Volts) in dB as given in (2.3). The same terminology and formulation for gain used in [33] is used here. In [34], this concept is referred to as *real gain*.

$$G_{TR} = 20\log_{10}\left[\frac{|y(t)|_{max}}{|ah(-t)/\max[h(-t)]|_{max}}\right] \tag{2.3}$$

The goal of this work is to create a compact, *high-power* pulse compressor. To do this, a technique called one-bit time-reversal (OBTR) is used. Originally applied in acoustics [38], and later applied in electromagnetics [29], OBTR applies the sign (signum) function to the TR impulse before re-transmitting in to the cavity, such that

$$\text{sign}[h(-t)] = \begin{cases} +1 \ for\ h(-t) > 0 \\ -1\ for\ h(-t) < 0 \end{cases} \tag{2.4}$$

This can be seen in Figure 2-6(b) where the decaying impulse response is overlaid on the one-bit signal; the inset shows that the OBTR signal has more energy per time that the original time-reversed impulse such that the amount of extra energy is the difference between the OB signal and the original impulse response. By applying OBTR and re-transmitting this 'energy-enhanced' signal through a wideband amplifier into the cavity, impulse reconstruction is still obtained at the output, but with increased gain now calculated as

$$G_{OBTR} = 20\log_{10}\left[\frac{|y(t)|_{max}}{|a\text{sign}\{h(-t)/\max[h(-t)]\}|_{max}}\right] \tag{2.5}$$

[2] It should be noted, that while TR does indeed 'undo' phase dispersion, its implementation in reverberant (overmoded) cavities does introduce some amplitude distortion due to the frequency response of the cavity, but this is expected as not all modes will be excited.

This technique was used in [29] and [30] to produce a compressed pulse in experiment having ~20 dB gain. The reconstruction with OBTR does result in time-sidelobes which could be detrimental for applications like UWB radar, and methods for reducing these will be discussed in Chapter 4.

2.4 - Summary

In this chapter, a review of basic time-reversal theory was presented in the context of pulse compression. Various experiments in the literature, e.g. in acoustics, have clearly shown the utility of using time reversal techniques for 'undoing' phase distortion incurred by the initial propagation of the waveform though the medium resulting in the 'reconstruction' of the original transmitted pulse. These early experiments were followed by a demonstration of TR techniques in electromagnetics wherein the acoustic transducers were replaced by antenna arrays. These demonstrations of TR, both in open media and in reverberant cavities, were demonstrated in low-power experiments, and the cavities were designed for low-power operation. This means that the input feeds and output feeds were standard coaxial connectors, which are not designed for high-power operation. Methods for calculating gain were introduced and a signal processing technique called one-bit time-reversal were also presented.

In Chapter 3, a novel TR pulse compressor design is presented that uses ultra-wideband waveguide feeds advancing the prior state of the art for high-power operation.

Chapter 3 - A Compact High-gain, High-power Ultra-wideband Pulse Compressor

In this chapter a compact, high-power, time-reversal-based microwave pulse compressor is presented. It is designed with waveguide feeds for high-power capability and has a curved inner geometry to promote an ergodic field distribution inside. First the design is presented, and then simulation results showing how compression gain varies with several different internal cavity materials. Next the cavity is fabricated and measurement results are presented including an analysis of cavity efficiency and an investigation into variations in compression gain due to varying the bandwidth of the excitation signal, and the length of the recorded impulse response. Finally, figures of merit of the pulse compressor in this work are compared with those from other researchers.

3.1 - Cavity Design and Simulation

The inner cavity dimensions are 65 cm x 45 cm x 4 cm. Inner volume is 11,151 cm^3. This is a little less than the rectangular volume due to wall curvature and added cylindrical scatterer. The height was chosen such that propagating modes can exist in the vertical direction making this a full 3D cavity, electromagnetically. The length and width were kept similar to those in [29], but it was verified that the cavity was electrically large using the relation specified in [39] that the characteristic length, L, (cubed root of the volume) of the cavity was at least three times the wavelength of the lowest frequency ($\lambda_1 = 6\ cm$). In the design L = 22.7 cm = 3.7λ_1. Simulations of the TR process were performed using the full-wave electromagnetic software suite, CST

The feeds are WRD500 waveguide sections that flare into horn-like apertures then gradually taper into the cavity walls. A cylindrical scatterer (height = 4 cm, radius = 6.98 cm) is placed in the cavity to block the direct path between the feeds (Figure 3-1(a)), which is further explained in Section 3.2. The reflection coefficient of the feeds over the entire bandwidth can be seen in Figure 3-1(b). By using waveguide rather than coaxial-dielectric feeds, the pulse compressor can operate at higher power levels, though a rigid, air-core coaxial line could also be

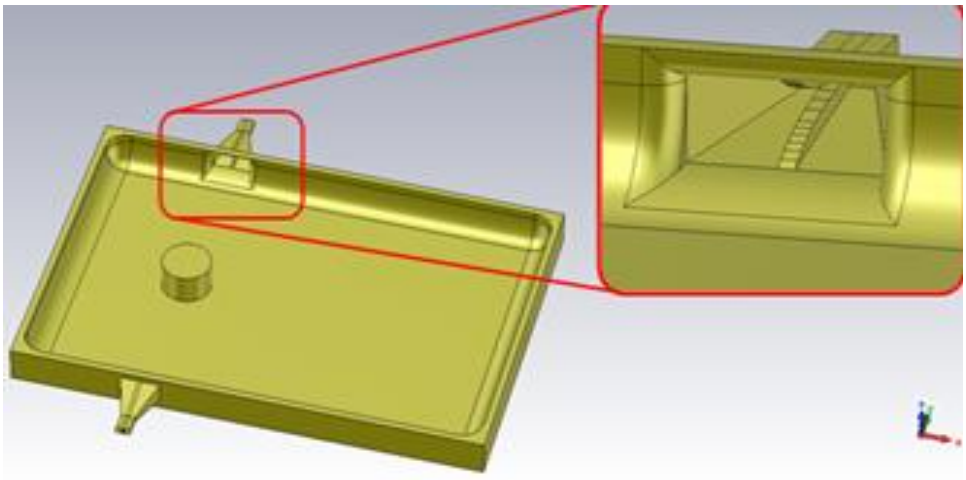

(a)

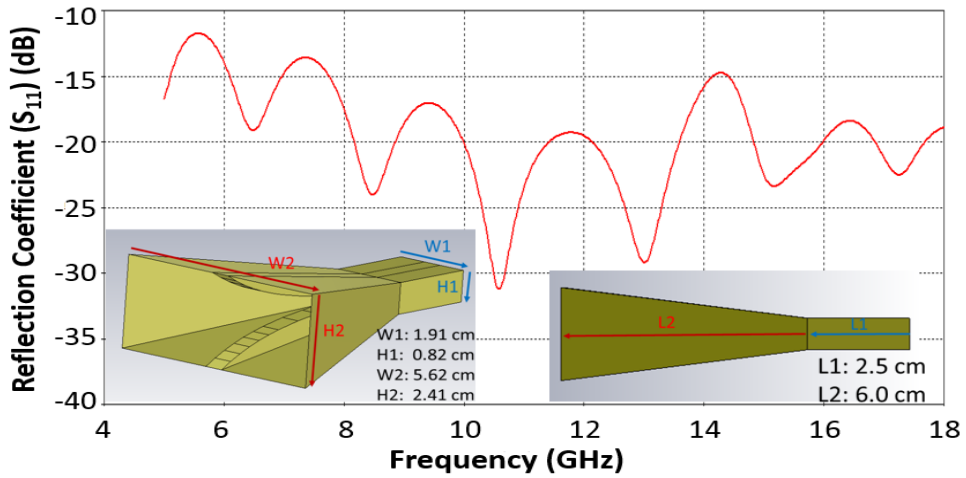

(b)

Figure 3-1. (a) Pulse compression cavity with waveguide feeds and cylindrical scatterer, and (b) reflection coefficient (S11) of the cavity feed from 5 - 18 GHz.

used. The feeds operate over the full bandwidth of 5 – 18 GHz and have a reflection coefficient (S_{11}) of less than -10 dB over the entire band.

For the pulse compression simulation, a sinc impulse, $\sin(x)/x$, with flat bandwidth from 5 – 18 GHz, is transmitted as the excitation pulse. The pulse width is ~35 ps at FWHM, Figure 3-2(a). Then, the OBTR process is performed as described previously, and the simulation is run for 100 ns longer than needed for impulse reconstruction to get a clear view of the peak, 3.3(b).

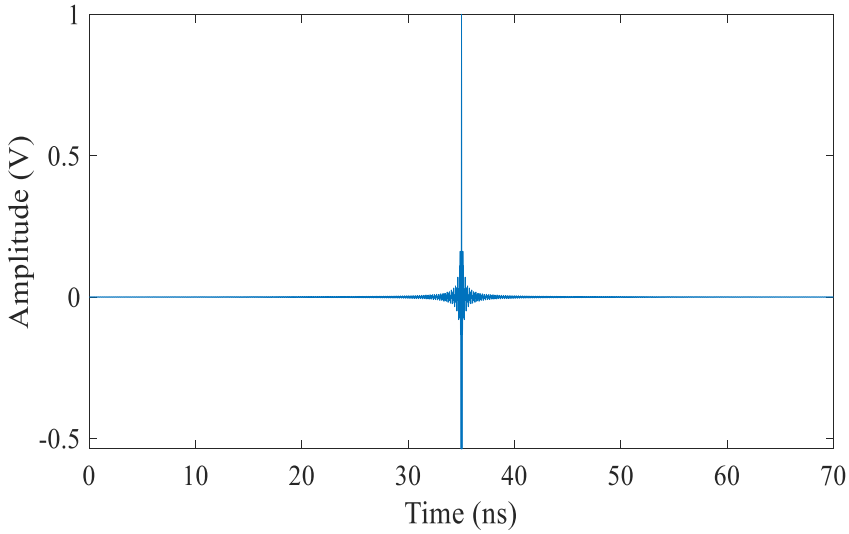

(a)

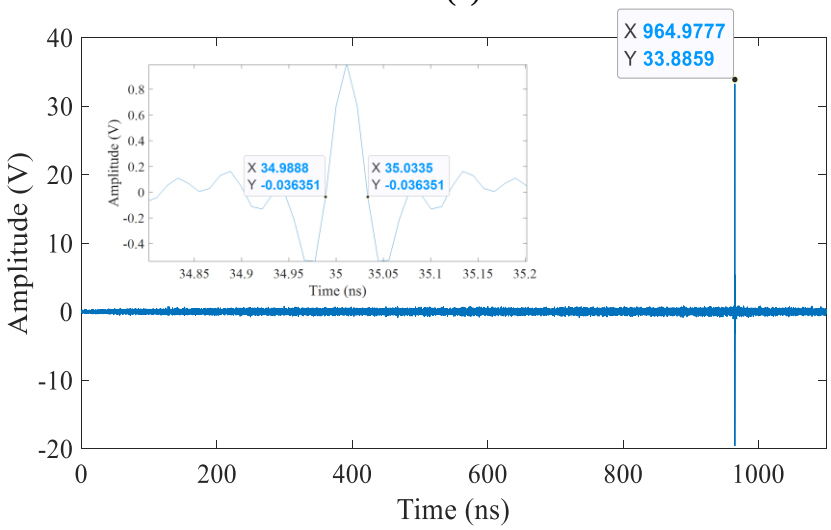

(b)

Figure 3-2. (a) Cavity excitation impulse is a sinc function with flat bandwidth from 5 – 18 GHz. Pulse width is ~35 ps at FWHM. (b) Simulated impulse reconstruction in PEC cavity showing reconstructed impulse at ~965 ns.

The cavity was simulated with several different materials, specifically perfect electric conductor (PEC), aluminum, copper, and silver, to assess the impact of cavity material on the compression gain, Figure 3-3. The ideal maximum gain for the pulse compression cavity is given by the time-bandwidth product ($t \times BW$), which is the product of the impulse bandwidth (13 GHz) and the impulse response length (up to 1.6 µs). Thus, ideally, and given a fixed bandwidth, a longer

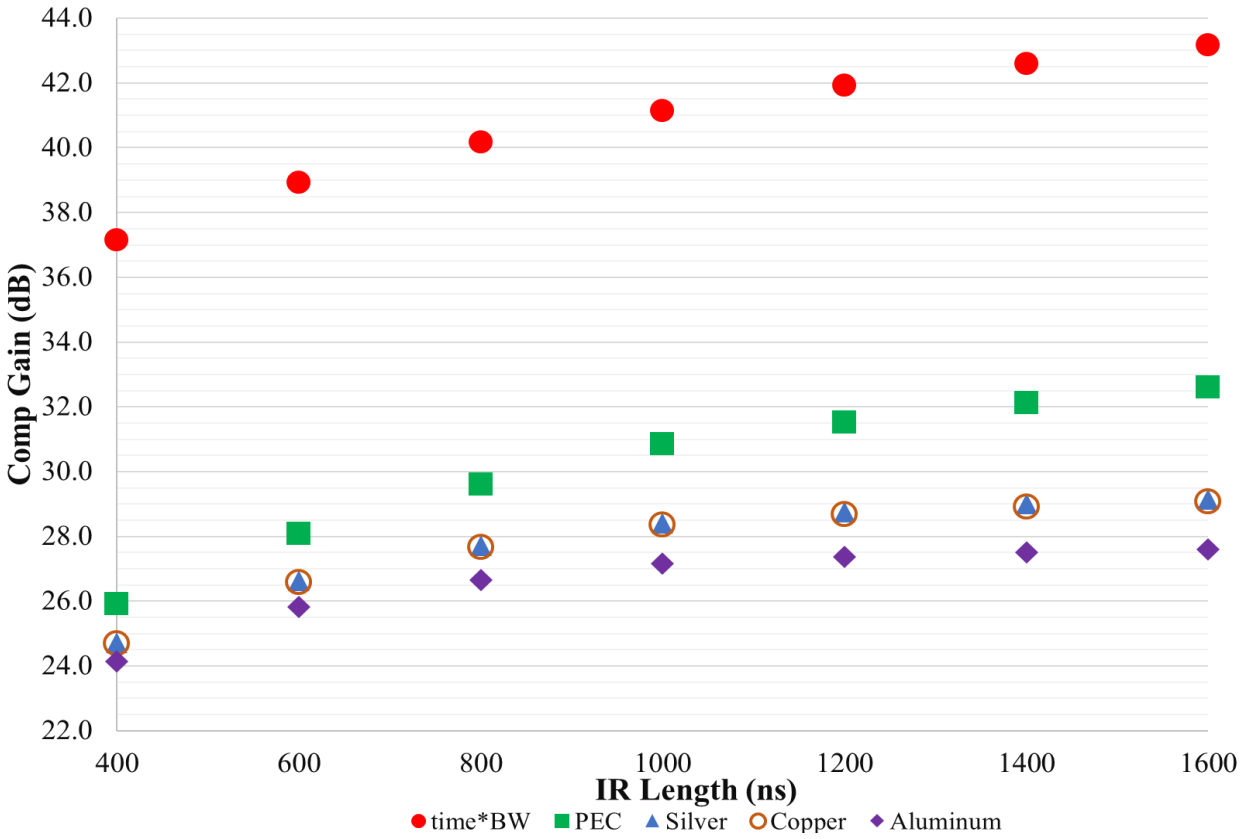

Figure 3-3. Tradeoff study of cavity material and impulse response length versus compression gain.

impulse response recording time results in higher gain. On the logarithmic (dB) scale, the time-bandwidth product continues to increase, though at decreasing rate. This is exactly a linear increase on a linear scale. The PEC cavity does not follow an ideal logarithmic increase in gain, however. And for the silver, copper, and aluminum cavities (with finite conductivity) the gain essentially becomes flat after roughly 1 µs. For the PEC cavity, this is due to energy lost through the ports. In a non-PEC (finite-conductivity cavity) Ohmic losses further contribute to a deviation from the time-bandwidth product gain values. In Figure 3-3 it can be seen that the PEC cavity gives the highest compression gain values (especially at longer impulse response recording times), while the aluminum cavity gives the lowest. The copper and silver cavities gave the highest compression gain for materials that can be used for fabrication through electroplating to the proper skin depth. However, the compression gain for the aluminum cavity was within about 1.0 dB of that for copper and silver at an impulse response length of 1 us, and is easier and lower cost to fabricate, thus, aluminum was chosen for cavity fabrication. The PEC simulation allows one to see the limits for

the pulse compression gain the conductivity of the walls of the cavity is increased. In practice PEC conditions could be more closely approached by placing the aluminum cavity in a dilution refrigerator to cool it to temperatures below the critical temperature.

3.2 - Cavity Fabrication and Experimental Set-up

The prototype cavity, shown in Figure 3-4, was fabricated out of solid aluminum to eliminate cavity wall deformation, as would be a concern with thin-plate sheets. The feeds are nearly identical to those in the simulation, which are WRD500 ridged waveguides with adapter sections that transition smoothly into the cavity. The inner dimensions of the cavity are identical to the simulation, and its outer dimensions are 67 cm x 47 cm x 6 cm with the lid being 1 cm thick. The inside of the cavity has curved walls (except where connected to the lid) to promote more ergodic scattering of the fields inside. A cylindrical scatterer centered between the feeds improves impulse response recording time (the time it takes the impulse response to decay to the oscilloscope noise floor). This is because, without the scatterer, a high amplitude early-time response causes difficulty in resolving the lower amplitude decay due to limited dynamic range on the scope. This could also be remedied by not having the feeds directly facing each other. Machining tolerance was 10 mils. Modeling of surface roughness with regard to comparison with simulation has not yet been attempted, but is not expected to be a significant issue of the frequency range of interest.

The full experimental setup is shown in Figure 3-5. First, the signal is created externally (in MATLAB), and then sent to the arbitrary waveform generator (AWG). The AWG is a Keysight M8196A with a maximum 92 GS/s sampling rate. Next, the USP is sent from the AWG into a wideband amplifier. The amplifier is a Qorvo 2 – 18 GHz solid-state amplifier with a nominal 75 W output (100 W in saturation). The amplified signal is then transmitted into the pulse compressor cavity. The pulse compressor output is set up with an 'attenuation shunt' such that, when the initial pulse is sent, it has a low attenuation level in order to observe the small signal on the oscilloscope. Then, when the OBTR process is complete, a higher attenuation level is selected to accommodate reading the high-peak output. The shunt is activated using RF switches controlled by Keithly power supplies. The attenuation shunt is controlled using MATLAB instrument control. The output of the cavity is recorded on a Tektronix DPO73304SX 33 GHz oscilloscope with 100 GS/s sampling rate.

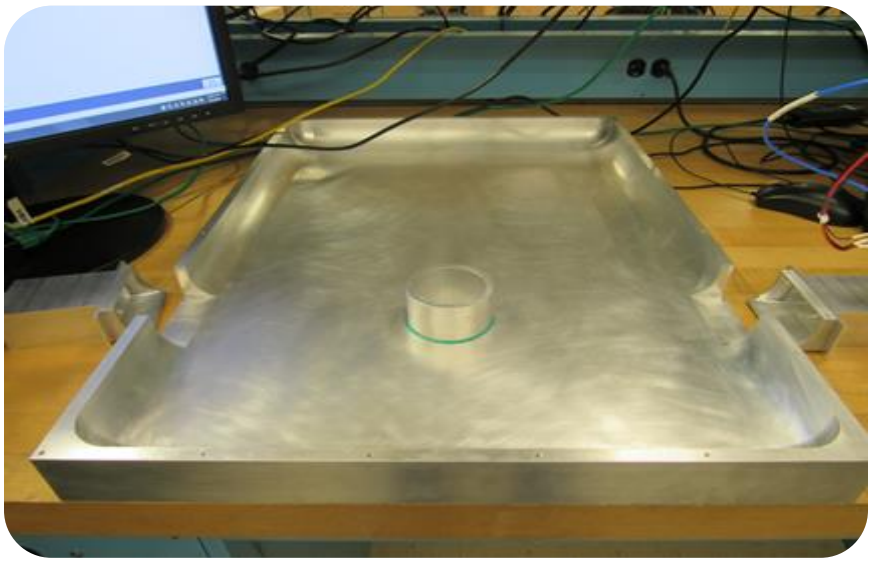

(a)

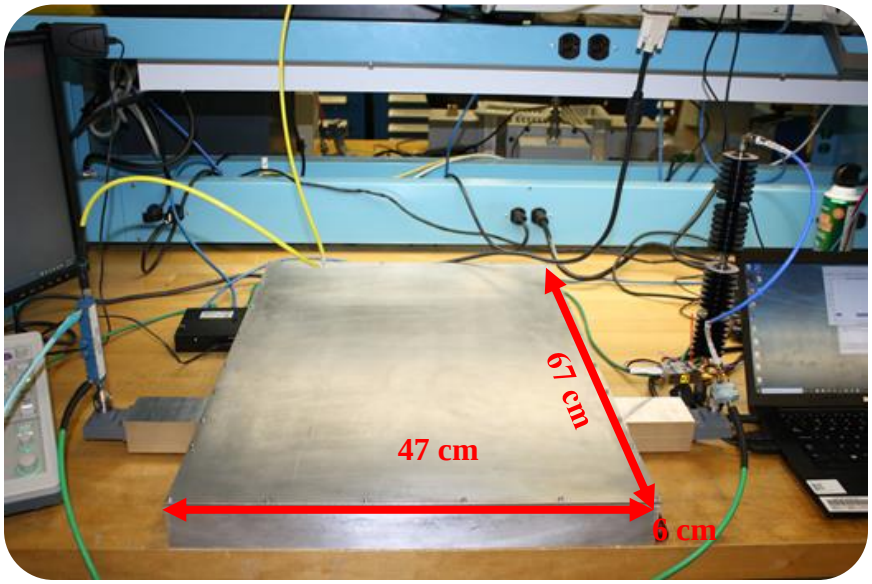

(b)

Figure 3-4. (a) The pulse compressor cavity is machined out of solid block of aluminum for rigidity to reduce perturbations due to deformation of the cavity, as would happen with thin-plate sides. (b) Pulse compressor (dispersive cavity) outer dimensions are 67 cm x 47 cm x 6 cm with a dual-directional coupler on the input and an attenuation shunt on the output for increased dynamic measurement range on the oscilloscope.

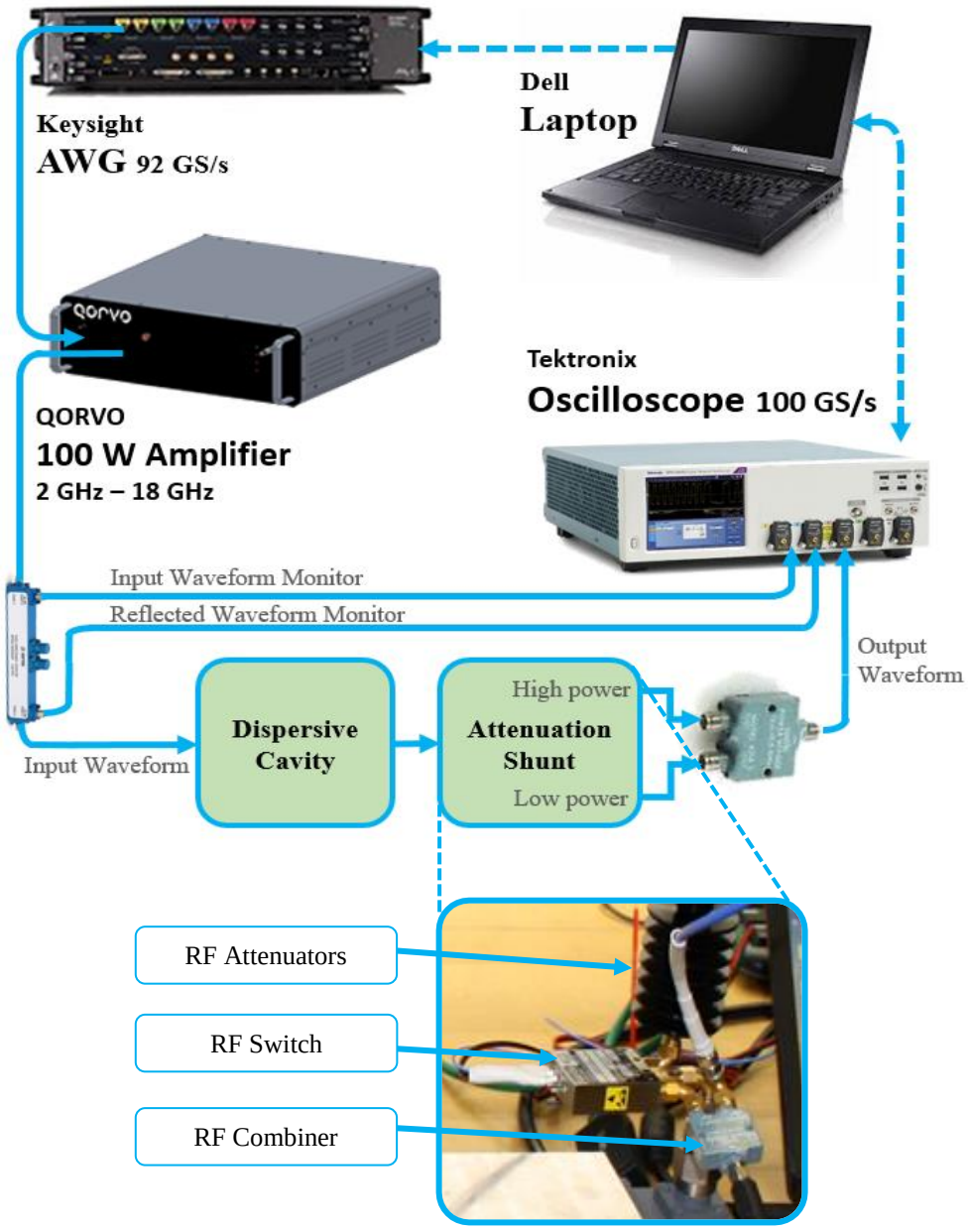

Figure 3-5. Experimental setup and signal flow diagram. The attenuation shunt is used to switch attenuation for low output power when measuring impulse response to more attenuation for high output power when measuring one-bit TR output signal.

3.3 - Measurement of the Cavity Compression Gain

The first step in the experimental pulse compression process is to program the AWG with the sinc function that has 5 – 18 GHz of bandwidth. This signal is seen in Figure 3-6(a) and its spectrum is seen in Figure 3-6(c). The AWG then sends the signal to the wideband amplifier. After transmitting the amplified excitation signal into the cavity, the impulse response due to the USP excitation is recorded from the oscilloscope, Figure 3-6(b), and its spectrum is also shown in Figure 3-6(c). The insets show detail of the excitation and IR, which can be seen to have some 'roll-off' as frequency increases. This is due to the fact that the AWG, the cables, and the cavity have frequency responses that 'roll off' at higher frequencies. Also, the inset to Figure 3-6(c) more clearly shows the frequency response of the amplifier, which is negligible compared the frequency response of the AWG. In addition, the phase shift of the amplifier was measured, but it too was found to be negligible.

Next, Figure 3-6(d) shows the time-reversed impulse response and the one-bit-processed response. Initially, the OBTR signal has high frequency content due to the discontinuities where it transitions from maximum to minimum, but this content will be filtered out due to the narrower system bandwidth. Performing OBTR past the impulse response can actually lead to increased time-sidelobes, but here only high-gain and high peak-power are of interest. Figure 3-6(e) shows the long-duration, low-peak power input and the reconstructed impulse with a 1400 V peak instantaneous voltage (both measured on the oscilloscope), which is 39.2 kW of instantaneous peak power for this 50 Ω system, and a record for this type of pulse compressor in the published literature. Figure 3-6(f) shows the spectrums of the OBTR excitation and reconstruction. The peak instantaneous voltage of the long-duration input was 122.3 V. So, using (2.5), with the numerator being 1400 V and the denominator being 122.3 V, gives ~21.2 dB of compression gain.

For time reversal pulse compressors, the peak output power is proportional to the magnitude of the input power, such that given an equivalent system, a higher peak input voltage will produce a higher peak output voltage. Nonetheless it is useful to compare the TR pulse compressor described in this dissertation with others described in the literature. This result is compared with compression gain results from other works in Table 3-1 at the end of section 3.4.

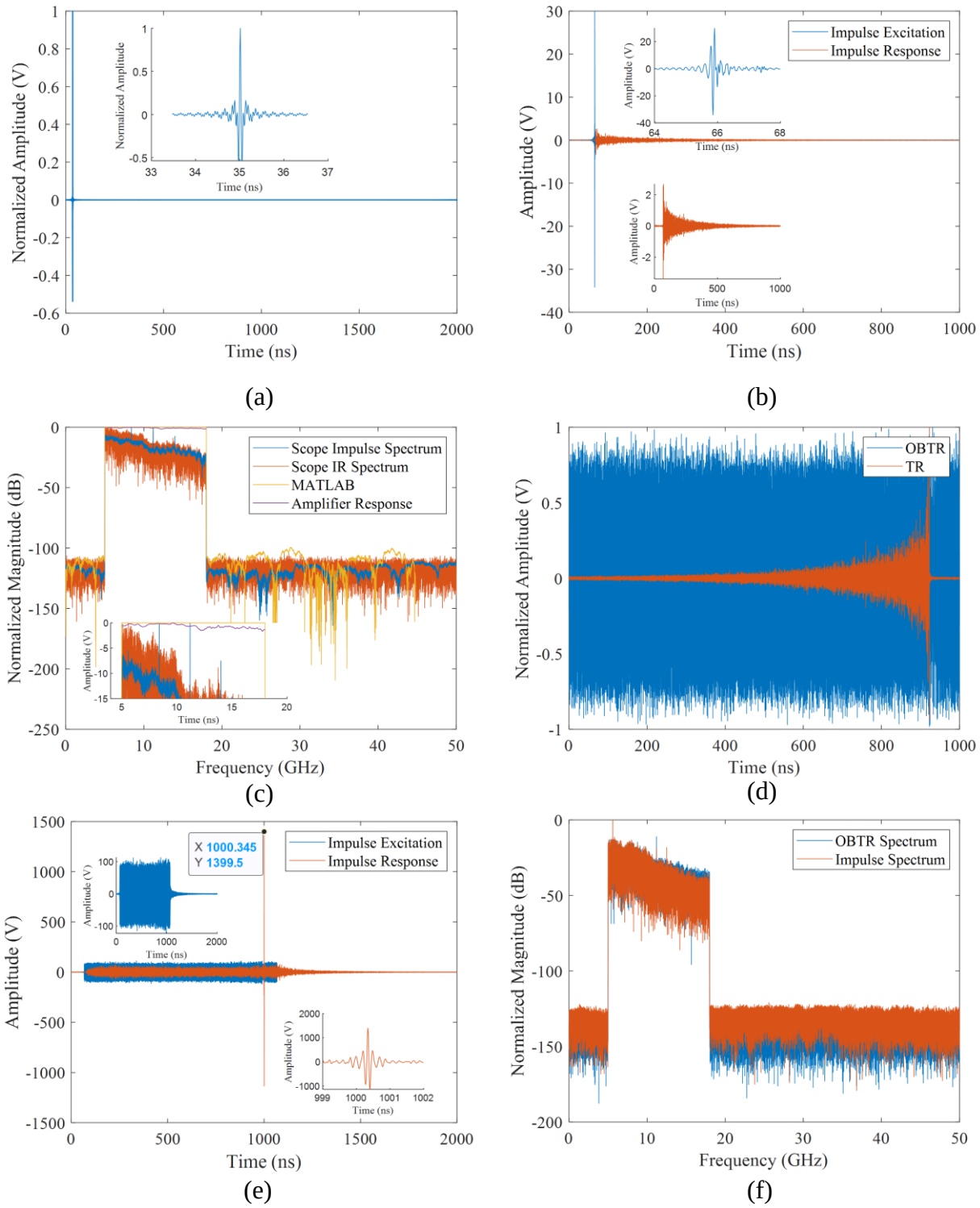

Figure 3-6. OBTR process and pulse reconstruction: (a). USP as programmed in the AWG; (b). Amplified signal transmitted into the cavity and the to-scale impulse response (inset shows zoomed in signals); (c). Spectra of signals in a) and b); (d). TR signal and OBTR signal (filtered to 13 GHz BW) sent to AWG; (e). Amplified OBTR signal and reconstructed impulse response showing 21.2 dB of gain and a peak output voltage of 1400 V; (f) Spectra of OBTR and Reconstructed Impulse.

3.4 - Analysis of Cavity Efficiency from Simulated and Measured Results

Compression gain is the primary figure of merit of interest here, but analyzing how various loss mechanisms contribute to decreased efficiency, and thus decreased gain, is instructive. Cavity efficiency has been discussed in [30]. Here, the cavity efficiency, η_{cav}, if of interest, which is defined as in [29] as the ratio of the total energy in the cavity output signal (the reconstructed impulse plus time-sidelobes) to the total energy in the input signal (the one-bit time-reversed signal):

$$\eta_{cav} = \frac{\int_{t=0}^{t=T} y(t)^2 \, dt}{\int_{t=0}^{t=T} \{sign[h(-t)]\}^2 \, dt} \tag{3.1}$$

where $\eta_{cav} = 1$ would mean that all the energy in the OBTR input would be converted to the high-peak USP output and its time-sidelobes. For the simulated cavity (with aluminum conductivity) the calculated efficiency using (3.1) is 36%, compared to the fabricated pulse compressor which has an efficiency using (6) of 22%. This value for efficiency compares favorably with other TRPC cavities in the literature as given in Table 3-1 at the end of this section.

There are four ways for energy to fail to reach the output thus reducing its efficiency: 1) reflection at the input; 2) returning to the input after one or more reflections in the cavity; 3) leaking from the seams around the lid and feeds; and 4) Ohmic losses. Reflection at the input is characterized by the reflection coefficient (S_{11}), though this also includes energy that has entered the cavity and returned to the input. Energy that exits at the output port is characterized by the transmission coefficient (S_{21}). Energy that enters the cavity, but does not exit through either port, and is not absorbed, has leaked out of the cavity. This quantity when combined with the energy lost interacting with the cavity walls (Ohmic losses) is characterized by absorptance (or total loss), α, which is determined as

$$\alpha = 1 - |S_{11}|^2 - |S_{21}|^2 \tag{3.2}$$

Figure 3-7 shows the reflectance ($|S_{11}|^2$), transmittance ($|S_{21}|^2$), and absorptance (Eq. (3.2)) of the both the simulated and measured aluminum cavities (measured S-parameters were

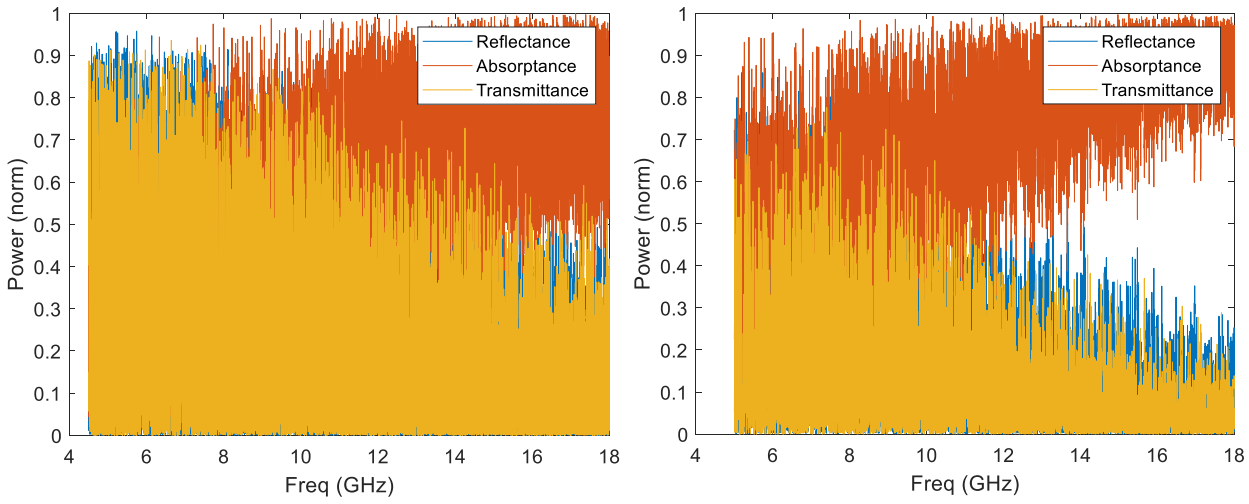

(a) (b)

Figure 3-7. (a) Reflectance, absorptance, and transmittance of the pulse compression cavity as a function of frequency for simulate, (b) and measured aluminum cavities.

determined on a vector network analyzer (VNA)) in order to give insight into how much of the total energy incident on port 1 contributes to the output signal, and thus to the compression gain. It can be seen that all of these quantities are frequency dependent such that the cavity is more efficient for lower frequencies. This is also apparent as there is higher absorption as frequency increases. Here cavity efficiency, η_{cav}, is equivalent to the transmittance. By summing the energy in each of the three quantities, and dividing each by the total energy measured it is found that for the simulated cavity 26.4% is reflected, 49.4% is absorbed (and leaked), and 24.2% is transmitted, whereas for the measured cavity 18.5% of the energy is reflected, 67.5% is absorbed (and leaked), and only 14% is transmitted. These results suggest that, while reducing reflected energy could lead to more energy in the cavity, and a possibility of higher compression gain, reducing absorbed and leaked energy has the greatest potential for increasing gain. Also, neglecting any potential effects due to machining tolerances that may cause design differences between the measured and simulated cavities, the simulated cavity has more reflected power, and less absorbed (and no leakage). This should be expected as the simulated cavity has no seams where parts are joined together, meaning that not only will less energy escape without being reflected or transmitted, but more energy will have an opportunity to be reflected and return to port 1. However, even with more energy being reflected, there is still higher transmission, which explains the higher compression gain in simulation (27 dB simulated vs 21.2 dB measured) and suggests that reducing

leakage in the measured cavity by better sealing or eliminating seams will contribute to higher gain. Further evidence for leakage from the measured cavity comes from high measured electric field values (using a Narda 3-axis probe) at both the input adapter interface, and around the lid/cavity seam.

Table 3-1. Comparison of Other EM TR Pulse Compressors in the Literature with This Work.

TR Pulse Compressor	*Vout, pk (V) /Vin, pk (V)*	*Center Frequency (GHz)*	*BW (GHz)*	*Compression Gain (dB)*	*Efficiency (%)*	*Cavity Volume (cm^3)*
This Work	1400/122.3	11.5	13	21.2	22	11,151 (compact)
Vallon [30]	1100/110[a]	1.3	0.3	19.8[b]	<10[a]	1,680,000 (large)
Hong et al. [29]	2.4/0.25	5.5	7	19.7	<10	~7400 (compact)
Hong et al. [31]	3.2/1	6	8	10.2	<10	81.9 (planar, semi-2D)

[a] Estimated from figures in [30]

[b] For the cavities in [29], [31], and this dissertation, compression gain is found by oscilloscope measurements at the input and output of the cavity and equation (2.5). In [30], the output was measured as radiated from the cavity on a D-dot probe at a distance of 1 m, and the stated power density at this distance was 3 kV/m. From this information, it could not be verified that the 1100 V shown in [[30], Fig. 4.58]; the gain is simply stated here as reported by the author.

3.5 - Investigation of the Effect of Variation of IR Recording Time and Signal Bandwidth on Compression Gain

The frequency dependence of the cavity power transmission, $|S_{21}|^2$, shown in Figure 3-7 also suggests that there may be an optimum spectral width beyond which there is no measurable increase in compression gain. Recognizing that S_{21} is also the transfer function for this 50 Ω system, a numerical investigation was undertaken to show how compression gain changes as bandwidth increases. Two numerical experiments were performed. In the first, sinc excitations were applied to the measured cavity transfer function beginning with an excitation having 100 MHz bandwidth from 5.0 to 5.1 GHz to obtain the cavity impulse response. The compression gain was determined by applying the OBTR process to the impulse response and then applying the

OBTR signal to the transfer function again. In this manner the gain was determined for increasing bandwidths up to 18 GHz in 100 MHz increments. The results can be seen in Figure 3-8 such that that the maximum gain of ~20 dB is obtained when the maximum frequency is ~13.5 GHz. It remains so, and even begins to decease as the maximum frequency passes ~16 GHz.

To gain insight into this 'gain saturation', a similar numerical experiment was performed where the excitation bandwidth was now varied by holding the *stop* frequency constant at 18.0 GHz and, beginning with 5.0 GHz, increasing the start frequency by 100 MHz on each experiment. The results can be seen in Figure 3-9. It is evident that as the start frequency is increased, the gain begins to reduce. This curve however is not the opposite of that in Figure 3-8, and in fact the gain is less <1 when the bandwidth is 17.9 to 18 GHz. This correlates well with the results from Figure 3-7, which shows that absorption in the cavity is greater at higher frequencies. These results suggest that when balancing increased gain and reduced pulse width (increased bandwidth) it is more efficient to use a lower start frequency than a higher stop frequency for a given bandwidth.

Finally, a third numerical experiment was undertaken wherein the bandwidth was held constant at the original 5 – 18 GHz bandwidth and the impulse response record time varied from 10 ns to 6 µs in 10 ns increments. This is similar to the format of the simulation results presented earlier in Figure 3-3. The results are shown in Figure 3-10. The results show that (for this cavity

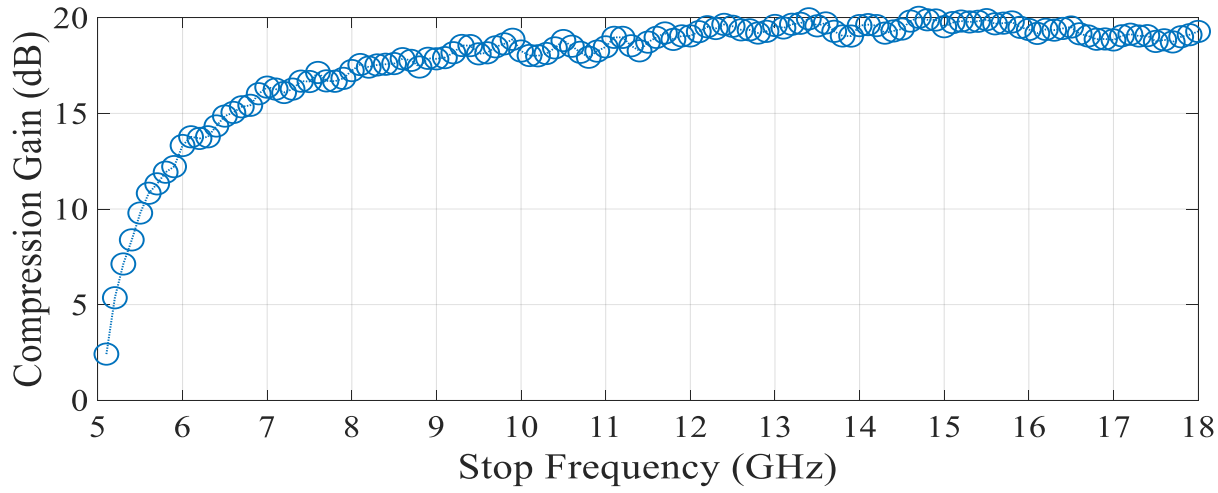

Figure 3-8. Compression gain as a function of *increasing* excitation signal bandwidth. Keeping the *start* frequency at 5 GHz, the *stop* frequency is varied from 5.1 GHz to 18 GHz in 100 MHz increments, and the pulse compression gain is noted. Impulse response length was 1 µs.

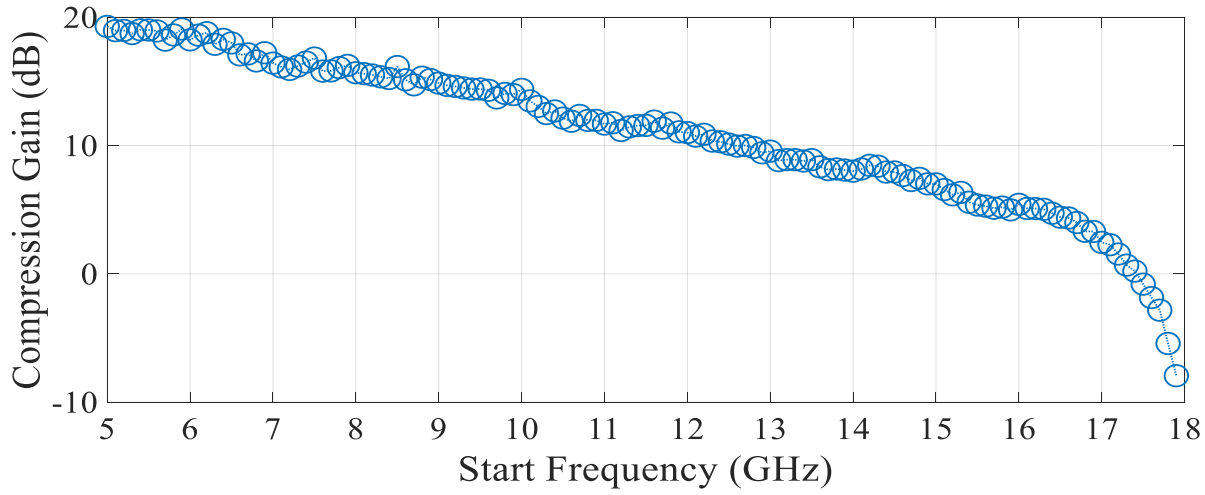

Figure 3-9. Compression gain as a function of *decreasing* excitation signal bandwidth. Keeping the *stop* frequency at 18 GHz, the *start* frequency is varied from 5.1 GHz to 18 GHz in 100 MHz increments, and the pulse compression gain is noted. Impulse response length was 1 µs.

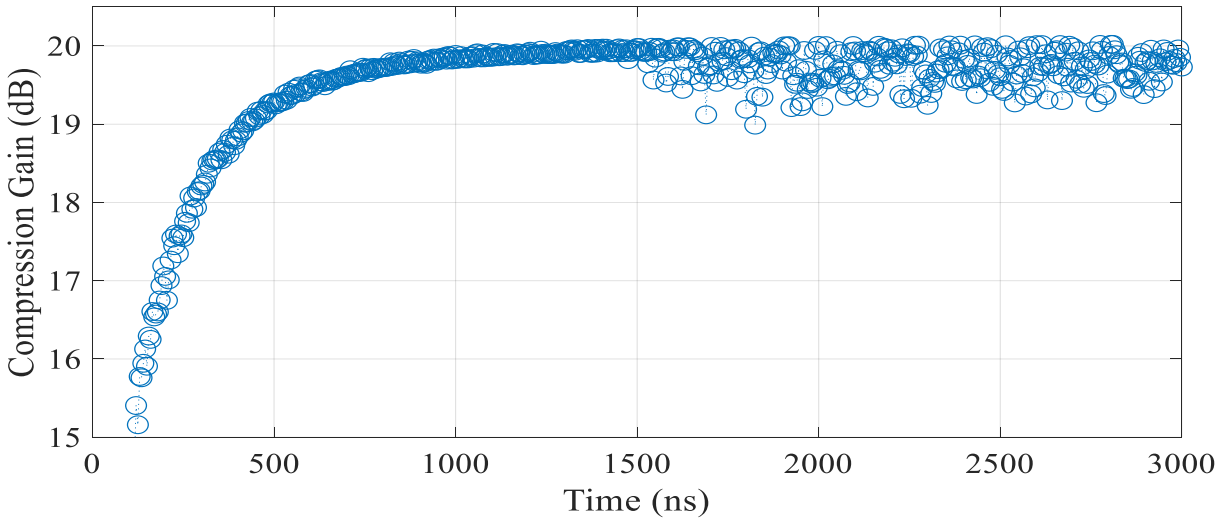

Figure 3-10. Compression gain as a function of *increasing* impulse response recording time. Keeping the bandwidth constant (5 GHz – 18 GHz), the record time is varied from 10 ns to 6 µs in 10 ns increments.

configuration, input power levels, and measurement resolution) there is no benefit, and in some cases a penalty, for recording longer than 1500 ns. This is because, at this IR length, the signal has decayed below the noise floor of the recording oscilloscope and the OBTR process is only digitizing noise, which does not contribute to increased gain.

These results are important because in this type of pulse compressor the maximum pulse repetition frequency (PRF) is determined by the length of the impulse response. For example, with 1 us impulse response the associated PRF is 1/1us = 1 MHz. By knowing the maximum effective impulse response length, one may achieve an optimal PRF while maximizing compression gain.

3.6 - Cavity Geometry Optimization

It was seen in [29] that, at many mode-stirrer positions, the gain of the cavity approached a mean of ~17 dB, but there were several positions where the gain was significantly higher (the highest was 19.6 dB). The mode stirrer is a thin piece of metal which when rotated provides a different internal geometry (thus different boundary conditions) with equivalent volume. The results from [29] show that cavity geometry can be important factor regarding increasing compression gain. Also, statistical models exist in the literature describing the quality factor of overmoded cavities as a function of the position of a geometry altering mode-stirrer [40], [41], and consequently of a changing transfer function from one port to another. This can lead to variations in compression gain, which can be optimized. To investigate this phenomenon in relation to this pulse compression cavity, a single-paddle mode stirrer was added to the cavity. The mode stirrer is controlled by a stepper motor as seen in Figure 3-11, and pulse compression measurements were taken for 200 different stirrer positions. The results are also plotted in Figure 3-11.

The 200 different stirrer positions produced a maximum gain of 19.7 dB and a minimum gain 17.6 dB with a mean of 18.9 dB. This shows ~2 dB of compression gain variation over all positions. However, this maximum value of 19.7 dB is 1.5 dB less than the 21.2 dB for an empty cavity, due to non-optimal stirrer location and position, and additional Ohmic losses from the added surface area of the stirrer paddle. These results alone are indeterminate as to whether the mode-stirrer absolutely reduces the gain beyond the ability of a stirrer to optimize it to a higher value, or whether the stirrer is simply placed in a poor position, or whether additional mode stirrers are required for more variability in modifying the wave propagation. In [29], a similar maximum gain of 19.6 dB was achieved, however the mean gain was lower at 17 dB with a minimum gain of 14.6 dB (a variance of 5 dB), and they did not report data for a cavity with no stirrer.

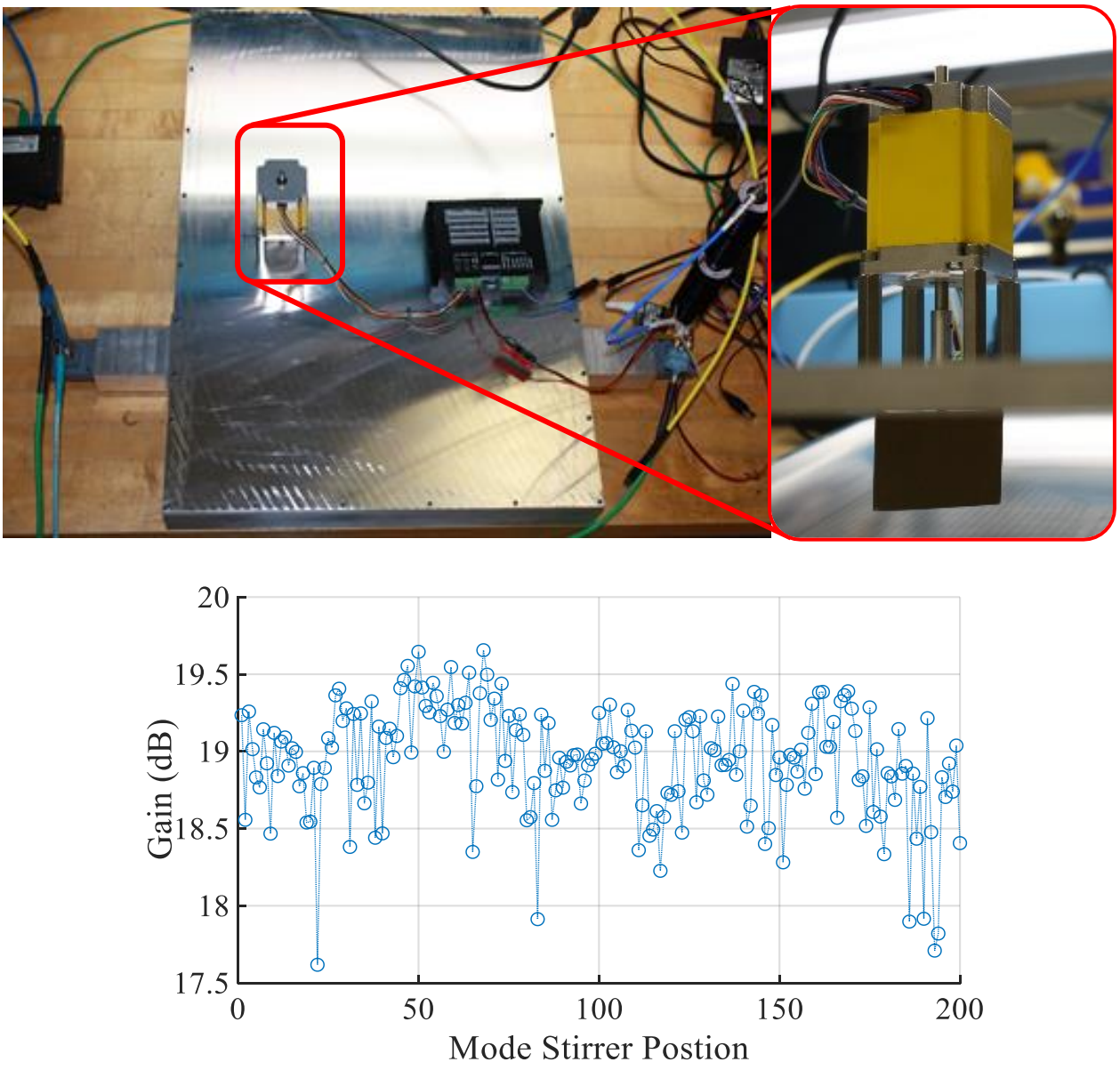

Figure 3-11. Compression Gain over 200 different stirrer positions. Mode stirrer is automatically controlled using MATLAB and a stepper motor such that the entire pulse compression process is accomplished through automated equipment control. Gain is seen to vary from 17.6 dB to 19.7 dB with a mean of 18.9 dB. Inset shows single-paddle mode stirrer attached to shaft below lid.

In order to investigate whether mode-stirrer *location* is significant regarding compression gain increase over mode stirrer paddle *position*, the mode-stirrer was moved to a new location, and the experiment with 200 stirrer positions was repeated. The results are shown in Figure 3-12. A maximum compression gain of 21 dB was obtained, which is 1.3 dB higher than that achieved with the mode-stirrer at the previous location. This suggests that not only is cavity geometry an

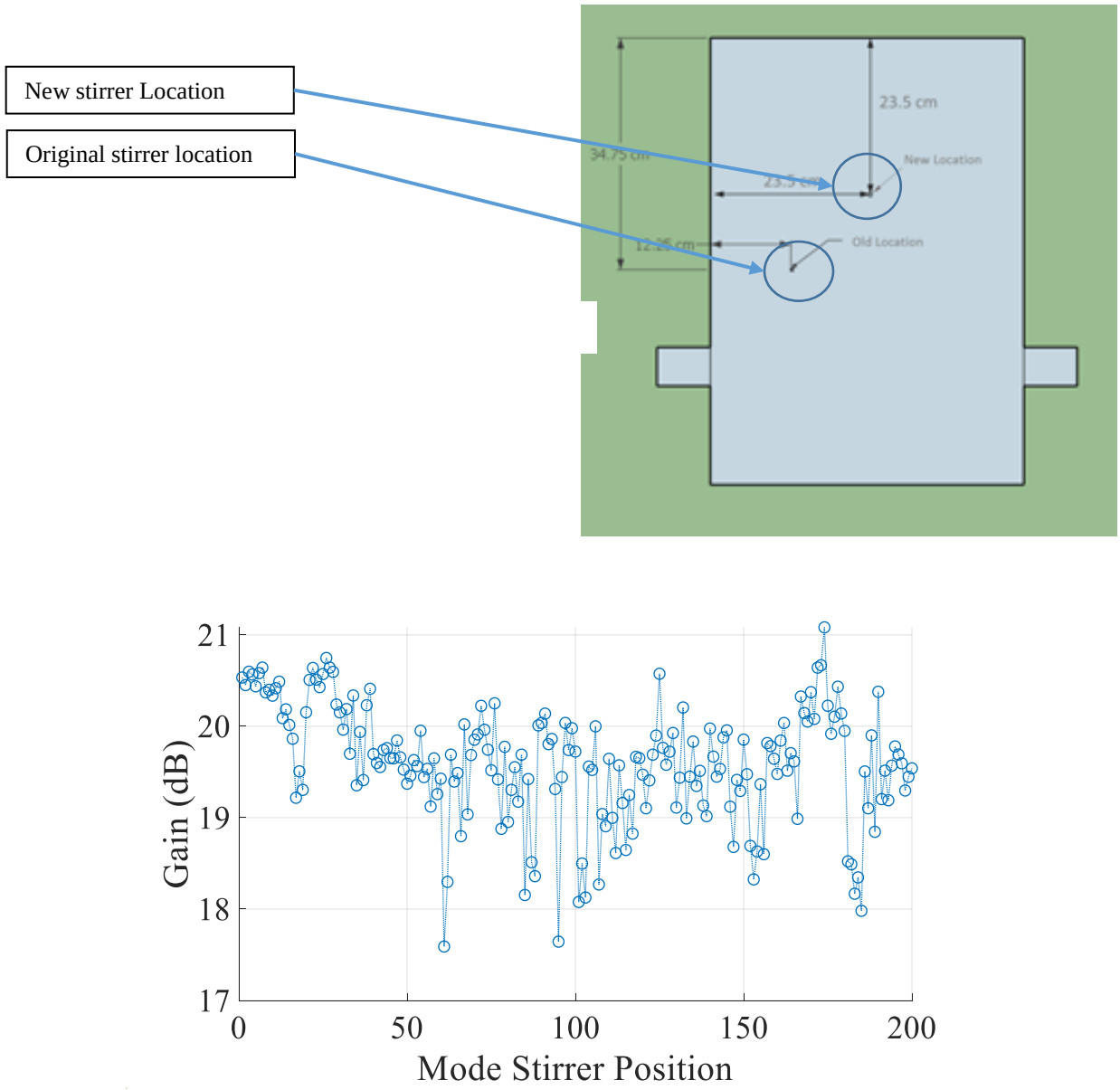

Figure 3-12. Compression Gain over 200 different stirrer positions at new stirrer location. Gain is seen to vary from 17.6 dB to 21 dB with a mean of 19.6 dB

important factor in compression gain, but that a single mode-stirrer at a single location does not provide enough variability to find the 'best' configuration for the 'highest' compression gain. It should be noted that no analytical solution exists for the *optimal* geometry or stirrer postion. In [42], a model was devloped that predicts the *statistics* of the signal-to-noise (SNR) ratio of the reconstructed signal as a non-perturbative receiver is moved around the cavity, but here, with each rotation of the stirrer, the modal weights of the transfer function change. Thus, due to the wave-chaotic nature of the cavity, it is not possible to predict the optimal placement of the stirrer.

Finally, as was seen in [29] and shown here, changing the internal geometry of a cavity can alter the compression, in some instances (realizations) leading to increased gain. However this has been shown only for a single-mode stirrer with a single optimization parameter, the angle of rotation. This led to the conjecture that having a multi-parameter optimization method could lead to finding an optimal cavity geometry for optimal compression gain. For example, a cavity with a series of metal posts that could be raised or lowered according to the output of a genetic algorithm was devised but two issues were found that showed that this technique would not ultimately be beneficial in practice. First the seams around each post could not be sufficiently shielded to prevent additional loss, and second the increased surface area and reduced volume led to reduced gain. These two factors led to a significant reduction in gain that could not be overcome by optimization. These efforts are further described in Appendix A for completeness, but were not pursued further as an alternative, more practical approach to improving compression gain was developed.

3.7 - Summary

In this chapter, a new design for a compact, high power pulse-compression cavity that operates with an instantaneous BW of 13 GHz (5–18 GHz) has been presented. Results from both full-wave simulations and measurements from a fabricated cavity were shown. With an un-optimized cavity 21.2 dB of compression gain was obtained using a 100 W peak-power sinc impulse function to get 39.2 kW instantaneous peak power output was shown. This is also the highest reported gain and peak output power for a pulse compressor of this type. This empty cavity is currently inefficient with an efficiency of about 22%, though this is higher efficiency than other similar pulse compressors. In a novel experiment, the internal geometry was optimized using a single-paddle mode-stirrer to obtain increased compression gain, but this resulted in a maximum gain that was 1.5 dB lower than the cavity with no mode-stirrer. The mode stirrer was then moved to a new location and the experiment repeated to achieve a higher gain compared with the empty cavity. Variation in compression gain to due to variation in the impulse response recording time and signal BW was also investigated.

In Chapter 4, the fidelity of the output waveform with respect to the input waveform will be discussed. Also discussed are the concept of time-sidelobes, and a novel technique for reducing them when using OBTR is presented.

Chapter 4 - Cavity Input-Output Fidelity and Time-Sidelobe Reduction

If the entire OBTR process is viewed as an amplification process as in [43], [30], then it is natural to compare the fidelity of the 'amplified' impulse to the unamplified impulse. Figure 4-1 shows the original impulse, a normalized excitation impulse, and a normalized OBTR reconstructed impulse. The yellow signal is the original impulse that was generated in MATLAB and sent to the AWG. Some significant features can be observed that differ from the excitation impulse that was sent from the AWG to the cavity input, but there is decent fidelity between the excitation impulse and the reconstructed impulse.

In a time-reversal pulse compressor where there are no losses in the walls (e.g. PEC in simulation or super-cooled/superconducting in practice), the compressor would exactly reconstruct the original excitation impulse *plus* any distortion from information lost at the input port due to energy being reflected by the cavity and returning to the port (i.e., not transmitted to the output). These distortions are referred to as *time-sidelobes* and are described in [38], [44], and elsewhere, and are referred to in part as noise in [42].

For a real-world experiment on a fabricated cavity (or even a simulation with finite conductivity), the situation is not ideal. Now, Ohmic loss (and leakage, for a real experiment) further degrade the fidelity of the impulse response. This degradation in either the lossless or lossy scenario comes in the form of further time-sidelobe distortion in the reconstructed impulse. But for a regular TR process, the time-sidelobes are minimal compared to those created by the one-bit time-reversal process. Figure 4-2 shows impulse reconstructions completed numerically using the transfer function method for both a PEC cavity and an aluminum cavity. As both signal processing (one-bit processing) and conductivity are added, time-sidelobes increase as all of these processes introduce phase error and thus 'imperfect' constructive interference at the output.

Time-sidelobes are thus an inherent feature of the TR pulse compression process, and it is useful to discuss methods for reducing them, especially if these waveforms are to be used for radar applications where high time-sidelobes can adversely affect radar detection thresholds. Time-sidelobe reduction using iterative time reversal was first introduced in acoustics in [45] and then in electromagnetics in [46]. The procedure begins by subtracting the original impulse from the

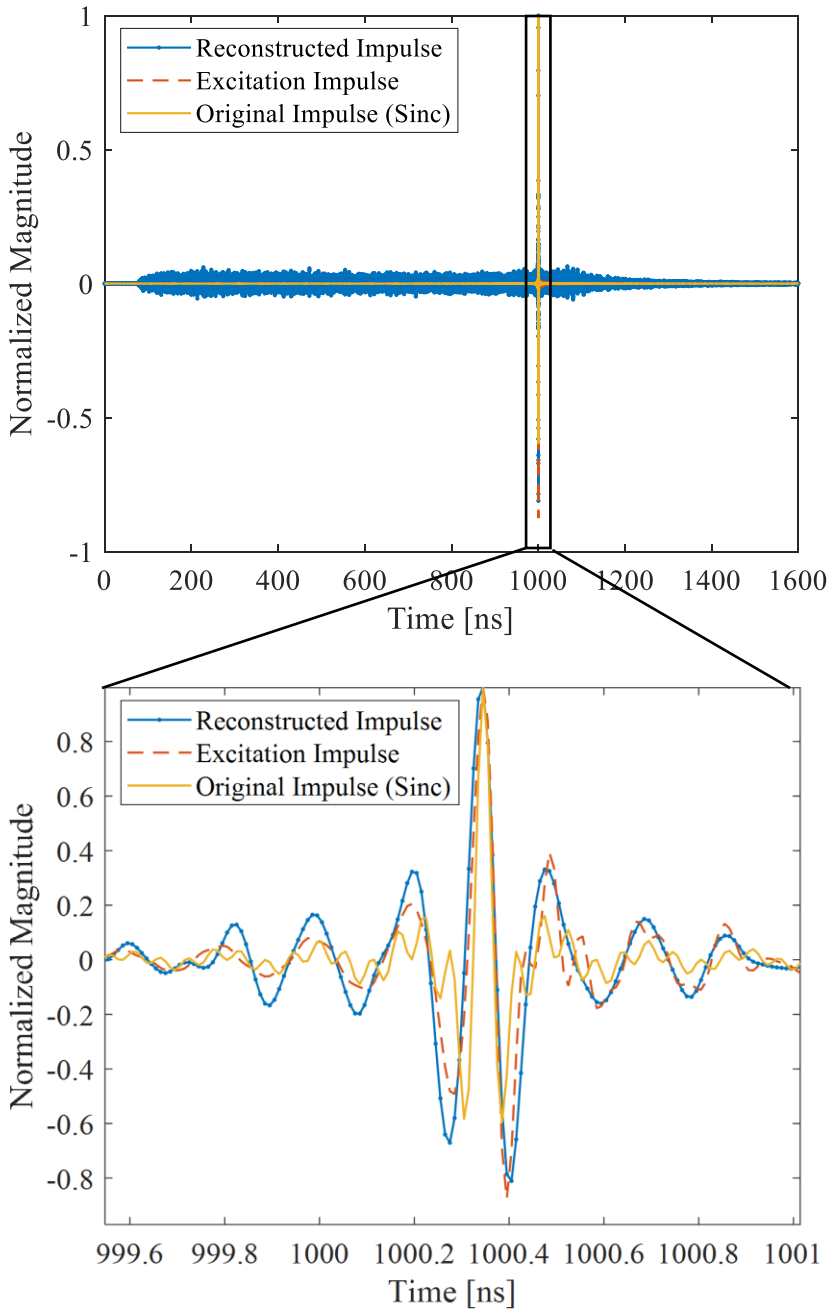

Figure 4-1. Original waveform, excitation waveform, and reconstructed waveform seen overlaid on each other (top) from the measured cavity. There is good fidelity between the reconstructed impulse and the excitation impulse, but there are certain features of the original impulse sent to the AWG that differ (bottom).

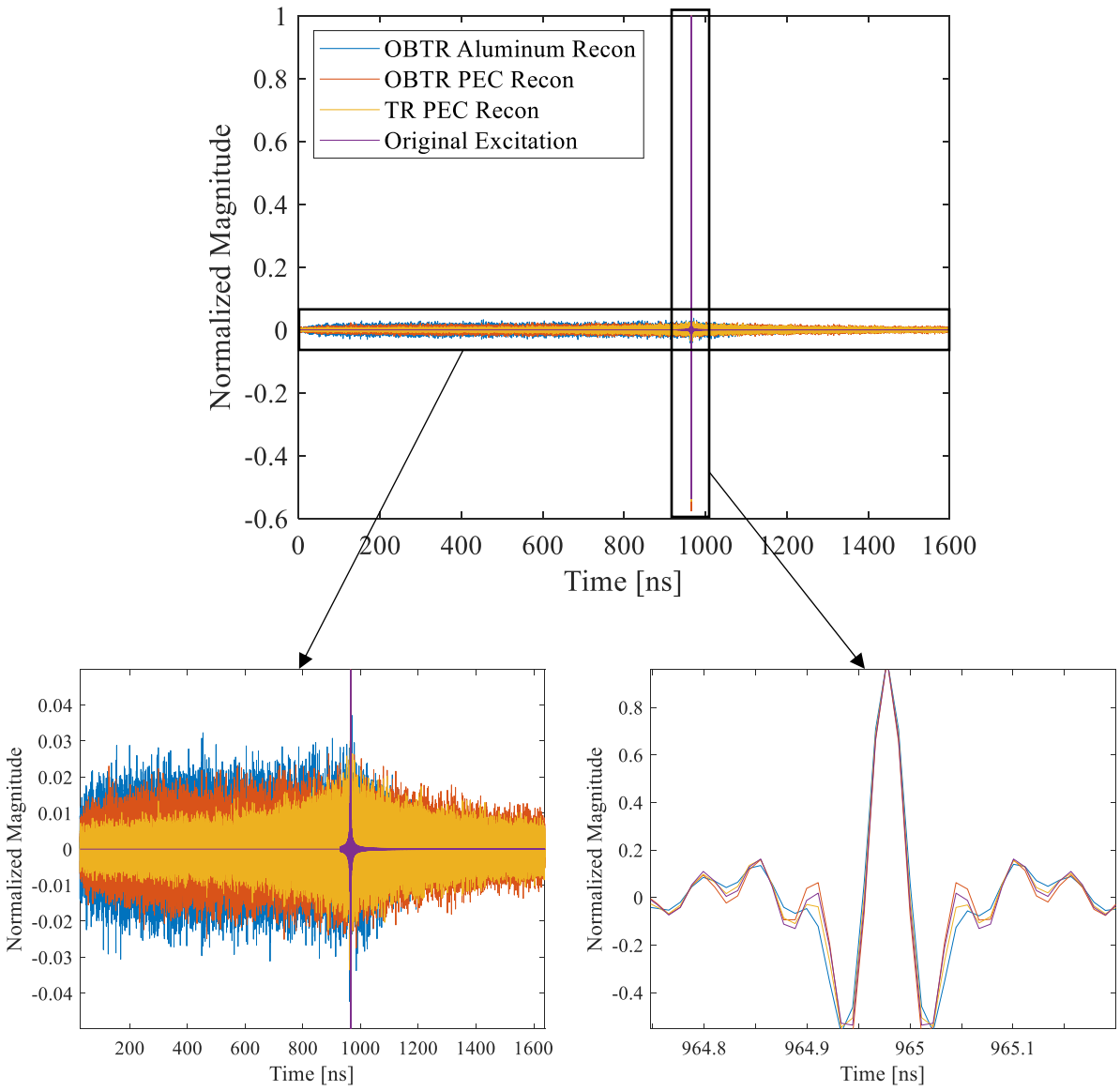

Figure 4-2. Excitation impulse, OBTR reconstructed impulse from simulated aluminum cavity, OBTR reconstructed impulse from simulated PEC cavity, and TR reconstructed impulse from simulated PEC cavity (top). Time-sidelobes for all cases in top (bottom left). Zoom in of reconstructed impulse for all cases in top (bottom right).

initial reconstructed impulse. This signal is called the 'sidelobe signal.' As described in [39], this sidelobe signal is time-reversed and retransmitted into the cavity, and the response is then subtracted from the previous IR. This new IR has thus had sidelobe-causing amplitude information removed and the new reconstructed signal will now have lower time-sidelobes. This iterative process can be repeated indefinitely to further reduce the time sidelobes. However, this process

only works well for non-OBTR signals because of the loss amplitude information inherent in applying the one-bit process on each iteration.

4.1 - Time-Sidelobe Reduction for OBTR

For one-bit TR signals, other methods must be used. Using an innovative approach not previously published in the literature, in this work a fast, reflective PIN-diode switch was placed on the cavity input (before the dual-directional coupler in Figure 3-5) such that after the original impulse is transmitted the switch closes after 10 ns. This serves to increase the energy in the recorded impulse response, potentially leading to increased gain. Then, after recording the impulse response and performing OBTR, the signal from the output port was transmitted back to the switch-enabled input port such that the fast RF switch opens after 990 ns (for a 1 μs recording time) just in time for the impulse to reconstruct, but with virtually no sidelobes due to the fact that the port was reflective for the first 990 ns.

Figure 4-3 shows a diagram of this process, which can be further described by defining $y_{IR}(t)$ to be the recorded impulse response and $y_{TR}(t)$ to be the reconstructed impulse such that in the ideal case

$$y_{IR}(t) = \begin{cases} h_1(t) * af(t), & t < t_{swF} \\ h_2(t) * af(t), & t \geq t_{swR} \end{cases} \tag{4.1}$$

and

$$y_{TR}(t) = \begin{cases} 0 & t < t_{swR} \\ h_1(t) * af(t), & t \geq t_{swF} \end{cases} \tag{4.2}$$

where $h_1(t)$ is the impulse response of the cavity terminated with matching 50 Ohm loads, $h_2(t)$ is impulse response of the cavity with port 1 terminated with a short (reflective) and port 2 still 50 Ω, t_{swF} is the switch time of the fast switch , and t_{swR} is the IR recording time minus t_{swF}.

Figure 4-4 shows that more energy was able to be stored in the cavity thus leading to a higher-energy impulse response (31.1 pJ of total energy for the 'higher-Q' scenario with switch closed, and 13.5 pJ for the 'lower-Q' cavity with switch open). This larger impulse response could

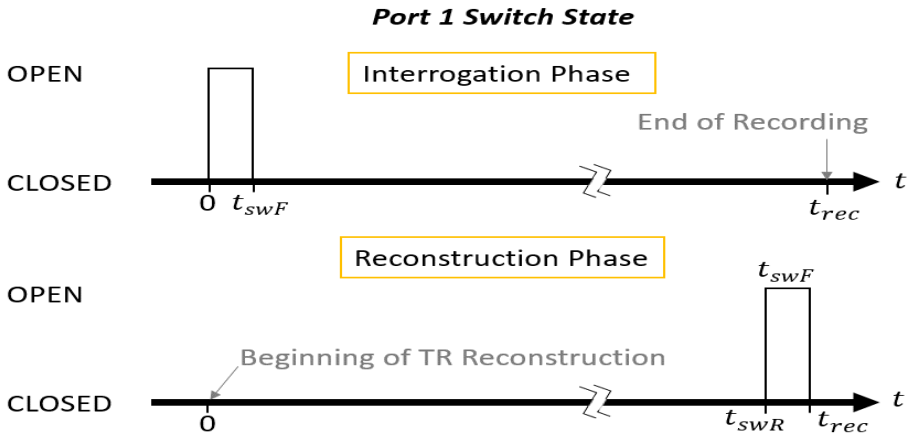

Figure 4-3. Diagram of switch state for OBTR sidelobe reduction. During the interrogation run, switch becomes reflective after forward switching time, t_{swF}. During the reconstruction run it remains reflective for the reverse switching time, t_{swR}, and becomes 50 ohms for the last period of length t_{swF}.

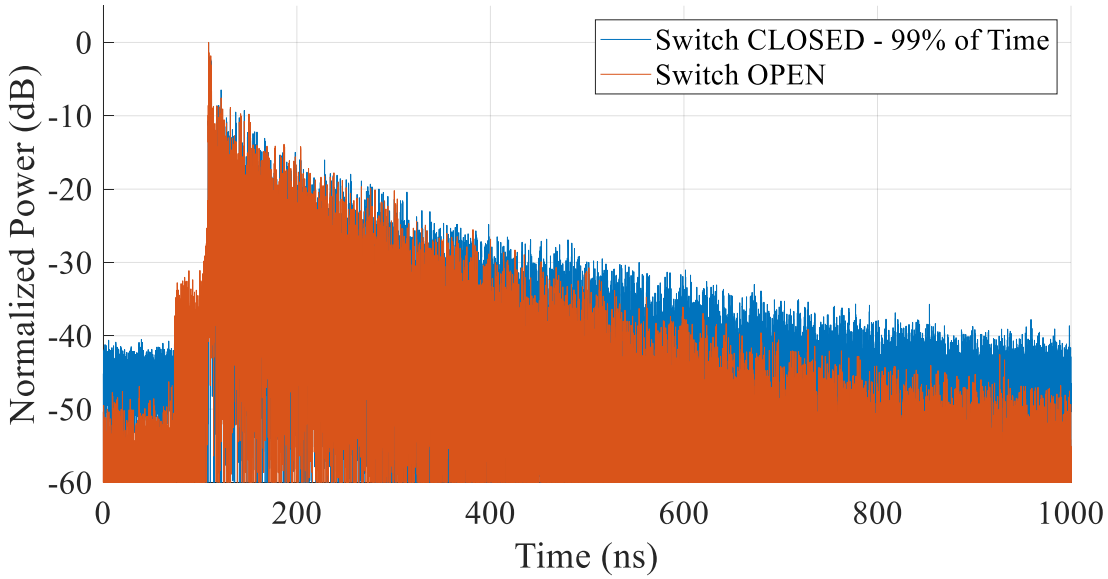

Figure 4-4. Impulse response when PIN diode switch was closed for 990 ns out of 1000 ns showing more energy than the impulse response with no PIN-diode switch open the for the whole 1000 ns.

potentially lead to higher gain, but as will be explained, a higher gain was not seen in this implementation. The time-sidelobes were indeed eliminated as expected, Figure 4-5. However, an unforeseen consequence of using a PIN-diode switch was that the impulse reconstruction, being of high amplitude, caused the PIN-diode switch to behave as a PIN-diode limiter. Non-PIN diode coaxial microwave switches may be used as well such as micro-electromechanical systems (MEMS) and monolithic microwave integrated circuit (MMIC) switches, but even these have low maximum average power thresholds.

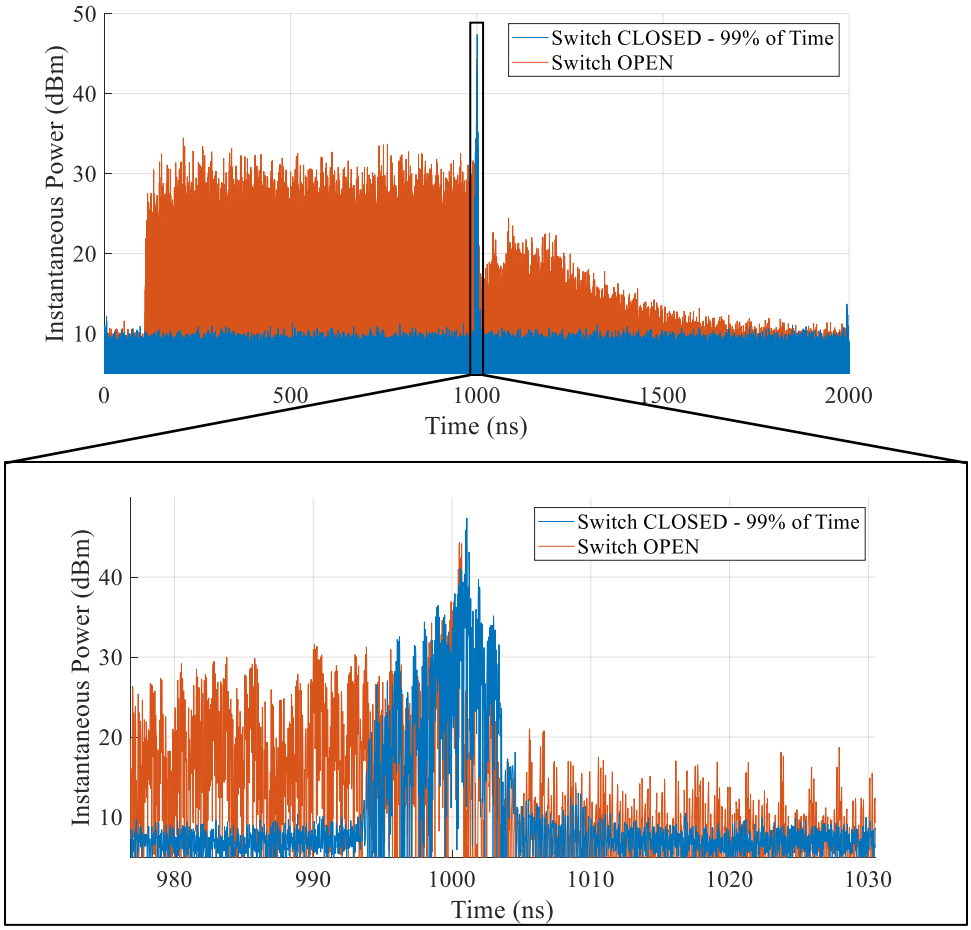

Figure 4-5. Time-sidelobe reduction is evident in the inset during the 990 ns period where the switch was closed, and the reconstruction begins after this time. Reconstruction truncation due to PIN-diode switch is also evident and peak power should be 10s of kW, not 10s of W.

4.2 - Summary

In this chapter, the input and output waveforms were compared to show how the TRPC process affects waveform fidelity. Then, a novel technique was presented for reducing time-sidelobes when using the OBTR process. This technique is effective for not just reducing time-sidelobes when using OBTR processing, but for effectively eliminating them. However, with current microwave switch technology, this technique may only be used for low power operations. Appendix B provides further experimental observations showing that, while this is effective at low power levels, it may not be used for power levels beyond which the fast microwave switches are rated.

Chapter 5 - Pulse Compression using Time Reversal Techniques in a Single-Port Cavity

In Chapter 3, a compact, high-power pulse compression cavity was presented that achieved 21.2 dB of compression gain. However, this cavity, like all prior TRPC demonstrations in cavities in the literature, has two ports: one input feed, and output feed. As has been discussed, time-reversal pulse compression (TRPC) in a two-port (2-port) cavity takes advantage of the fact that a dispersive cavity acts an autocorrellator for its own time-reversed impulse response. The standard method for TRPC is described in section 2.3, and is depicted for a 2-port cavity in Figure 5-1. As discussed previously, compression gain may be further increased by using OBTR to add additional energy to the time-reversed IR before retransmitting into the cavity.

However, in a 2-port cavity, regardless of whether one uses regular TR or OBTR, not all the energy transmitted into the cavity using the input port propagates to the output port. In addition to Ohmic losses and cavity leakage through insufficiently sealed seams, a portion of the energy that enters the cavity is internally reflected and returns to the input port. This lost energy does not contribute to the IR, and thus does not contribute to the compression gain.

In Chapter 4 a technique was presented for using a fast, reflective microwave switch to block the input port after transmitting the excitation impulse into the cavity to mitigate the losses incurred at the input port. While this was effective for increasing the energy in the recorded IR, there are limitations in the amount of peak power that can be applied to the fast microwave switches before non-linear effects begin to degrade the output pulse. This leads us to consider, though, the possibility of *single-feed* TPRC techniques that would avoid the return loss effect at the input port of a 2-port cavity.

There have been single-feed TRPC techniques demonstrated previously as in [34] and [35] but these still fundamentally use 2-port cavities: one input/output feed (used for transmitting and receiving) and one or more apertures, Figure 5-2. The pulse compression process in this case is similar to that for the dual-feed cavities except the original excitation is transmitted from an external antenna a distance away from the cavity. This excitation enters the cavity through an aperture and the IR is received at the feed. Then, upon TR and retransmission, the reconstructed impulse is recorded back on the distant antenna. This technique is useful primarily for its ability

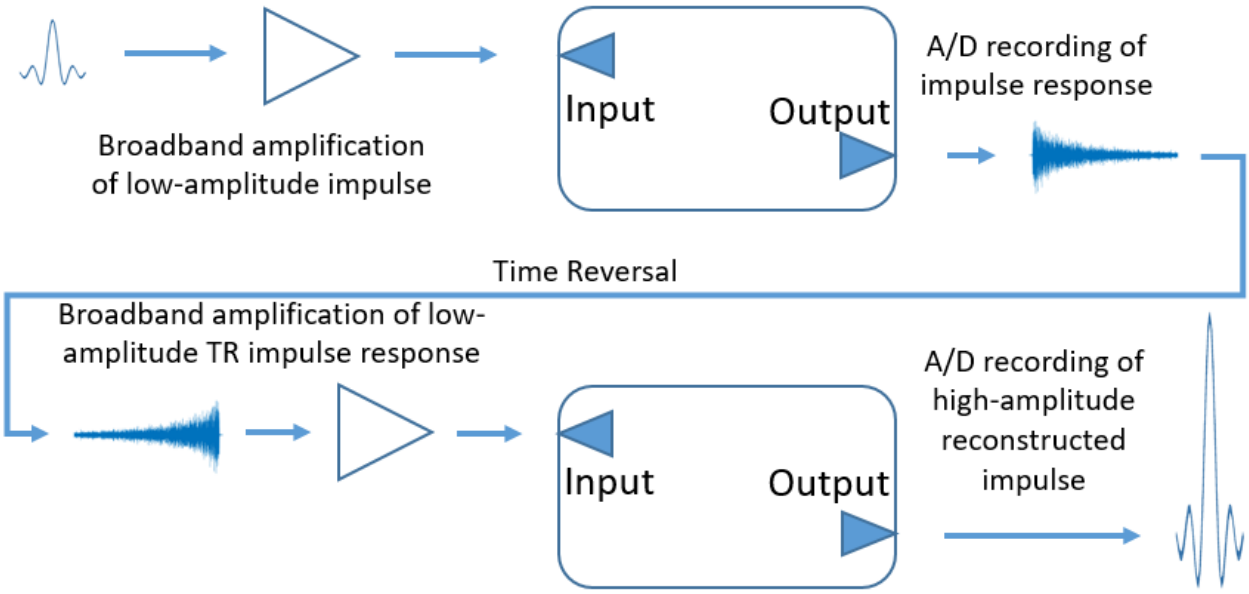

Figure 5-1. 2-port cavity TRPC process using a dual-feed cavity architecture.

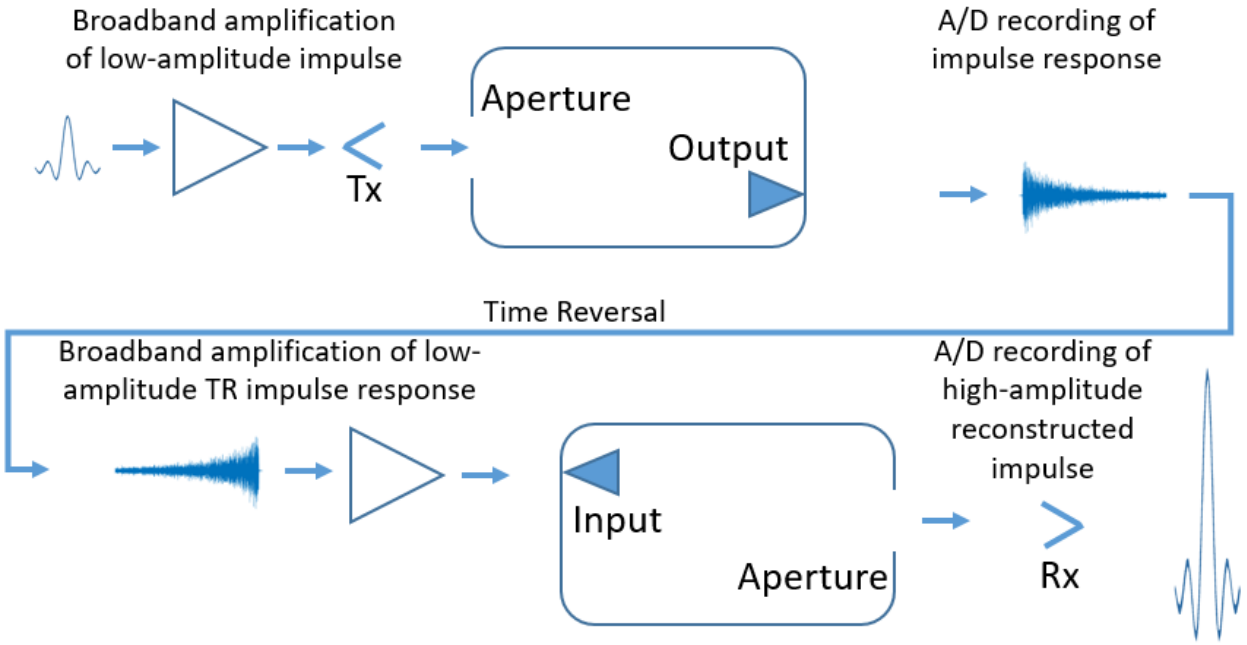

Figure 5-2. A 2-port cavity TRPC process using a single-feed and aperture architecture with and external antenna.

to focus energy spatially and temporally at a distance, but not for providing a higher-power signal to a transmit antenna through increased gain.

In this chapter a novel technique is presented for performing TRPC using a cavity with *a single port* and a *microwave circulator* attached to this port, Figure 5-3. This technique takes advantage of both an increase in the loaded quality factor due to the removal of the second port, as well as an increase in available power by using the same port as both input and output. The TRPC process is identical to the standard dual-feed process, except that the cavity itself has one port (one feed) and the attached circulator provides the two ports at the system level. Strictly speaking, the *system* still has two ports, but the cavity itself has only one port. Thus a distinction is made between the cavity ports and the entire TR system ports.

As discussed previously, other techniques to further increase compression gain have been demonstrated such as using a mode-stirrer to optimize the internal geometry of a cavity and/or moving/optimizing the position of the mode-stirrer within the cavity, [29], [47]. Additionally, methods for increasing the cavity quality factor by increasing the conductivity through the use of higher-conductivity materials or by cryogenic cooling have also been suggested [29], [47]. All of these techniques are as equally applicable to a 1-port cavity as they are to a 2-port cavity.

5.1 - Motivation for Single-Port Pulse Compression

In this section the relevant theory and modeling that motivate the use of a single-port (1-port) cavity for TRPC are reviewed. There are two relevant concepts to consider: 1) the existence of coherent reciprocal ray paths at the input port, and 2) the increase in the cavity loaded quality factor, Q_l, achieved by not having a second port.

5.1.1 - On the Potential for Increased Power by Using One Port for both Transmitting and Receiving

First, it was shown in [48], using a geometric optics derivation, that in a two-port (2-port) reverberant system the squared magnitude of the complex reflection coefficient is twice that of the squared magnitude of the complex transmission coefficient,

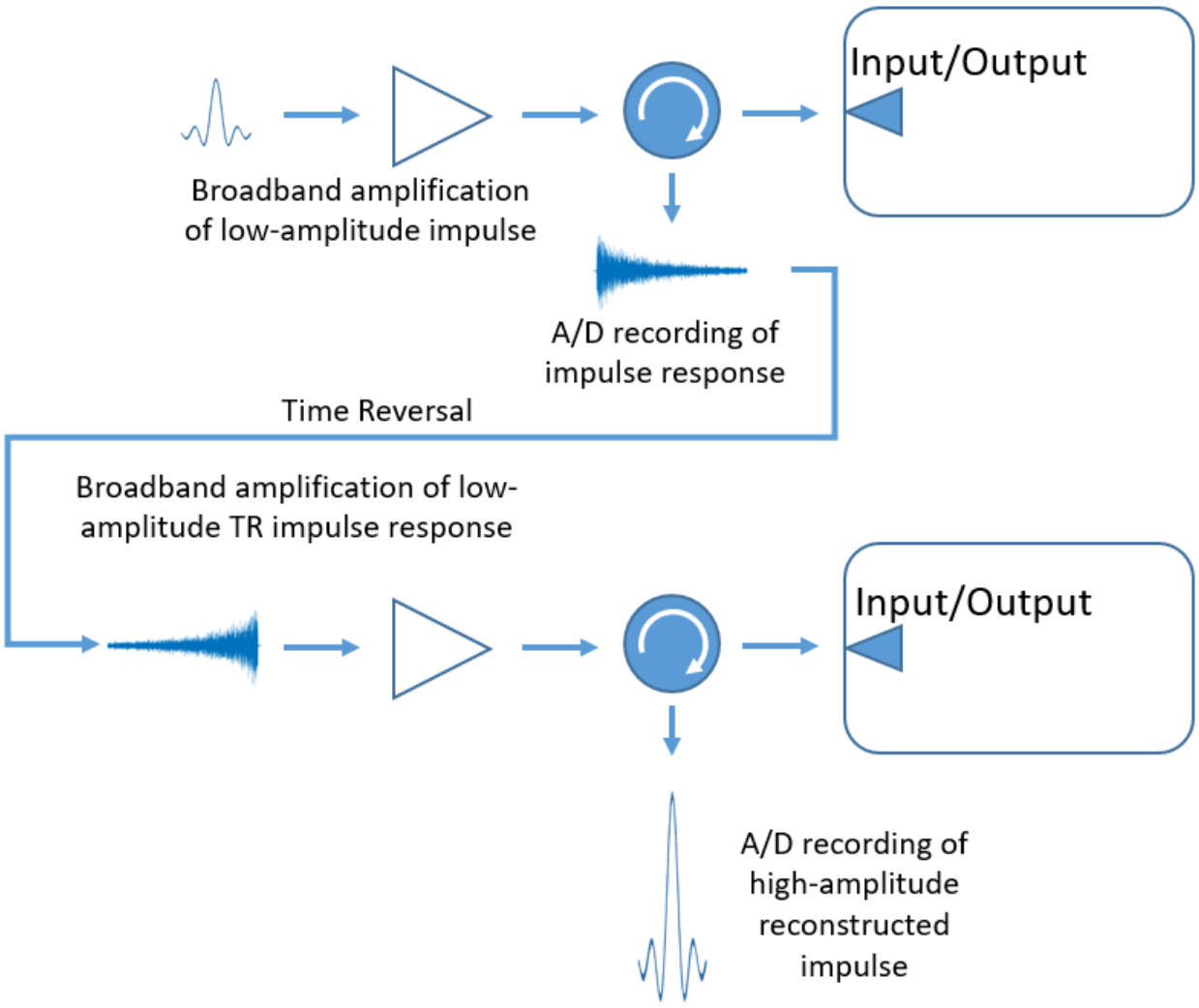

Figure 5-3. A 1-port TRPC process using a cavity with a single port and a circulator.

$$\langle |S_{11}|^2 \rangle = 2\langle |S_{21}|^2 \rangle. \tag{5.1}$$

where angle brackets denote an ensemble average. It is concluded that this doubling in returned power at the input is due to coherent addition of reciprocal rays from the energy backscattered in the cavity and returning to the input feed [48]. This is now a well-known finding from reverberation chamber theory, and is illustrated in Figure 5-4. This derivation was done without considering reflection due to impedance mismatch at the input, but nonetheless this phenomena suggests it may be more advantageous to use the input port for both transmitting the excitation waveform *and* receiving the impulse response. The second port would then *only* act as an

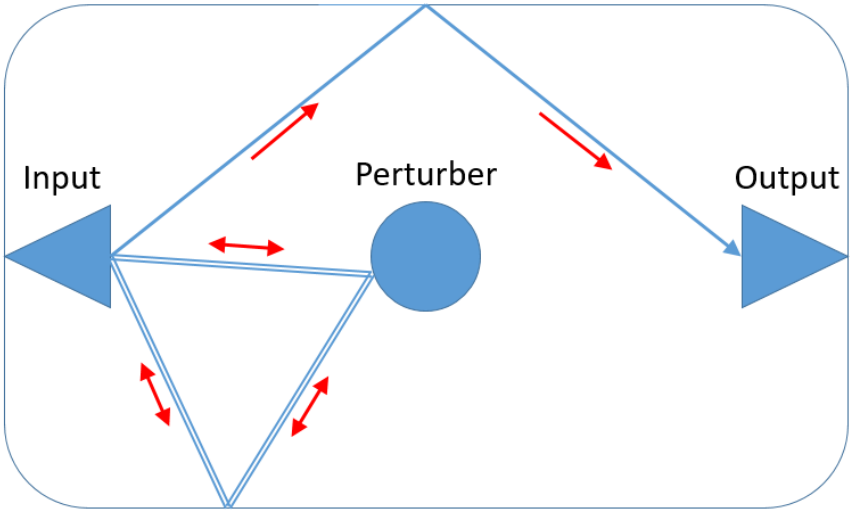

Figure 5-4. A dispersive, reverberant cavity with two ports. Due to identical transmit and receive locations, the coherent addition of a portion of the transmitted waves at port 1 leads to a doubling in normalized power. Adapted from [17].

absorptive port, and would thus be an unnecessary source of loss. One can conjecture from (5.1) that since there is twice as much power at the input port as is incident on the output port, then one should see some benefit in compression gain from using the only input port for performing TRPC.

5.1.2 - On the Increase in Loaded Quality Factor from Removing the Second Port

Next, in [49], a mathematical model for the impact of additional ports on the frequency dependent loaded quality factor, Q_l, is presented, and shown here as

$$\frac{1}{Q_l(f)} = \frac{M}{Q_p(f)} + \frac{1}{Q_u(f)}. \tag{5.2}$$

where, Q_p is a term describing the effect of the ports on Q_l and is given as

$$Q_p(f) = \frac{Q_p^0(f)}{1 - \eta_p^2(f)|\Gamma_L|^2}, \tag{5.3}$$

and M is the total number of ports in the cavity plus 1 due to the condition in (5.1). Thus, for example, $M = 2$ corresponds to a single-port cavity. Q_u is the unloaded quality factor of the cavity. In the numerator of (5.3), $Q_p^0(f) = \pi^2(V/\lambda^3)$ where V is the cavity volume and λ is the wavelength. In the denominator η_p is the radiation efficiency of the ports where it is assumed all feeds have the same radiation efficiency, and Γ_L describes the mismatch between the ports and the load.

The unloaded cavity quality factor, Q_u can be determined using several methods. For Q_u, including cavity volume, V, surface area, S, and conductivity, σ, is of interest; a good model for Q_u is found in [50] and gives

$$Q_c = \frac{3V}{2\delta S}. \tag{5.4}$$

where, for the cavity in this work, $V = 0.0115\ m^2$, and the skin depth $\delta = \sqrt{2/(2\pi f \mu_0 \sigma)}$ where $\mu_0 = 1.26 \times 10^{-6}$ H/m, $\sigma = 2.5 \times 107$ S/m (6061-T6 aluminum), and it is assumed there is no surface roughness. By using (5.3) and (5.4) in (5.2) Q_l can be calculated for a 1-port and 2-port cavity. It is assumed the feeds and loads are well-matched, and the ports are efficient, such that both η and Γ_L equal 1. Then, by setting $M = 2$ and $M = 3$, the frequency-dependent Q_l can be estimated for both a 1-port and 2-port cavity, respectively, as plotted in Figure 5-5(a). It can be seen that the loaded quality factor of the 1-port cavity is ~2600 larger than that of the 2-port cavity across the entire bandwidth of interest (6.5 GHz to 17 GHz). In Figure 5-5(b) each component of (5.2) is plotted for both 1-port ($M = 2$) and 2-port ($M = 3$) cavities to show how the factor related to the ports (M/Q_p) varies in relation to the inverse of the unloaded quality factor, ($1/Q_u$). It can be seen that the f^3 term in Q_p makes these contributions decay quickly with frequency, approaching zero. The frequency range of interest in this chapter is 6.5 GHz to 17 GHz. For this range the M/Q_p components intersect $1/Q_u$ at ~9 GHz and ~10.5 GHz for $M = 2$ and $M = 3$, respectively. The region in Figure 5-5(a) where the difference between the 1-port and 2-port Q_l is maximum corresponds to the region in Figure 5-5(b) after the M/Q_p plots intersect $1/Q_u$ at ~11.5 GHz. It should be noted that (5.2) and (5.4) form upper bounds for the quantities Q_l and Q_u, and that more empirical estimations of these values may better approximate a particular cavity [51]. Equation (5.2) and (5.4) have been used here for their ease of use and generality. It can be further

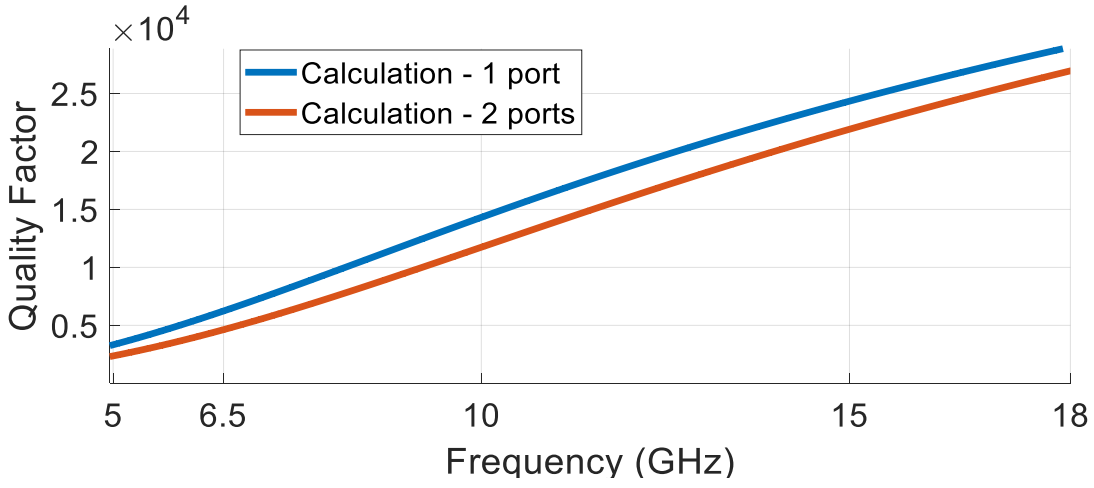

(a)

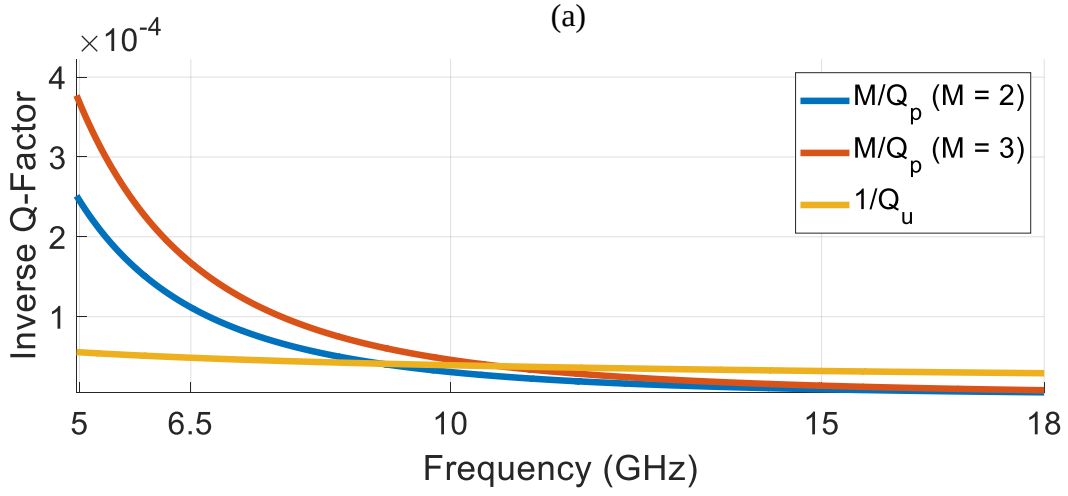

(b)

Figure 5-5. (a) Frequency dependent loaded quality factor, Q_l, from 5 GHz to 18 GHz for 1-port and 2-port cavities calculated using (6). (b) M/Q_p for 1-port and 2-port cavities plotted with $1/Q_u$ for (6).

conjectured that the *increase* in Q_l due to a *lower value* of M, should increase the compression gain even further. However, it is unclear how this increase in Q_l corresponds quantitatively to a change in the compression gain. For instance, a change in the orientation or position of a mode stirrer, can also increase or decrease the gain by up to ~2.5 dB [29], [47]. Similarly, a change in the orientation of the feeds can increase or decrease the signal-to-noise ratio (SNR), and potentially the gain [42]. This sensitivity to internal boundary conditions suggests a statistical approach is preferable for modeling compression gain.

5.2 - Compression Gain Modeling

5.2.1 - Cavity Transfer Function Modeling using the Random Coupling Model

To examine how the increased Q_l achieved by going from a 2-port to a 1-port cavity affects the compression gain, a novel application of the random coupling model (RCM) is used to develop *transfer functions* for both 1-port and 2-port cavities. A comprehensive overview of standard RCM theory and applications can be found in [39], [52], and at [53]. The RCM has heretofore been used to predict the statistics of induced voltages on ports in reverberant cavities. It is of interest to apply the RCM for generating physics-based transfer functions, based on the radiation impedance of the cavity feeds, to model the increase or decrease in compression gain due to different cavity realizations in 1-port and 2-port cavities. To do this the cavity transfer function is statistically modeled using the RCM formulation for the 1-port impedance matrix [54], Z, such that

$$Z(k) = -\frac{j}{\pi}\sum_{n}\frac{\Delta k^2 R_{11}^{rad}(k_n) w_n^2}{k^2\left(1-\frac{j}{Q_u}\right)-k_n^2} \tag{5.5}$$

where k is the wavenumber, k_n are the cavity eigenmodes, and $w_n = X_1$ such that X_1 is a vector of L independent and identically distributed (iid) elements, each with a standard normal distribution, $N(0,1)$. L is the approximate number of cavity modes in the frequency band of interest. The unloaded, frequency dependent cavity quality factor, Q_u, is determined using (5.4). $R_{11}^{rad}(k_n)$ is the radiation resistance of the simulated port, and thus specific to this system. R_{11}^{rad} is the real-part of the radiation impedance Z_{11}^{rad}, thus Z_{11}^{rad} must be found.

There are two methods for determining Z_{11}^{rad}: direct simulation with a full-wave electromagnetic (EM) solver with three of the four cavity walls removed and replaced with a perfectly matched layer (PML); or a technique known as the time-gating method (TGM) [55]. Both techniques for the proposed system are compared.

For the first method the full-wave EM solver, CST, is used to simulate the cavity with all but the input port wall and the perturber removed (Figure 5-6), thus directly obtaining S_{11}^{rad} from which Z_{11}^{rad} is obtained using the bilinear transformation

$$Z_{11}^{rad} = \frac{\left(1 + S_{11}^{rad}\right)}{\left(1 - S_{11}^{rad}\right)} Z_{\mathbf{0}} \tag{5.6}$$

and it is assumed Z_0 *is* 50 Ω.

For the second method the following steps are used:

1) Obtain the complex reflection coefficient, S_{11}, of the input feed, connected to the cavity, through full-wave simulation (this can be done in measurement as well), Figure 5-7(a).

2) Take the inverse Fourier transform of S_{11}. The initial time period containing prompt reflections from the feed/cavity mismatch and coupled energy from short orbits is noted as the gating time, t_{gate}, Figure 5-7(b). Short orbits here are short ray paths not modeled by random matrix theory, and are those rays that have entered the cavity and quickly returned after only a few reflections (such as those reflected by the perturber) [56, 57].

3) This time-gated portion is then Fourier-transformed and the radiation impedance, $Z_{11}^{rad} = R_{11}^{rad} + jX_{11}^{rad}$, is obtained using (5.6). Figure 5-8 shows both Z_{11}^{rad} and the cavity impedance Z_{11}, which is also obtained using (5.6), but using S_{11} in instead of S_{11}^{rad}.

The real part of Z_{11}^{rad} is the radiation resistance R_{11}^{rad} and the imaginary part is the radiation reactance, X_{11}^{rad}; both are plotted in Figure 5-9. There is good agreement between the two methods, but by definition the PML solution is the exact representation of the radiation impedance, so the results of the PML method are used for the cavity impedance modeling. However, it is important to note that the time-gating technique is much simpler to employ experimentally.

Once R_{11}^{rad} is determined all the components to calculate (5.5) are known. Next, a Monte Carlo simulation of (5.5) is performed with both k_n and w_n as random variables to find a range of different instances of Z_{11}. These different instances correspond to different internal cavity geometries but with the same volume, surface area, and conductivity. Alternatively, each instance can correspond to a different placement of the cavity feeds with respect to each other. The Monte Carlo simulation was performed for 200 iterations.

The same modeling was carried out for the 2-port cavity as well so results can be compared with those of the 1-port cavity. The only difference for the two port cavity simulation is that the radiation impedance is now a 2 x 2 matrix [58] and (5.5) is now represented with a matrix formulation such that

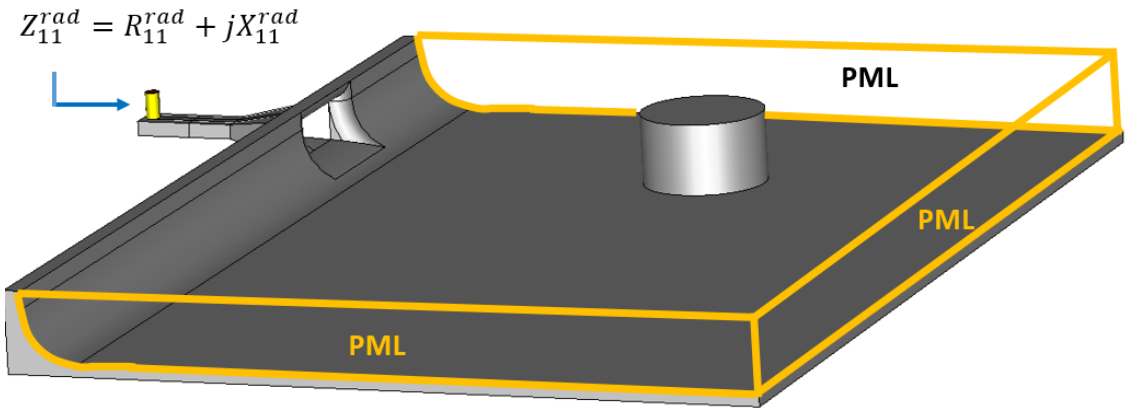

Figure 5-6. Z_{11}^{rad} of cavity directly simulated in CST full-wave solver. Three walls of the cavity have been removed and replaced with a PML boundary. The lid remains in the simulation, and is only removed here to show detail.

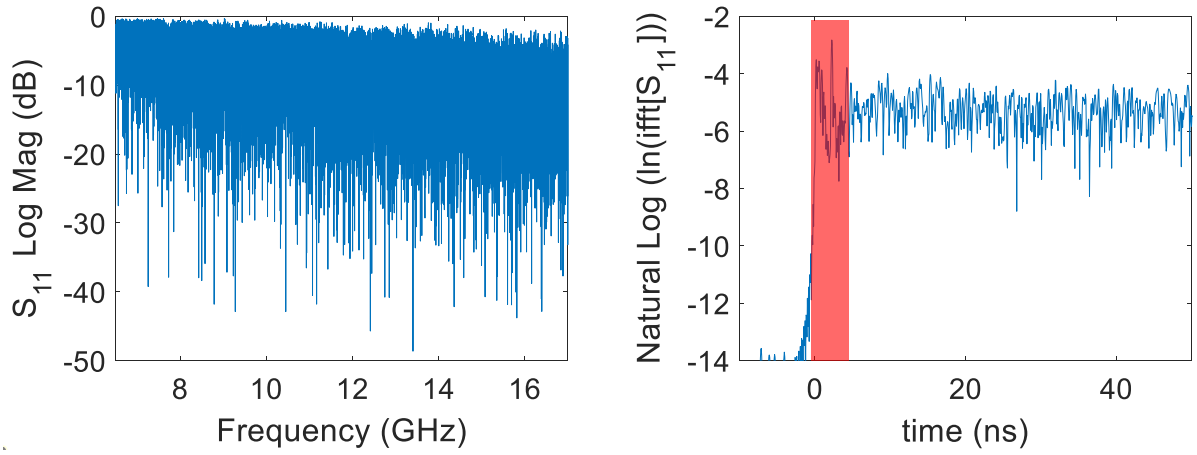

(a) (b)

Figure 5-7. a) S_{11} of cavity simulated in CST. (b) Inverse Fourier transform (time-domain response of cavity) used to find the time-gating length, t_{gate} for use in finding $\boldsymbol{R}^{rad}$ (Gating time (box) is determined to be 5 ns.)

$$Z(k) = -\frac{j}{\pi}\sum_{n}\frac{\Delta k^2 \boldsymbol{R}^{rad\frac{1}{2}}(k_n) w_n w_n^T \boldsymbol{R}^{rad\frac{1}{2}}(k_n)}{k^2\left(1-\frac{j}{Q_u}\right)-k_n^2}. \tag{5.7}$$

Here $w_n = [X_1;\ X_2]$ such that X_1 and X_2 are random vectors of L iid, standard normally distributed elements, and the bold $\boldsymbol{R}^{rad}$ is the matrix radiation resistance of the simulated port, and thus specific to this system. $\boldsymbol{R}^{rad}$ is a function of k_n, and is determined by taking the real-part of the

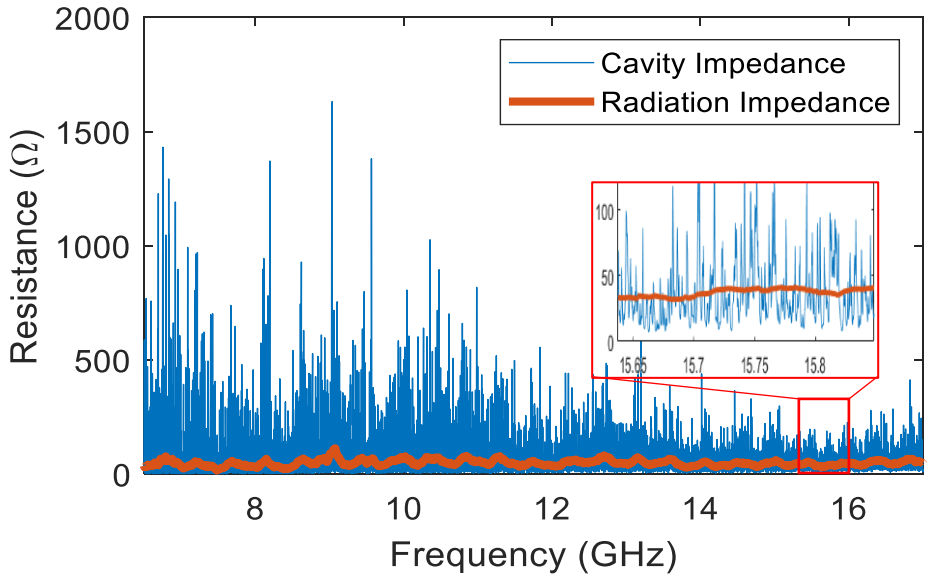

Figure 5-8. Z_{11} of cavity simulated in CST and Z^{rad} as determined using the TGM.

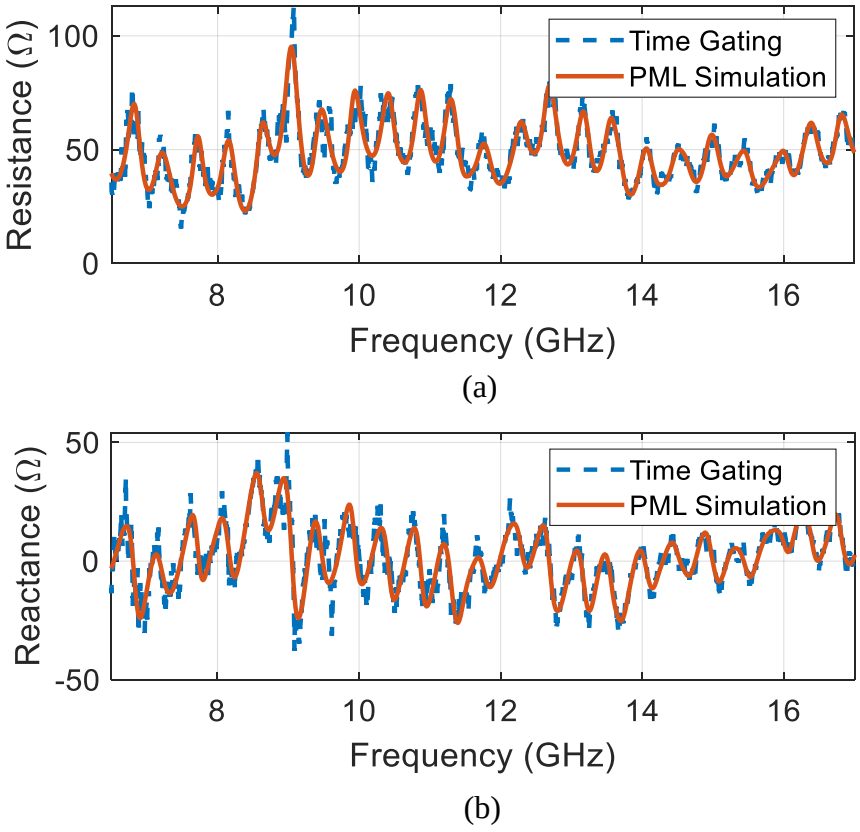

Figure 5-9. (a) Radiation resistance, R_{11}^{rad} and (b) radiation reactance, X_{11}^{rad}, determined by both the time gating and the PML simulation methods.

radiation impedance $\boldsymbol{Z}^{rad} = \boldsymbol{R}^{rad} + j\boldsymbol{X}^{rad}$ where $\boldsymbol{X}^{rad}$ is the radiation reactance. Also, recognizing that the ports are identical the substitution $R_{11}^{rad} = R_{22}^{rad}$ can be made such that

$$\boldsymbol{R}^{rad} = \begin{bmatrix} R_{11}^{rad} & 0 \\ 0 & R_{11}^{rad} \end{bmatrix}. \tag{5.8}$$

The off-diagonal elements are set to zero with the assumption that there is no direct coupling between the two ports. This is justified by noting that often the direct path between the two ports is blocked or minimized such that the energy available to fill the cavity is maximized. This is important because the energy available to the cavity is what is compressed to realize gain. Therefore, minimizing the direct path maximizes the pulse compression gain of the cavity. However, in some cases there may be unavoidable direct paths between the two ports, in which case the off-diagonal elements of the radiation impedance in the model cannot be neglected.

Before presenting the numerical results for compression gain calculated using the RCM-generated transfer functions, it is noted that a cavity transfer function was modeled in [42] and used to compute the statistics of the SNR between the reconstructed impulse and the time-sidelobes (noise) of the same signal. This is a short step away from computing gain. The primary difference between the RCM transfer function formulation and that in [42] is that, in [42], the cavity eigenmodes are assumed to be equally distributed across the system spectrum and the quality factor is not an explicit function of the surface area or conductivity. The RCM formulation presented here is an explicit function of the radiation impedance and the eigenmodes modeled after the eigenvalues of random matrices satisfying the Gaussian Orthogonal Ensemble (GOE) condition. Thus, the technique presented here is applicable to looking at more specific cavities (though without need for specifying the internal geometry). These transfer function models will now be used to model compression gain for both 1-port and 2-port systems.

5.2.2 - Modeling Compression Gain

The entire TRPC process can be described succinctly using (5.9) such that the reconstructed impulse, $y(t)$, is the autocorrelated impulse response of the cavity, ψ_{hh},

$$y(t) = h(t) * ah(-t) = a\int_0^T h(\tau)h(\tau - t)d\tau = \psi_{hh} \tag{5.9}$$

where $h(t)$ is the cavity impulse response, and a is an amplification factor. The description in (5.9) is a time-domain representation of the TRPC process. For the modeling described here, this process is performed in the frequency domain. Using the Fourier transform, $h(t)$ becomes $\mathcal{F}\{h(t)\} = H(\omega)$, and $h(-t)$ becomes $\mathcal{F}\{h(-t)\} = H^*(\omega)$, which is the complex conjugate of the transfer function, $H(\omega)$. Thus (5.9) becomes

$$Y(\omega) = H(\omega)H^*(\omega) = |H(\omega)|e^{-j\Theta(\omega)}|H(\omega)|e^{j\Theta(\omega)} = |H(\omega)|^2 \tag{5.10}$$

Using the system-specific transfer function models developed in the previous section, Monte Carlo simulations are performed to generate both the 1-port and 2-port cavity transfer functions. To each of these transfer functions the spectrum of the excitation shown in Figure 5-10 is applied. Then, the result is inverse-Fourier-transformed, which gives the IR, $h(t)$, for that particular cavity realization (i.e., instance of Z_{11}). This IR is then time-reversed, normalized, Fourier transformed, and reapplied to the same transfer function. The result is the spectrum of the reconstructed impulse. This is again inverse-Fourier transformed to obtain the time-domain representation of the reconstructed impulse, $y(t)$. The compression gain may then be computed.

Here, the same procedure is followed, and the same notation is used, for calculating compression gain as in [47] and [29], such that compression gain for regular TR is determined by taking the ratio of the peak of the output waveform to the peak of the input waveform as

$$\mathrm{G}_{TR} = 20\log_{10}\left[\frac{|y(t)|_{max}}{|ah(-t)/\max[h(-t)]|_{max}}\right] \tag{5.11}$$

Here the normalization of the time-reversed impulse response is retained in the denominator, and a is an amplification factor. This formulation is heuristic for the measured results as it assumes a

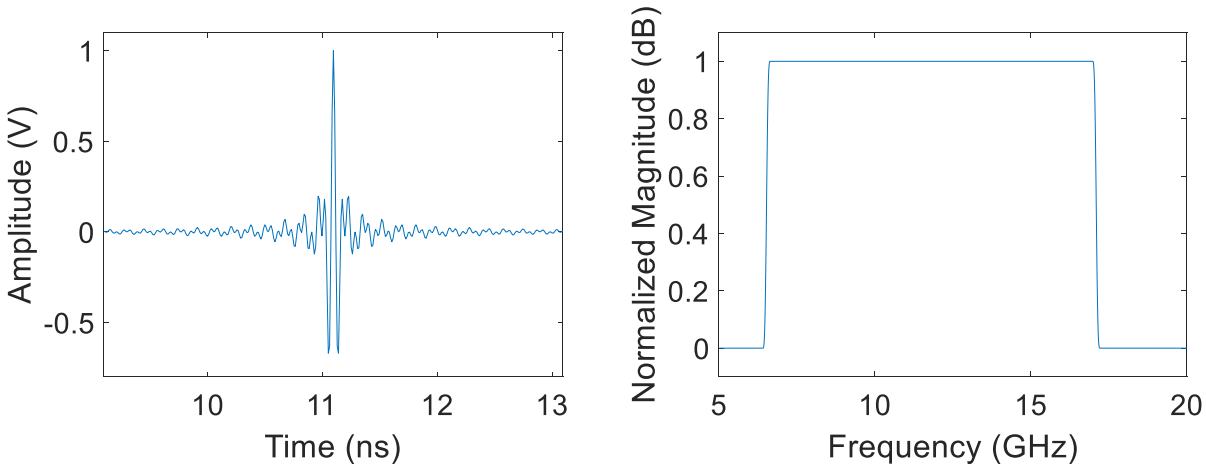

(a) (b)

Figure 5-10. (a) Excitation signal and (b) it's spectrum for both the compression gain modeling in Section 5.2.2 and the simulations in this section.

flat amplification response. The compression gain for OBTR is similarly computed as

$$G_{OBTR} = 20\log_{10}\left[\frac{|y(t)|_{max}}{|a\text{sign}\{h(-t)/\max[h(-t)]\}|_{max}}\right] \tag{5.12}$$

where

$$\text{sign}[h(-t)] = \begin{cases} +1 \ for\ h(-t) > 0 \\ -1\ for\ h(-t) < 0 \end{cases}. \tag{5.13}$$

The digitization of the IR using OBTR, as in (5.13) adds additional energy to the IR, while sufficiently preserving the phase such that the pulse reconstruction still occurs, but with significantly higher gain. In Figure 5-11 results for both the 1-port and 2-port cavities are plotted for regular and OBTR for 200 different cavity realizations, and the statistics are given in Table 5-1. It can be seen that there is clearly an increase in compression gain for the 1-port cavity compared to the 2-port cavity for both regular TR and OBTR. In fact, for regular TR, the mean compression gain (20.4 dB) is 3.7 dB higher than the mean compression gain of the 2-port cavity (16.3 dB). For OBTR, the mean compression gain is 4.4 dB higher for the 1-port case compared

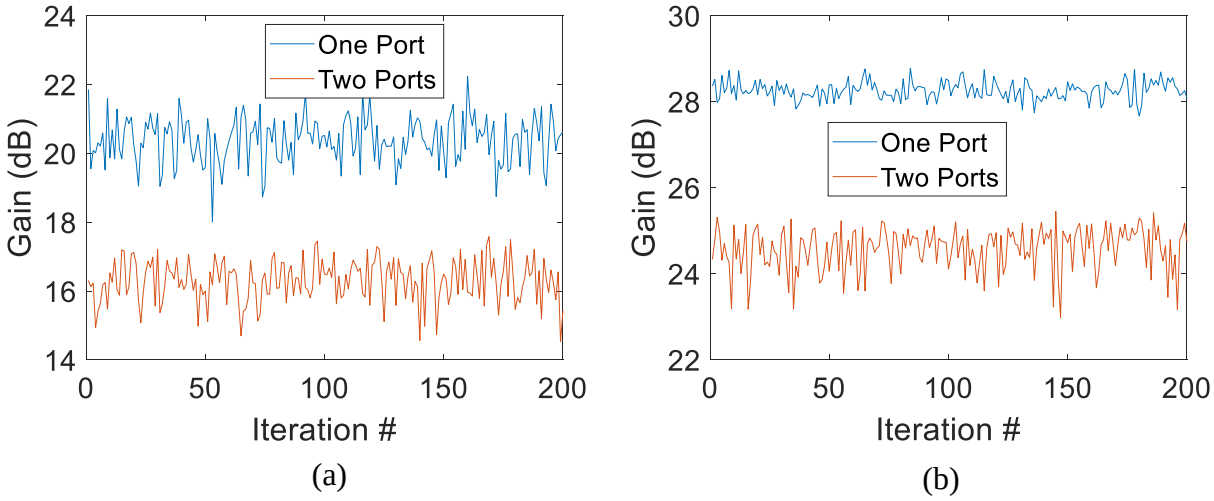

Figure 5-11. Compression gain over 200 realizations for (a) regular TR for both 1-port and 2-port cavities, and for (b) OBTR for both 1-port and 2-port cavities. For all simulations the impulse response length was 1600 ns.

Table 5-1. Statistics Of Compression Gain Modeling For Regular TR And OBTR

CASE	*Min Gain (dB)*	*Max Gain (dB)*	*Mean Gain (dB)*	*Variance (dB)*
RTR: 1-port	18.0	22.5	20.4	0.46
RTR: 2-port	14.5	17.6	16.3	0.38
OBTR: 1-port	27.7	28.8	28.3	0.05
OBTR: 2-port	23.0	25.4	24.6	0.25

to the 2-port case. In order to obtain this increase, though, there is one additional signal processing step that must be applied in the 1-port pulse compression process. After generating the impulse response, the effects from the prompt reflections and short orbit (short path) returns (noted in Figure 5-7) must be removed by truncating the beginning of signal for the length of time these reflections occur *plus* the initial time that it takes for the sinc function *peak* to enter the cavity.

In the present case the sinc pulse peak enters the cavity about 11.2 ns after the beginning of the excitation, Figure 5-10(a), and the prompt reflections and short orbit returns occur for about 5 ns, totaling ~16 ns. The prompt reflections and short orbit returns will be referred to collectively as early-time reflections.

The reason these early-time reflections cause decreased compression gain is their amplitude is much higher than the actual decaying response associated with the cavity time-

constant, as seen in Figure 5-12. It is clear by inspection that there is far more energy in the normalized 2-port impulse response than in the 1-port response; this leads to decreased compression gain in the 1-port case without the truncation step. This is not the case for the 2-port cavity because, since the impulse response is received on the second port, early-time reflections do not impact the performance.

For *OBTR* with a 1-port cavity this is not as much of an issue since the rest of the signal has energy added due to the one-bit process, though even here there can be some benefit from truncation since the early-time reflections do exist. In Figure 5-13 the compression gain is plotted for both the 1-port and 2-port cavities vs. the length of time the initial part of the impulse response is truncated (for truncation, values are set to zero in processing). There is no change in compression gain for the first ~11.2 ns, which is the time between the start of the excitation and the peak of the excitation. After that, the gain increases rapidly (within 5 ns) such that while previously the 1-port cavity produced 9 dB less gain vs. than the 2-port cavity, it now produces almost 5 dB more. This truncation step is a critical step in the 1-port port pulse compression process.

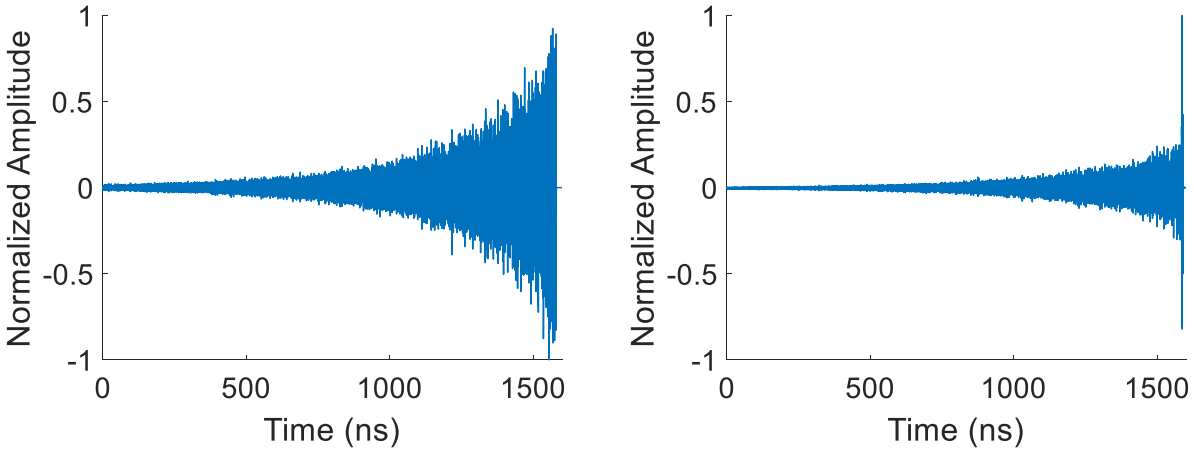

(a) (b)

Figure 5-12. Un-truncated, time-reversed impulse responses from (a) the 2-port cavity and (b) the 1-port cavity. The early-time reflections can clearly be seen in the 1-port impulse response while they are absent in the 2-port impulse response.

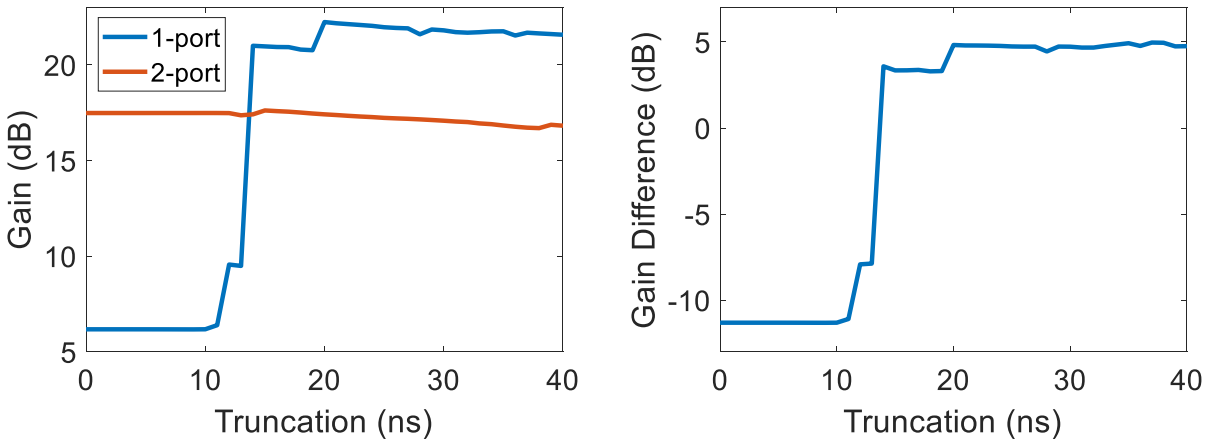

(a) (b)

Figure 5-13. (a) Compression gain for 1-port and 2-port cavities after truncating the impulse response to remove the initial prompt reflections in the 1-port response. (b) The difference in gain showing that in fact, 1-port pulse compression is superior even for regular time reversal as long as the waveform has the prompt reflection removed. For all simulations the impulse response length was 1600 ns.

5.3 - Compression Gain Simulations For 1-Port And 2-Port Cavities

The modeling results in the previous section show a ~4 dB increase in compression gain by using a 1-port cavity instead of a 2-port cavity. This model makes use of the system specific radiation impedance of the cavity, but requires no other information about the internal geometry other than the conductivity, volume, and surface area. Now it will be shown how these results apply to the actual cavity described in this dissertation, a *specific* instance of these modeled results.

To demonstrate 1-port TRPC one of the ports is removed from a 2-port cavity, and replaced with an aluminum plate, as shown in Figure 5-14. The cavity itself is identical to the first cavity used in [47] (i.e., no mode stirrer) minus the second port. The inner cavity dimensions are 65 cm x 45 cm x 4 cm, and the inner volume is 11,151 cm^3. The volume includes the cylindrical perturber, which has a height of 4 cm and a radius of 6.98 cm. Then, using the full-wave EM software suite, CST, the scattering parameters of both the 1-port and 2-port cavities from 6.5 GHz to 17 GHz are

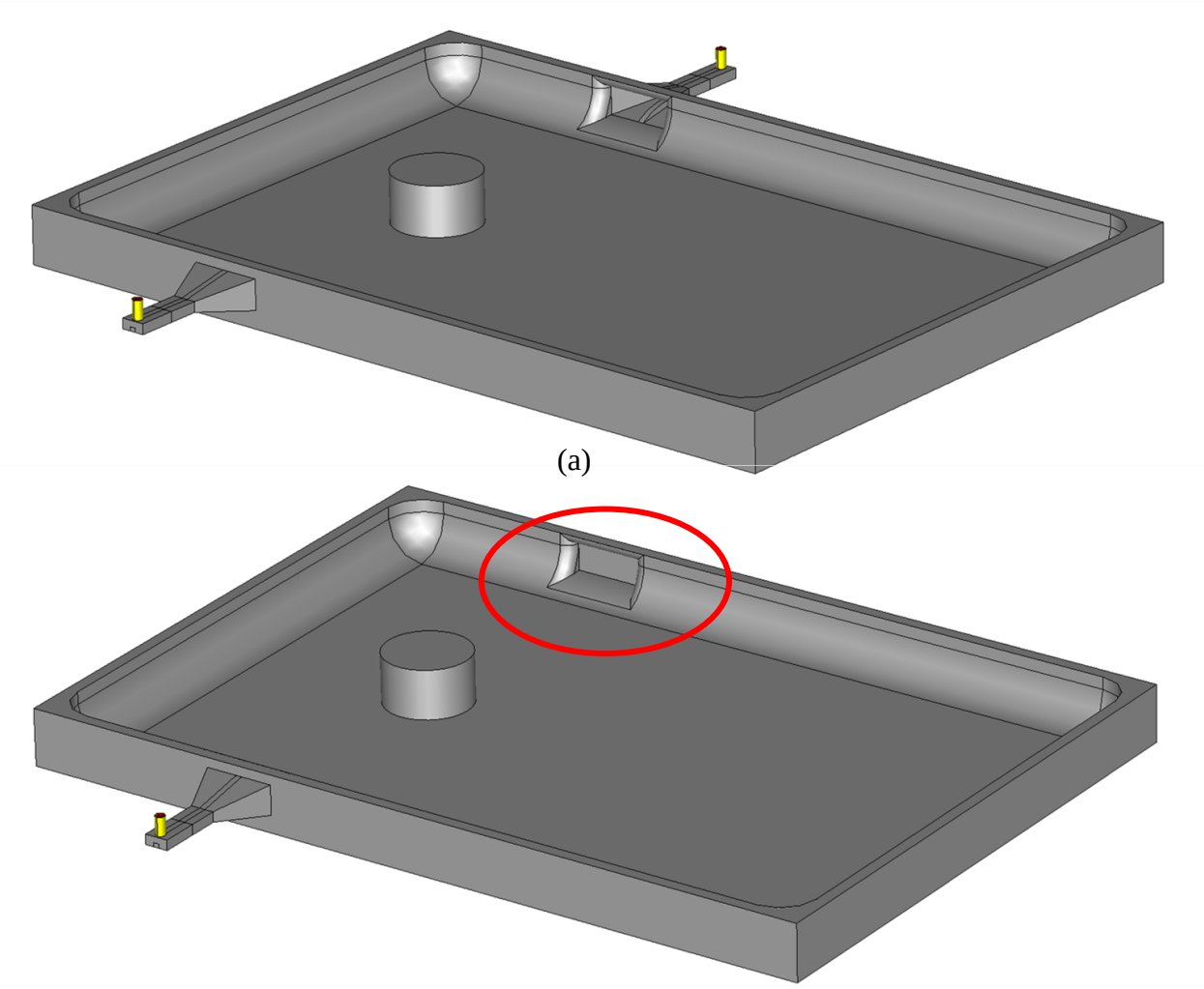

Figure 5-14. (a) CST model of 2-port cavity with perturber and (b) 1-port cavity. This 1-port cavity is identical to the 2-port except that port has been replaced by a blank plate (highlighted in red circle).

obtained. This bandwidth is slightly reduced from the 5 GHz to 18 GHz used in [47] due to the bandwidth limitations of the available WRD650 circulator. The four different TRPC operations from Table 5-1 were performed using the two sets of CST-simulated 1-port and 2-port scatttering parameters: regular TR for a 2-port cavity; regular TR for a 1-port cavity; OBTR for a 2-port cavity; OBTR for a 1-port cavity. Assuming a 50 Ohm system, S_{21} was used as the transfer function of the 2-port cavity. The scenario is depicted in Figure 5-15(a). For the 1-port cavity S_{11} was used as it contains both the reflected signal due to port/cavity mismatch as well as that which entered the cavity and returned to the port. This is equivalent to using an ideal circulator, i.e., one that maintains constant spectrum amplitude across the entire bandwidth from 6.5 GHz to 17 GHz,

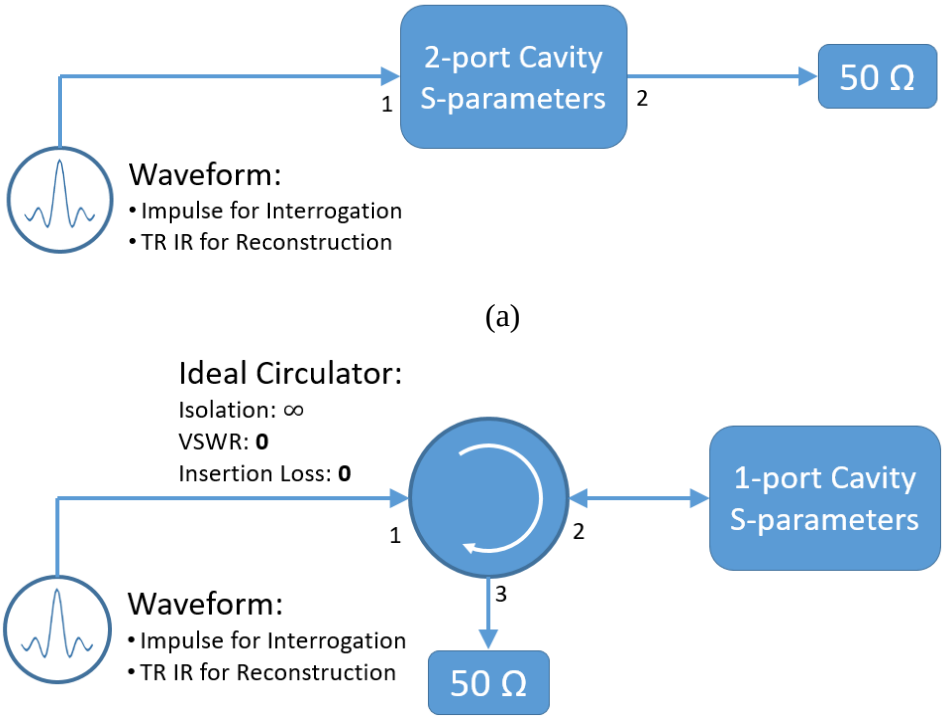

Figure 5-15. (a) Simulation schematics of 2-port, and (b) 1-port cavity as simulated using S-parameters determined in CST full-wave simulation. In both (a) and (b) the 50 Ohm load is the equivalent waveform recording point.

as well as infinite isolation and no insertion loss, Figure 5-15(b). The excitation waveform is described by a $\mathrm{sinc}(t)$ function, with a flat spectrum from

6.5 GHz to 17 GHz, and is the same as that applied to the transfer function in the RCM modeling, Figure 5-10(a). The same methods of using S_{21} and S_{11} as transfer functions for the 2-port and 1-port TRPC, respectively, was also used. Following the author's previous work in [47] the compression gain was calculated for impulse responses recorded in lengths of 400 ns to 1600 ns in 200 ns increments. In a low-loss cavity the compression gain is well-described by the time-bandwidth product, such that either an increase in bandwidth or an increase in the recorded impulse response length will lead to increased compression gain. In practice the compression gain will be much less than the time-bandwidth product, due to significant cavity and port losses as well as the dynamic range of the measurement system or simulation platform.

The compression gain results for regular TR and OBTR are given in Table 5-2 and Table 5-3. For regular TR an average 2.7 dB increase in compression gain is seen when using the 1-port cavity vs. the 2-port cavity, and for OBTR the average difference is 2.5 dB. The 1-port TRPC simulations are performed using the configuration depicted in Figure 5-15(b) corresponding to an ideal circulator, and providing a good analogue to the ideal conditions implicitly assumed for the modeling in section 5.2, but in a real-world implementation the circulator will not be ideal. The isolation will not be infinite, and there will be frequency dependent attenuation (insertion loss) across the spectrum.

To investigate how circulator isolation affects the compression gain, a circuit co-simulation technique was used such that the complex scattering parameters of each type of cavity (1-port and 2-port) obtained through simulation in CST, were then ported to a Keysight ADS circuit simulator. This method is used because the ADS circulator model allows the direct parameterization of isolation. Isolation was varied from 10 dB to 60 dB in 10 dB increments, and computed the compression gain for both regular and OBTR for a 1600 ns impulse response. The results are shown in Table 5-4. A concurrent increase in compression gain was seen with increasing isolation up to about 30 dB of isolation at which point the compression gain saturates at 19.0 dB for regular TR and 28.8 dB for OBTR. For comparison, the circulator used in the measurements (section 5.4) has an average isolation of about 17 dB.

Using the same circuit co-simulator method, the TRPC simulations were also performed using the measured 3-port scattering parameters from the real circulator as measured on a Keysight PNA-X N5247B 4-port network analyzer, Figure 5-16, rather than using a Keysight ADS-defined circulator model. The circulator is a custom-built WRD650 waveguide circulator, whose 3-port S-parameters are imported into the ADS circuit model (schematic shown in Figure 5-17). The results of this 1-port investigation are given in Table 5-5. Most notably, the use of the actual circulator S-parameters in simulation produced compression gains that are ~2 dB lower than the ideal circulator for both regular TR and OBTR. This is to be expected and brings the simulations more in line with the measured results.

Table 5-2. Compression Gain Comparison: 2-Port Vs. 1-Port Cavity: Regular Time-Reversal

Impulse Response Length (ns)	*PC GAIN (DB): 1-port*	*PC GAIN (DB): 2-port*	*Diff (dB)*
400	17.3	16.4	0.9
600	18.1	16.8	1.3
800	18.4	17.1	1.3
1000	18.5	17.1	1.4
1200	18.5	17.2	1.3
1400	18.5	17.2	1.3
1600	18.5	17.2	1.3

Table 5-3. Compression Gain Comparison: 2-Port Vs. 1-Port Cavity: One-Bit Time-Reversal

Impulse Response Length (ns)	*PC GAIN (DB): 1-port*	*PC GAIN (DB): 2-port*	*Diff (dB)*
400	25.3	24.5	0.8
600	27.1	25.7	1.4
800	27.8	26.6	1.2
1000	28.4	27.1	1.3
1200	28.6	27.5	1.1
1400	28.8	27.9	0.9
1600	28.8	27.9	0.9

Table 5-4. Compression Gain Vs. Circulator Isolation

Isolation (dB)	*PC Gain (dB): Reg. TR*	*PC Gain (dB): 1-Bit TR*	*Diff (dB)*
10	13.1	23.3	10.2
20	16.8	26.6	9.9
30	18.0	27.8	9.9
40	18.3	28.2	9.8
50	18.5	28.3	9.8
60	18.5	28.3	9.8

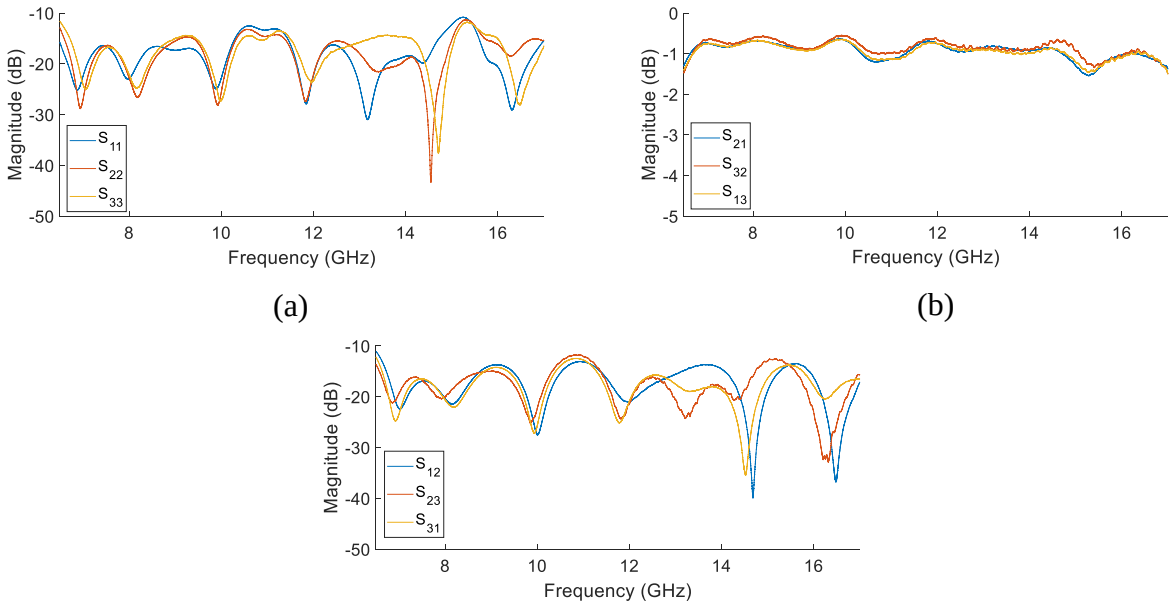

Figure 5-16. Measured WRD650 circulator 3-port S-parameters from 6.5 GHz to 17.5 GHz (a) reflection coefficients (b) transmission coefficients, and (c) isolation. Average insertion loss: S21 = 0.93 dB, S32 = 0.85 dB. Average isolation: S12 = 17.1 dB, S31 = 17.5 dB.

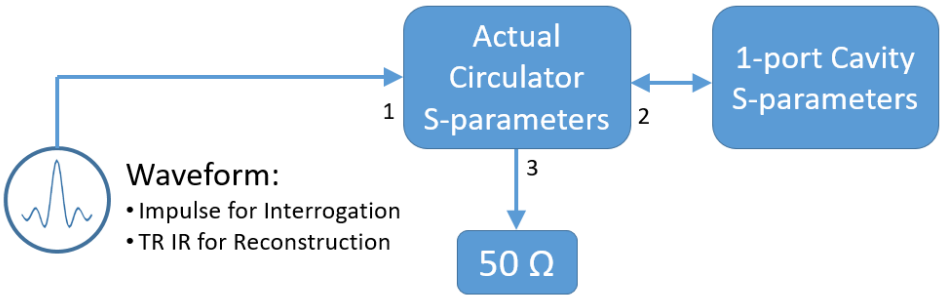

Figure 5-17. Circuit diagram for Keysight ADS simulation using 3-port s-parameters for the circulator rather the ADS-defined circulator.

Table 5-5. Compression Gain Using Measured 3-Port S-Params From Real Circulator

Impulse Response Length (ns)	*PC GAIN (DB): Reg. TR*	*PC GAIN (DB): 1-Bit TR*	*Diff (dB)*
400	15.9	22.8	6.9
600	16.7	24.6	7.9
800	17	25.6	8.6
1000	17.1	26.1	9
1200	17.2	26.4	9.2
1400	17.2	26.5	9.3
1600	17.2	26.6	9.4

5.4 - Pulse Compression Measurements

TRPC was performed for both 1-port and 2-port cavities using what are here called ‘full time-domain’ measurements, which is the most common technique found in the literature, [29], [30], [31], and in the author’s previous work [47]. As shown in Figure 5-18, the excitation impulse is first transmitted from an arbitrary waveform generator (AWG) through a wideband amplifier into the cavity and the impulse response is recorded on a sampling oscilloscope (Tektronix

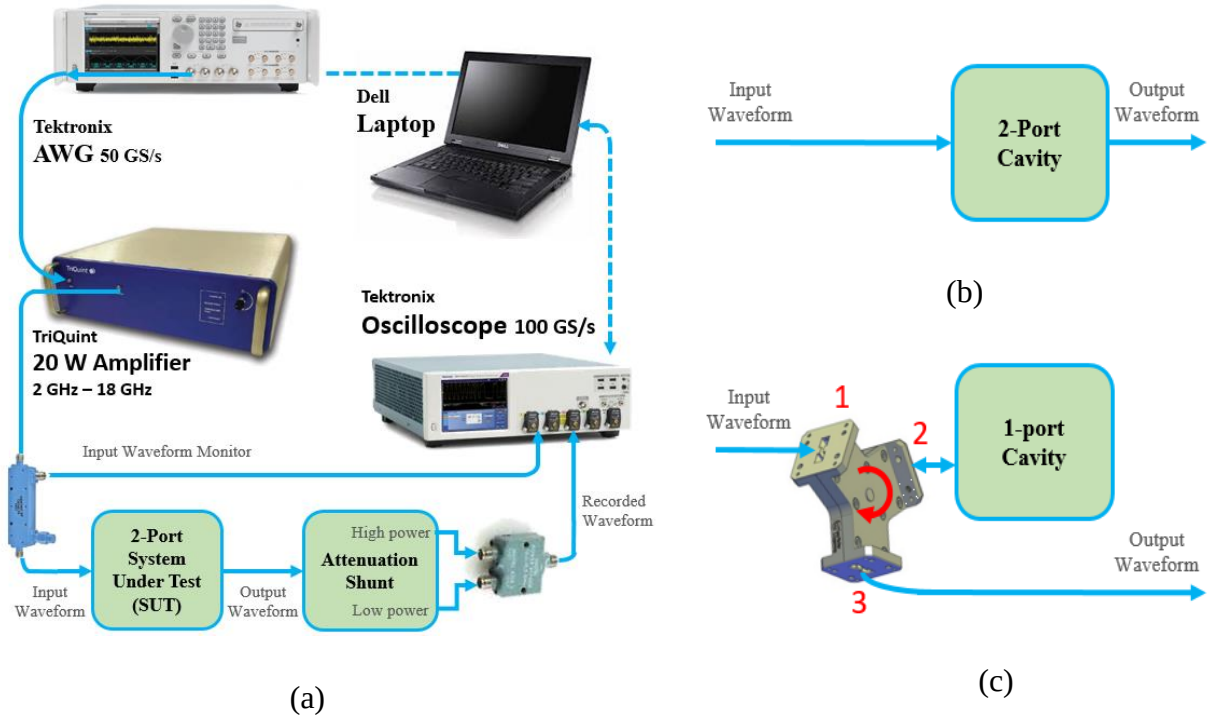

Figure 5-18. (a) Experimental setup for both 1-port and 2-port measurements. The Attenuation Shunt switches between a low insertion loss (IL) and high IL attenuator to protect the oscilloscope from the high peak power of the reconstructed impulse. (b) System under test (SUT) for 2-port TRPC measurements. (c) SUT for 1-port TRPC measurements.

DPO73304SX) with 100 GS/s sampling rate. This waveform is then time-reversed and retransmitted into the cavity using the AWG and the wideband amplifier, and the reconstructed impulse is recorded on the oscilloscope.

The 2-port cavity and setup are similar to that in [47], but a slightly reduced bandwidth (6.5 GHz to 17 GHz) is used as described earlier in section 5.3. Other differences include the use of a 20 W wideband amplifier (CAP Wireless RM022020, 2 GHz – 18 GHz) instead of the 100 W wideband amplifier (Qorvo QPR1001, 2 GHz to 18 GHz), and a 50 GS/s AWG (Tektronix AWG70001A) instead of 92 GS/s AWG (Keysight M8196A), Figure 5-18(a). The lower power amplifier was used because the higher power amplifier used in [47] was not available at the time of these measurements. A photograph of the fabricated 1-port cavity with the circulator attached is shown in Figure 5-19 to provide a better picture of how the circulator is attached to the cavity. As with the simulations in section 5.3, the compression gain was measured for impulse responses recorded in lengths of 400 ns to 1600 ns in 200 ns increments. The results are shown in Table 5-6 and Table 5-7 for regular TR and OBTR, respectively. For OBTR, similar behavior to the simulated results in Table 5-3 is seen such that the difference in compression gain (1-port vs. 2-

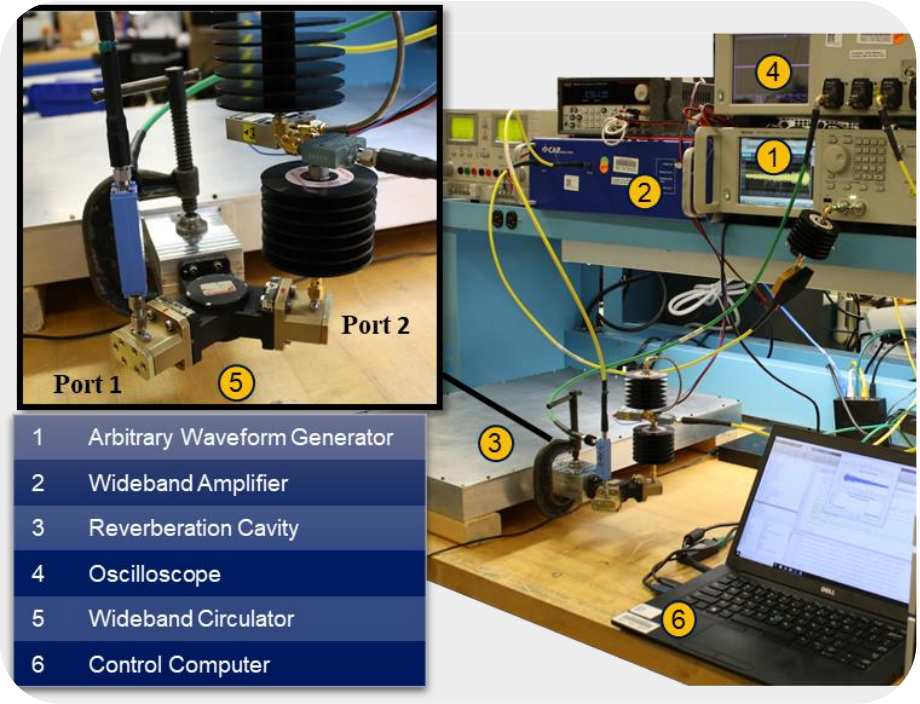

Figure 5-19. Experimental set-up for 'full time-domain' method. Port 2 of the circulator is connected directly to the cavity. Input port and Output port of the TRPC system are labeled Port 1 and Port 2, respectively.

Table 5-6. Compression Gain Comparison: 2-Port Vs. 1-Port Cavity: Regular Time-Reversal

Impulse Response Length (ns)	*PC GAIN (DB): 1-port*	*PC GAIN (DB): 2-port*	*Diff (dB)*
400	15.7	14.6	1.1
600	16.0	14.8	1.2
800	16.2	15.0	1.2
1000	16.2	14.9	1.3
1200	16.2	14.8	1.4
1400	16.3	15.0	1.3
1600	16.2	15.0	1.2

Table 5-7. Compression Gain Comparison: 2-Port Vs. 1-Port Cavity: One-Bit Time-Reversal

Impulse Response Length (ns)	*PC GAIN (DB): 1-port*	*PC GAIN (DB): 2-port*	*Diff (dB)*
400	20.4	18.9	1.5
600	22.0	19.8	2.2
800	23.0	20.4	2.6
1000	23.2	20.6	2.6
1200	23.5	20.6	2.9
1400	23.6	20.6	3.0
1600	23.7	20.7	3.0

port) increases from 1.5 dB at an IR length of 400 ns up to 3.0 dB at an IR length of 1600 ns. For regular TR the difference in compression gain from the simulated results in Table 5-2 stays relatively constant at ~ 1 dB. This discrepancy for regular TR in measurement is likely due to the early times of the time-reversed impulse response having amplitudes too low to rise above the noise floor of the amplifier. This is not observed in simulation because there are no real-world amplifier effects modeled.

Finally, the 1-port measured results using regular TR can be compared to the results in Table 5-5 where the compression gain is simulated using CST-generated cavity reflection coefficient, but using the 3-port scattering parameters of the real circulator. It can be seen that the measured and simulated results are about equal at the lowest impulse response length (400 ns), but quickly increase to a difference of ~1 dB. This is due to leakage in the real cavity, which is not present in the CST-simulated cavity. The comparison is similar for the measured OBTR results and those in Table 5-3 such that the initial difference of ~1.5 dB quickly rises to ~3 dB. This increase in compression gain difference is also due to leakage in the cavity.

5.5 - Analysis and Discussion

5.5.1 - The Statistical Nature of Predictions of Compression Gain

In Figure 5-20 and Figure 5-21 results are plotted from the modeling (section 5.2), simulation (section 5.3), and measurement (section 5.4). It is clear that in all cases 1-port TRPC outperforms 2-port TRPC. In this chapter the gain was computed for the 1600 ns impulse response length for 200 different cavity realizations in a Monte Carlo simulation using the modeled transfer functions. In Figure 5-20 and Figure 5-21 the average compression gain results from the modeling as single data points are also plotted. It was found that for regular TR the average increase in compression gain from 2-port TRPC to 1-port TPRC was 3.7 dB, and the average increase for OBTR was 4.4 dB. But these modeling results do not include circulator insertion loss (IL), which occurs when going from port 1 to port 2 (S_{21}), and when going from port 2 to port 3 (S_{32}). Nor do the modeling results include the effect of circulator isolation. 1.8 dB of average total IL was measured, and it was found that this non-ideal isolation further reduced compression gain by ~2 dB. This loss in the can be accounted for in the modeled results by subtracting 3.8 dB from the results. These results for both regular TR and OBTR are plotted in Figure 5-20 and Figure 5-21 as well. The results of IL and isolation effects are accounted for in the simulation results by using the CST-simulated cavity S-parameters in conjunction with S- parameters from the actual circulator, and also plotted in Figure 5-20 and Figure 5-21.

By including insertion loss and the loss incurred through non-ideal circulator isolation, both modeled and simulated OBTR compression gains come within 0.4 dB and 2.9 dB of the measured results, respectively. For regular TR, the modeled and simulated compression gains come within 0.9 dB and 1.0 dB, respectively. The measured results are always lower than either the modeled or simulated results. This discrepancy can be explained by the fact that loss due to leakage in the measured cavity is not included in either the modeling or simulations.

A final point to note is that the modeled results for compression gain for the 1-port cavity were within 1.1 dB of the full-wave simulations for both regular TR and OBTR, but the 2-port cavity modeling under-predicted the simulated OBTR results by 1.9 dB. An avenue to explore

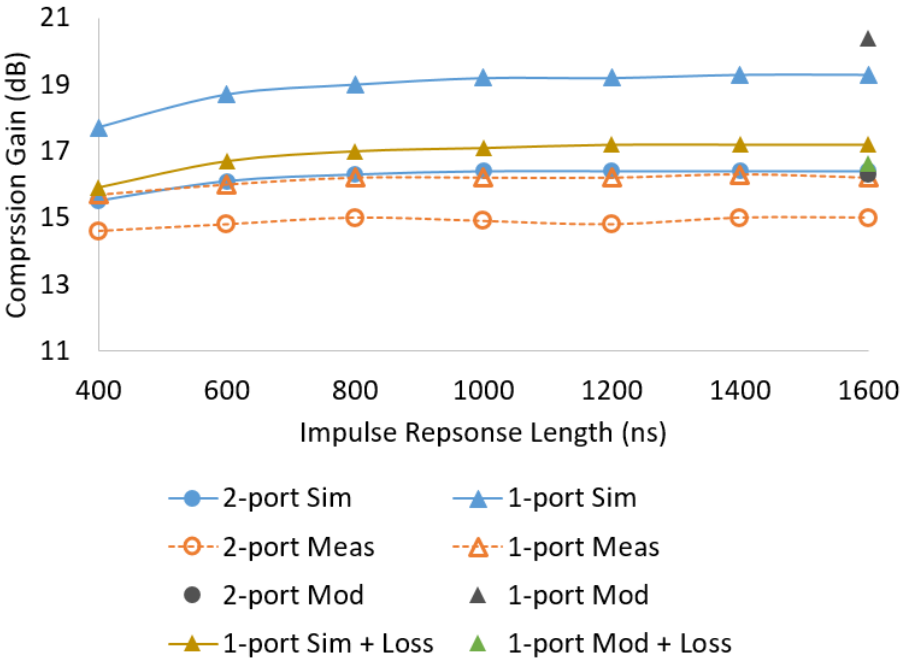

Figure 5-20. Compression gain for the 1-port and 2-port cavities for regular *TR*. Plots include modeling results from section 5.2, simulated results from section 5.3, and measured results from section 5.4. Also included are modeling results with insertion loss and losses incurred from non-ideal isolation, and results from simulations using the CST cavity results and S-params from the real circulator.

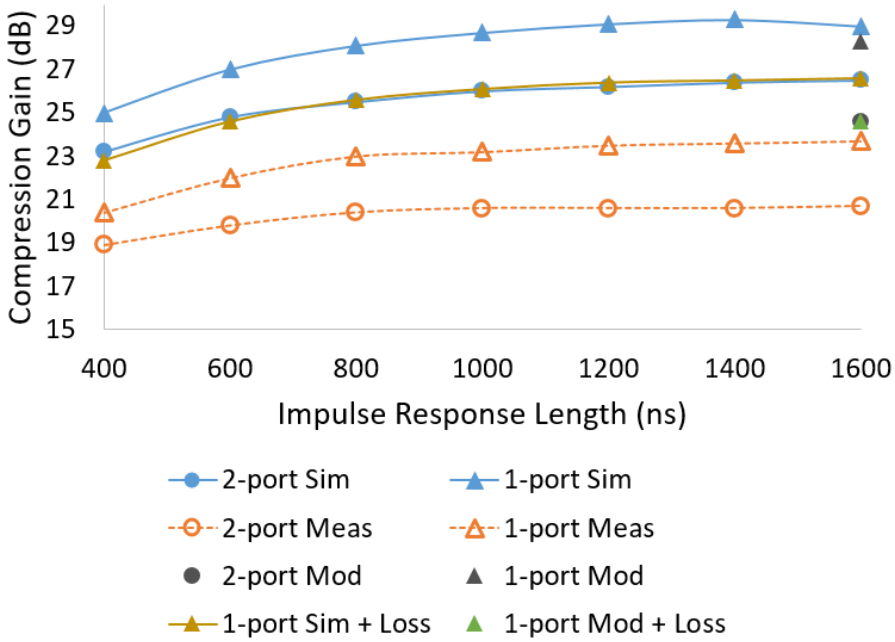

Figure 5-21. Compression gain for the 1-port and 2-port cavities for *OBTR*. Plots include modeling results from section 5.2, simulated results from section 5.3, and measured results from section 5.4. Also included are modeling results with insertion loss and losses incurred from non-ideal isolation, and results from simulations using the CST cavity results and S-params from the real circulator.

regarding this is the assumption of setting the off-diagonal components to zero in the present formulation of the radiation resistance in (5.8) as there may be some relation to this and the poor OBTR predictions. To investigate this further one would have to determine the non-zero off-diagonal components. These values would necessarily be system specific since the off-diagonal component would describe semi-direct coupling paths between port 1 and port 2. They could be determined through measurement, but if a non-measurement method is desired, they may be able to be determined by using the synthetic sona (impulse response) method in [59] whereby the early-time coupling between the ports can be determined using ray-tracing methods constrained by path lengths where only the shortest path lengths are included.

5.5.2 - Cavity Efficiency

In addition to increased gain, an increase in cavity efficiency was found when using one port vs. two ports. The increase was higher in simulation, as expected due to the ideal circulator, but even in measurement there is improvement. To calculate efficiency the same method is used as in [29] and [47] such the cavity efficiency for regular TR is calculated as

$$\eta_{cav}^{TR} = \frac{\int_{t=0}^{t=2*IRL} y(t)^2 \, dt}{\int_{t=0}^{t=2*IRL} h(-t)^2 \, dt} \tag{5.14}$$

where the numerator is the total energy in the cavity output (the reconstructed impulse plus time-sidelobes), and the denominator is the total energy in the cavity input (the time-reversed impulse response). IRL is the impulse response length in seconds. Cavity efficiency for OBTR is similarly calculated as

$$\eta_{cav}^{OBTR} = \frac{\int_{t=0}^{t=2*IRL} y(t)^2 \, dt}{\int_{t=0}^{t=2*IRL} \{sign[h(-t)]\}^2 \, dt} \tag{5.15}$$

In Figure 5-22 the calculated cavity efficiency is plotted for the simulated cases of regular TR and OBTR for the 1-port and 2- port cavities. Here, an 8 percentage point increase in efficiency is seen for regular TR when using one port vs. two ports for this cavity realization. In measurement an average 2 percentage point increase in efficiency when using 1-port is seen. The simulated

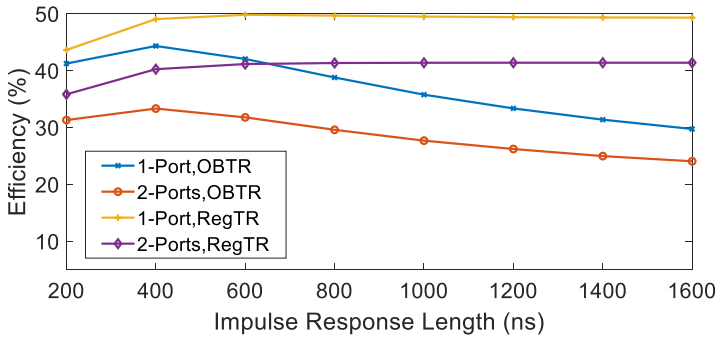

(a)

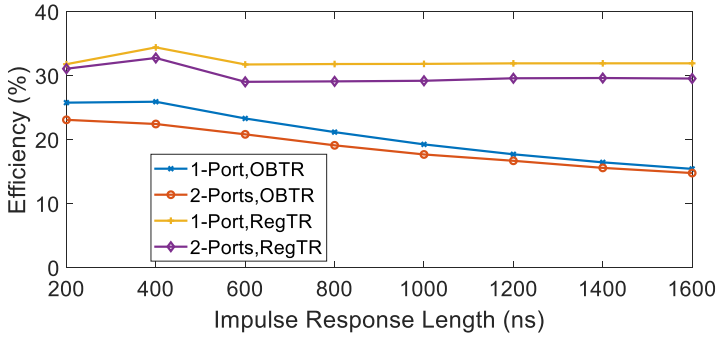

(b)

Figure 5-22. Simulation and measurement results from 5.3 and 5.4 for (a) compression gain for regular TR for the 1- and 2-port cavities, and (b) compression gain results for the 1-port and 2-port cavities for OBTR.

results assume an ideal circulator and do not include the 1.8 dB of total insertion loss, which contribute to reduced efficiency.

5.6 - Summary

A new technique for performing TRPC using a cavity with a single port was presented, including results from both simulation and measurement showing that time-reversal-based pulse compression using a 1-port cavity provides, in all cases, higher gain that can be achieved using a comparable 2-port cavity. Also provided was a novel application of the random coupling model (RCM) to model the compression gain for both 1-port and 2-port cavities. This model, which assumes an ideal circulator with no insertion loss and high isolation, shows an average increase in compression gain using regular TR of 4.1 dB using a 1-port cavity vs a 2-port cavity, and an increase of 3.7 dB for OBTR.

From the measurement results, it was found that the benefit from using 1-port vs. 2-ports (in the example shown) was ~1 dB for regular TR regardless of the impulse response length. For

OBTR the benefit from using a 1-port cavity increased from, 1.5 dB at the lowest IR length (400 ns) to 3 dB at the highest (1600 ns). In simulation, a similar increase was seen for both regular and OBTR. This discrepancy for regular TR in measurement is likely due to the early periods of the time-reversed impulse response having amplitudes too low to rise above the noise floor of the amplifier. This would not be observed in these simulations because real-world amplifier effects were not modeled. This issue is not observed with OBTR because the one-bit operation raises the entire time-reversed signal to equal amplitude before amplification, well above the noise floor.

Cavity efficiency was also examined, and is was found that in simulation there was a ~8 percentage point increase in efficiency using 1-port TRPC rather than 2-port, which is a 20% improvement. This value, though, assumes an ideal circulator and no leakage in the cavity. However, in measurement a ~2 percentage point increase in cavity efficiency is still seen, which is a 7% improvement. There is really no significant difference in implementation in using 1-port vs. 2-port, as long as a wideband circulator with acceptable insertion loss is available, and in all cases studied there was some benefit. In this work, no attempt was made to optimize this cavity to produce optimal compression gain. It has been shown elsewhere, that using a mode-stirrer to select the optimal internal geometry can produce higher compression gain by up to ~2.5 dB. This is the meaning of the modeling results from Figure 5-11 showing increased or decreased gain based on different instances of cavity impedance (cavity realizations). Though even here, an increased number iteration could result in outlying values of compression gain of even higher or lower values. Neither was the optimal ratio of cavity volume to surface area for optimal compression gain modeled. Thus it should remembered that both the simulation and measurement results from sections 5.3 and 5.4 are for a *single cavity realization*. It should be expected that if a mode-stirrer were added, and the compression gain were found for many stirrer positions, then the results could show even more benefit.

It was not specifically studied whether there was any effect of non-linearities from the circulator imparting distortion or otherwise affecting the fidelity of the output pulse with respect to the original excitation. The amplifier used in these experiments to amplify the excitation and time-reversed signals was relatively low power (20 W), which was due to the unavailability of the higher power amplifier from previous work in [47] but higher power signals have been used in other experiments and no obvious distortion has been noticed.

Chapter 6 - Conclusions and Future Work

6.1 - Conclusions

This dissertation presents new techniques and analyses thereof for maximizing compression gain, and obtaining the highest peak output power, from TR-based microwave cavity pulse compressors, for a given volume and material. Several techniques are applied in this work including high-power design, analysis of efficiency, internal geometry optimization, investigation of variation in gain to due to variation in the impulse response recording time and signal bandwidth, and sidelobe reduction in OBTR. Consequently, a new design for a compact, high power pulse-compression cavity that operates with an instantaneous bandwidth of 13 GHz (5 GHz to 18 GHz) has been presented. Results from both full-wave simulations as well as measurements from a fabricated cavity are shown. With an 'empty', un-optimized cavity, 21.2 dB of compression gain was obtained, and using a 100 W peak-power sinc impulse function, 39.2 kW instantaneous peak power output was shown. *This is the highest reported gain and peak output power to date for a pulse compressor of this type*. This empty cavity is currently inefficient with an efficiency of about 22%, though this is a higher efficiency than other similar published pulse compressors. For time reversal pulse compressors, the peak output power is proportional to the magnitude of the input power, such that given an equivalent system, a higher peak input voltage will produce a higher peak output voltage. Table 3-1 provided a comparison of the high-power pulse compressor in this dissertation to other similar systems, and Figure 6-1 shows again the trade space of bandwidth and peak power for different USP sources from Figure 1-1 with high-power TR (HP TR) added to show how this work moves the state-of-the-art in this direction. The new high-power TR (HP TR) data point is expect to be at least 3 dB higher had the 100 W broadband amplifier been used rather than the 20 W amplifier, but the general trend is evident. For future researchers and engineers wishing to increase this even further, the most obvious is to continue to use a higher power broadband amplifier to drive the cavity. Other engineering techniques include electroplating with silver or other high-condivity metal, this was shown to have some benefit in simulation, in Figure 3-3. A further avenue off research to improve gain is through cavity optimization both through use of mode stirrers and through modeling to discover the optimum volume for a given center frequency and bandwidth.

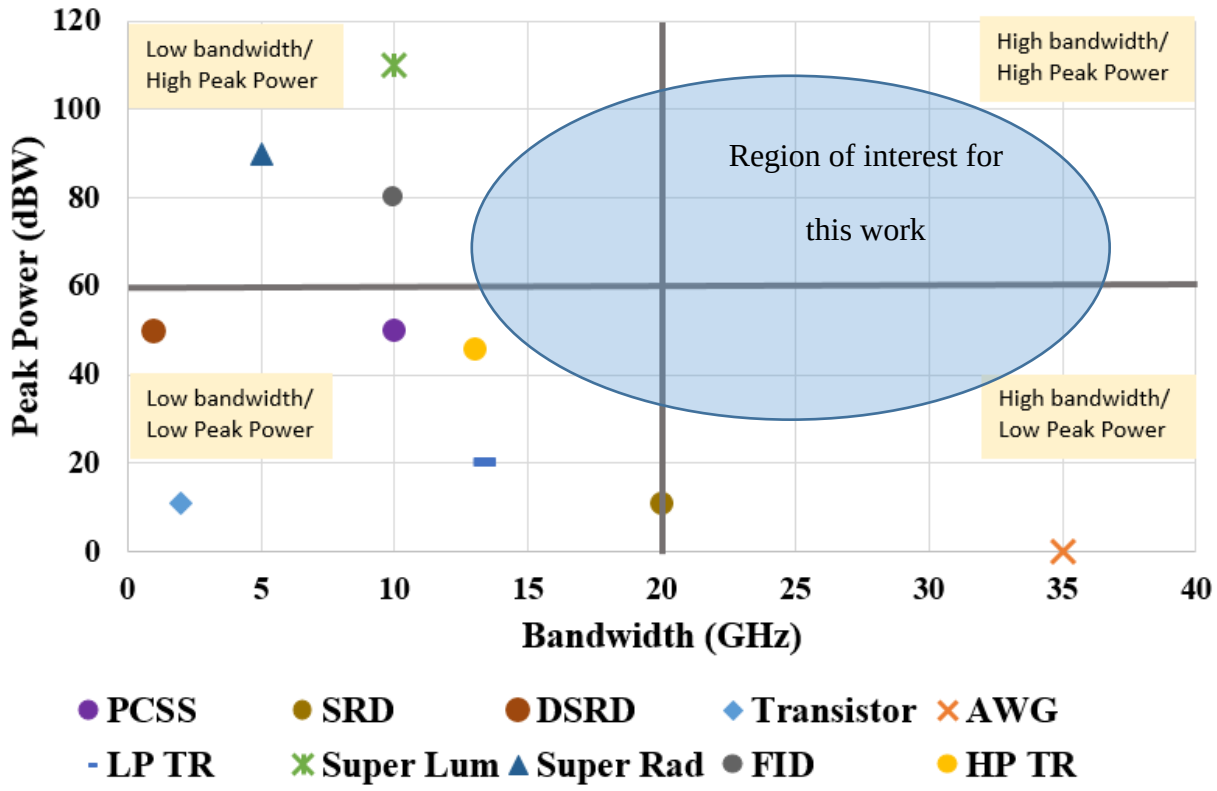

Figure 6-1. Trade space of bandwidth and peak power for different USP sources from Figure 1-1 with high-power TR (HP TR) added to show how this work moves the state-of-the-art in this direction.

Additionally, a novel technique was introduced for increasing compression gain using fast microwave switches on the input in order to better store the energy in the cavity after the impulse has entered the cavity on the impulse response recording part of the pulse compression process. The author has implemented this technique for the first time with PIN-diode switches. This was successful in increasing the cavity quality factor, and providing a higher-energy recorded impulse response, but upon applying the OBTR procedure and re-transmitting, the high peak power at the output (incident on the PIN-diode switch) caused the PIN-diode switch to act as a PIN-diode limiter, thus not allowing full impulse reconstruction to be achieved. However, it was discovered though that this technique can be used to eliminate time-sidelobes in the OBTR impulse reconstructions as well, though only for very low-power systems since the current technology for these fast microwave admit only peak power levels of well below 10 W.

Finally, a new technique for performing TRPC using a cavity with a single port was presented. Simulation and measurement results were presented showing that time-reversal-based

pulse compression using a 1-port cavity provides, in all cases, higher gain that can be achieved using a comparable 2-port cavity. A novel application of the random coupling model (RCM) to model the compression gain for both 1-port and 2-port cavities was provided. This model, which assumes an ideal circulator with no insertion loss and high isolation, shows an average increase in compression gain using regular TR of 4.0 dB using a 1-port cavity vs a 2-port cavity, and an increase of 4.4 dB for OBTR.

From measured results, it was found that the benefit from using 1-port vs. 2-ports (in the example in this dissertation) was ~1 dB for regular TR regardless of the impulse response length. For OBTR the benefit from using a 1-port cavity increased from, 1.5 dB at the lowest IR length (400 ns) to 3 dB at the highest (1600 ns). In simulation a similar increase for both regular and OBTR was seen. This discrepancy for regular TR in measurement is likely due to the early periods of the time-reversed impulse response having amplitudes too low to rise above the noise floor of the amplifier. This would not be observed in these simulations because real-world amplifier effects were not modeled. This issue is not observed with OBTR because the one-bit operation raises the entire time-reversed signal to equal amplitude before amplification, well above the noise floor.
Cavity efficiency was also examined and it was found that in simulation there was a ~8 percentage point increase in efficiency using 1-port TRPC rather than 2-port, which is a 20% improvement. This value, though, assumes an ideal circulator and no leakage in the cavity. However, in measurement there is still a ~2 percentage point increase in cavity efficiency, which is a 7% improvement. There is really no significant difference in implementation in using 1-port vs. 2-port, as long as a wideband circulator with acceptable insertion loss is available, and in all cases that were studied there was some benefit.

In this case, optimizing the cavity to produce optimal compression gain was not attempted. It has been shown elsewhere, [29], [47], that using a mode-stirrer to select the optimal internal geometry can produce higher compression gain by up to ~2.5 dB. This is the meaning of the modeling results in Figure 5-11 showing increased or decreased gain based on different instances of cavity impedance (cavity realizations). Though even here, an increased number iterations could result in even higher or lower values of compression gain. Neither was the optimal ratio of cavity volume to surface area for optimal compression gain modeled. Thus, it should remembered that both the simulation and measurement results from sections 5.3 and 5.4 are for a *single cavity*

realization. It should be expected that if a mode stirrer were added, and the compression gain were found for many stirrer positions, then the proposed one-port system could show even more benefit.

The author did not specifically study whether there was any effect of non-linearities from the circulator imparting distortion or otherwise affecting the fidelity of the output pulse with respect to the original excitation. The amplifier used in these experiments to amplify the excitation and time-reversed signals was operating at relatively low power (20 W), but the author has used higher power signals in other experiments and noticed no obvious distortion. However, this is something that can be studied in future research.

6.2 - Future Work

The results of this dissertation work are promising, but several questions were raised, which require further research. For instance, excellent agreement was seen between the modeling results and those of the 1-port simulations. However, the modeling results under-predicted the simulation results for the two-port case. One can speculate that this could be due to assumptions made in the modeling such as assuming no coupling paths from port 1 to port 2. Also, the modeling-plus-loss case was slightly lower the measurement when using regular TR. In future work the maximization of compression gain through both optimization of internal cavity geometry using a mode-stirrer as well as through the exploration the optimal ratio of volume to surface area will be pursued. The model will be further investigated with non-zero values for the off-diagonal components in the radiation impedance using techniques described in [59]. The change in the mean statistics of compression gain change over many Monte Carlo simulations will also be investigated; for instance, increasing the number of iterations per simulation (currently 200) may reveal higher or lower outlying values for compression gain than was seen with only 200 iterations.

Appendix A - Multiple-Post Height Optimization

At the end of section 3.6 a potential technique was described for optimizing the internal cavity geometry for optimal compression gain whereby a cavity with a series of metal posts that could be raised or lowered according to the output of a genetic algorithm was devised, although the proposed approach had drawbacks that limited its effectiveness in achieving high compression gain and power. In the devised scheme, there are 88 posts, and even if each post had only two heights then there would be 2^{88} permutations! This is too many to ever try them all. Instead, optimization algorithms will be used to find the correct post height profile that provides the maximum cavity gain. The pulse compression cavity is an electromagnetic wave propagation system. Methods for optimizing electromagnetic systems, including antennas and arrays in some cases, generally rely on training-data sets or on the problem being convex, or otherwise not susceptible to being stuck in a local minimum. The problem of optimization of array element geometry, in this case an array of posts, is best suited to metaheuristic algorithms, the most popular of which are genetic algorithms (GAs) and particle swarm optimization (PSO). GAs became popular in the late 1980's and 1990's due to the work of Goldberg [60], Holland [61], Haupt [62-64], and Johnson [65]. They are ideal for selecting optimum configurations from a large population (posts with different heights) and can be used to optimize multiple parameters simultaneously.

A.1 - Genetic Algorithms for Post Height Optimization

The general procedure for performing optimization using GAs is well-described elsewhere, [62, 63, 65] but will be reviewed here for completeness. GAs do not work on the actual parameters in the objective function, but rather on an encoded version, generally binary-encoded. A parameter can be encoded using a single bit or multiple bits. Thus, if the objective function is described generally as a function of one or more parameters as

$$fun_{obj} = \left(p_1, p_{2,\ldots,} p_N\right) \tag{A.1}$$

then the parameters can be encoded as (for example)

$$p_1 = 1011, \qquad p_2 = 0111, \quad p_N = 1110 \tag{A.2}$$

and so forth. These encoded parameters may then be concatenated to create chromosomes (if the objective function has more than one parameter). So, for example

$$chromosome = \underbrace{1011}_{p_1}\underbrace{0111}_{p_2}\ldots\underbrace{1110}_{p_N} \tag{A.3}$$

M chromosomes may now be randomly generated such that they from an MxN matrix with each row corresponding to a different chromosome—this is the initial population. Now, the objective/cost function may be evaluated for each chromosome to produce the cost. The chromosomes are then ranked by cost from lowest (if minimizing) to highest, and the bottom half are rejected. The remaining chromosomes may be mated by cutting them at random crossover points and joining pairs to form new chromosomes to replace the ones that were discarded. Then, a random mutation is introduced (this keeps the algorithm from getting stuck in a local minimum). This is now a new population, which can be decoded and evaluated using the objective function. The process is repeated. The flowchart in Figure A-1 below depicts the process.

The first step will be to randomly choose an initial population of post configurations. The possible post heights will be constrained to be 0 cm, 1 cm, 2 cm, 3 cm, or 4 cm. Each configuration is a set of 92 posts with initially random heights. The TR process will then be performed to obtain a gain value. The best configurations will be chosen from the initial population and new 'child' populations with be created from the good 'parent' populations, and the process will be repeated.

A.2 - Fabrication of Post-Grid Optimization Apparatus

Each post has its own linear actuator and is raised or lowered based on GA results calculated in MATLAB. Figure A-2 shows two actuators connected to their respective posts. Each

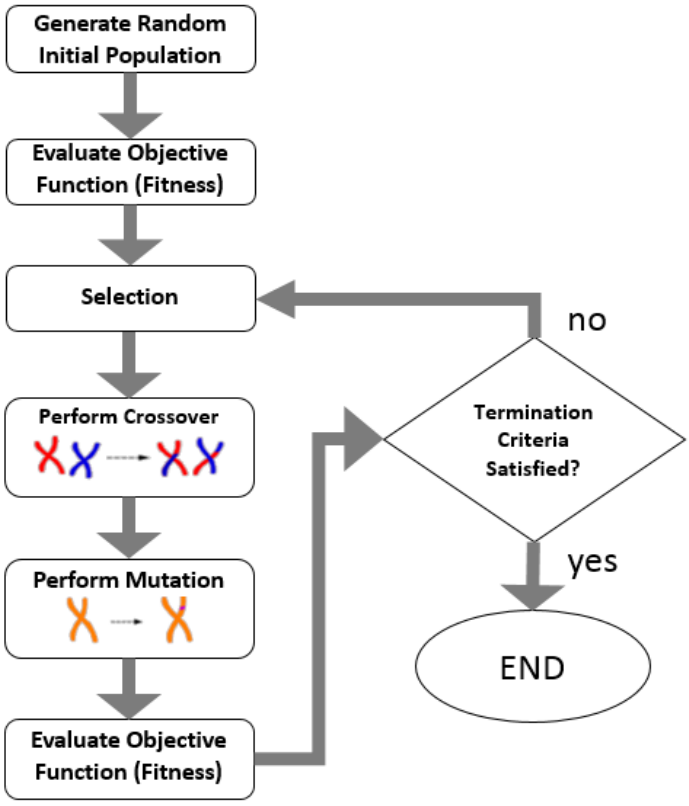

Figure A-1. Flowchart Describing GA decision process.

actuator must be controlled by two relays (Figure A-3), which supply either +12 V or -12 V depending on whether the actuator is moving up or down.

The movement itself and each post must be set according to the GA is controlled by an Arduino in communication with MATLAB running on a laptop. Before setting the post heights, a calibration is performed where all posts are 'sent' to the bottom of the cavity. Once they hit bottom, the change in current on the power supply due to the stopping force of the posts hitting the bottom tells where to 'zero out' the posts. Each post may then be raised or lowered, simultaneously to execute pulse compression with a particular post-height population.

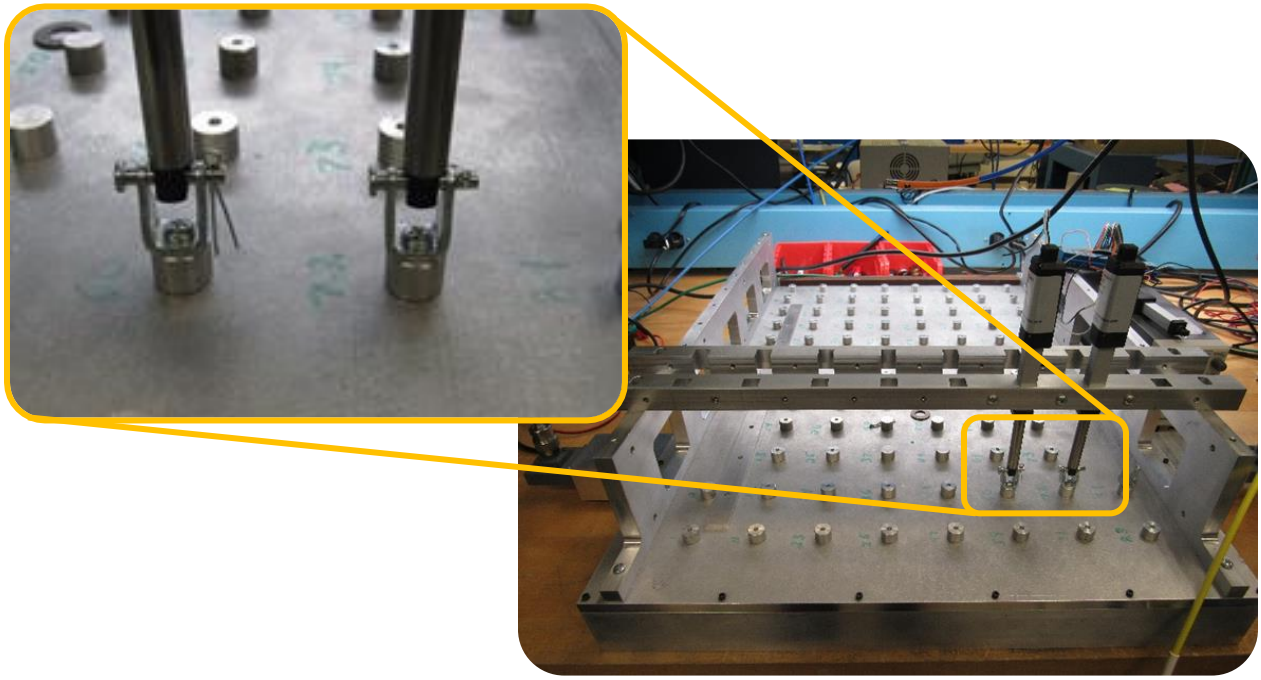

Figure A-2 - Two linear actuators shown in holders and connected to posts.

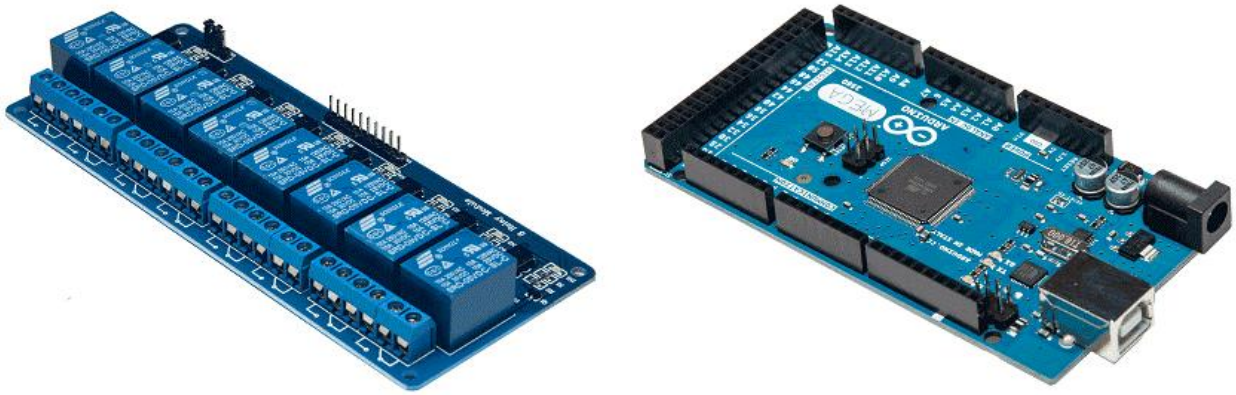

Figure A-3. Eight-channel relay module (left) controls 4 relays (+12 V, up; -12 V down). Arduino Mega microcontroller (right) controls each relay.

Appendix B - Further Measurements for Time-sidelobe Reduction

Following the initial results in Chapter 4 additional experiments were performed using the same Narda S213D PIN-diode switch and experimental setup. These experiments were performed at a later time and the equipment used was that shown in Figure 5-18 rather than Figure 3-5. Also in the experiments in Chapter 4, electromechanical switches were used to switch between the interrogation transmit/receive paths and the reconstruction transmit/receive paths. This was done in order to automate the process of executing on the two measurement states shown in Figure 4-3. For the measurements described here, the two measurement states were achieved by manually moving the transmit apparatus and the receive apparatus from one port of the cavity to the other as shown in Figure B-1.

Figure B-2 (a) shows a reconstructed impulse due to a low-power (1.14 W) input. 14.5 dB of gain was achieved. Figure B-2 (b) shows that upon increasing the input power level to ~8 W, reduced gain can be seen that due to the limiting behavior of the Narda S213D PIN-diode switch. Figure B-3 shows results for keeping the switch open during the entire TRPC process. As expected, no time-sidelobe reduction occurs, but the same limiting phenomenology is observed. Figure B-4 shows a comparison of reconstructed waveforms to show that, while there is still some distortion of the waveform for the low-power switch experiments, there is still further distortion incurred during the high-power experiments.

Next, in Figure B-5, a TRPC measurement is conducted with a different non-PIN-diode fast microwave switch and the same elimination of time-sidelobes can be seen when the switch is active. A high-power experiment was not conducted in this case, but it is expected that even if

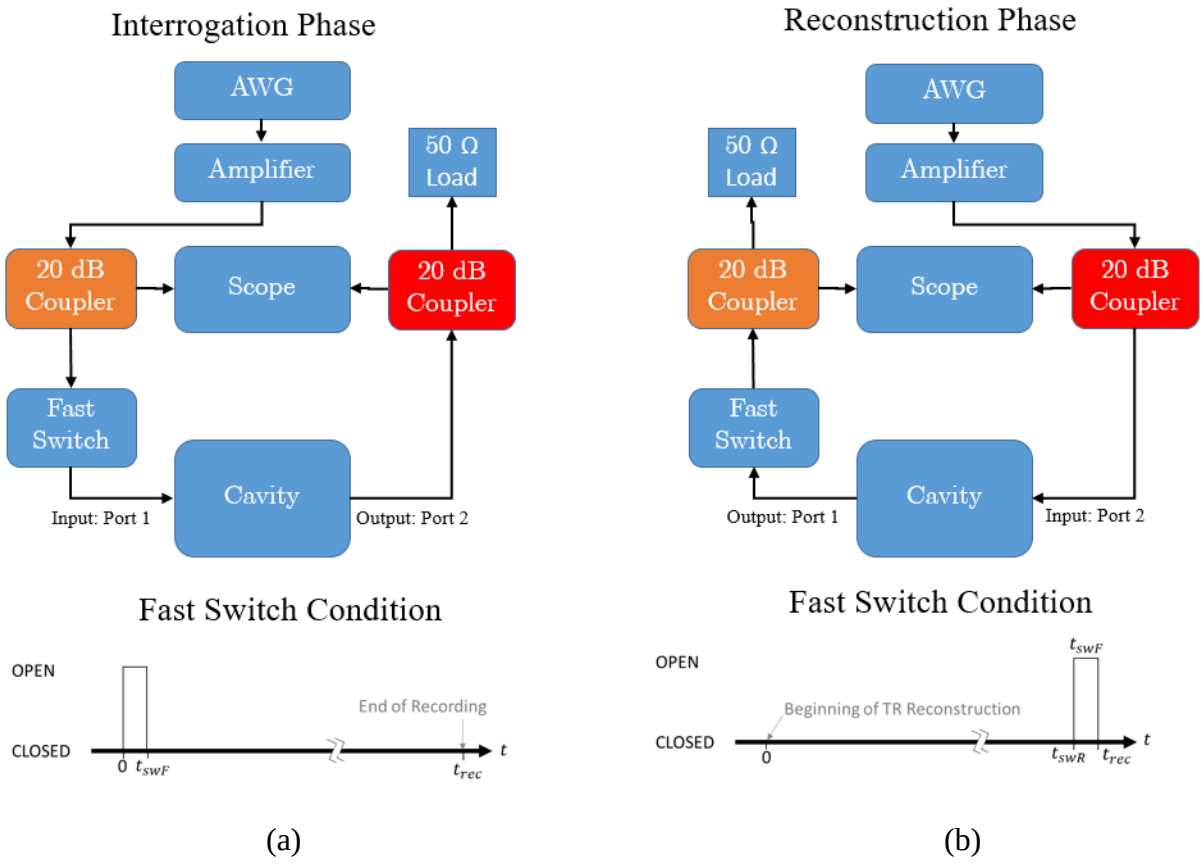

(a) (b)

Figure B-1. (a) Measurement setup for the interrogation phase where the impulse response is measured, and which corresponds to the switch allowing signal to pass for less than 100 ns. (b) Measurement setup for the reconstruction phase where the reconstructed impulse is measured, and which corresponds to the switch only allows signal to pass during the last 100 ns or less while blocking signal for the first ~900 ns.

there were no limiting, the switch can only handle ~3 W of average power, so this would still not be suitable for high-power operation. In Figure B-6, the impulse responses are compared for the switching and non-switching cases for both types of switches tested. There is not as much of a difference noticed as in Figure 4-4, but a higher loaded quality factor is still found in the switching case for the PIN-diode switch versus the non-switching case. The difference is more obvious when a moving average is applied to the impulse responses shown in Figure B-6(b) as shown in Figure B-7. It can now be clearly seen that the switching case produces a higher loaded quality factor, but it is not significant enough to produce increased compression gain. The 1-port technique from Chapter 5 is better for this.

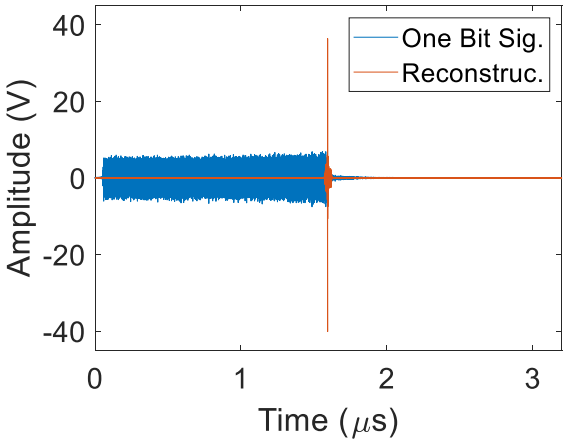

Max Input Power [W]: 1.14
Max Output Power [W]: 32.2
Gain [dB]: 14.5

(a)

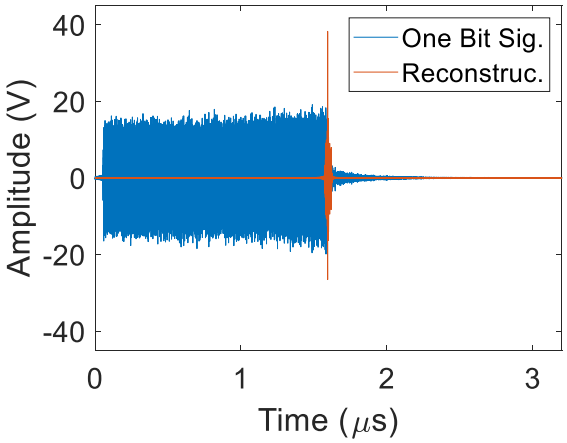

Max Input Power [W]: 7.91
Max Output Power [W]: 29.3
Gain [dB]: 5.7

(b)

Figure B-2. Results from measurements using switching scheme from Figure B-1 for (a) Low-power OBTR input signal and reconstructed signal showing no early time-sidelobes and 14.5 dB compression gain. (b) High-power OBTR input showing no early time-sidelobes, but also reduced gain due to limiting of the reconstructed impulse. Switch used is Narda S213D.

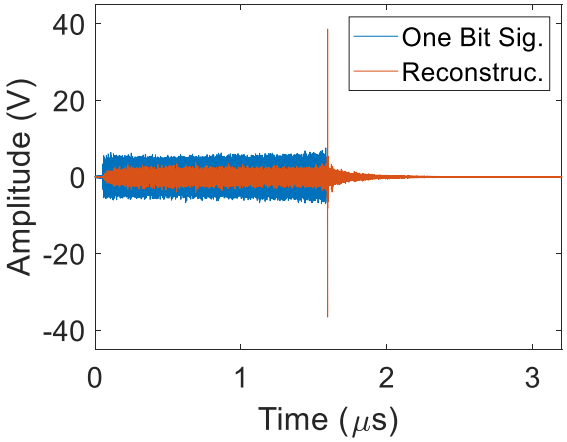

Max Input Power [W]: 1.14
Max Output Power [W]: 29.8
Gain [dB]: 14.1

(a)

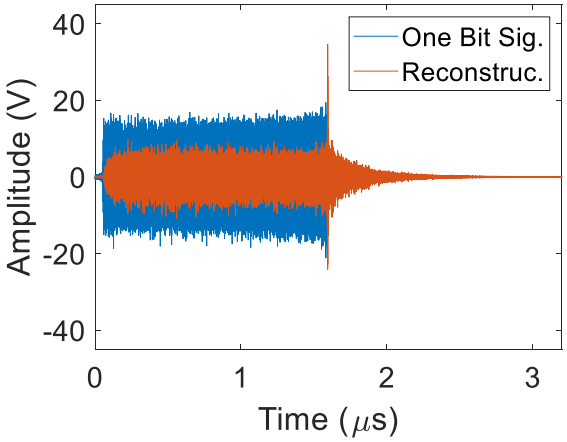

Max Input Power [W]: 8.94
Max Output Power [W]: 23.93
Gain [dB]: 4.3

(b)

Figure B-3. Results from measurements using setup from Figure B-1, but with no switching. (a) Low-power OBTR input signal and reconstructed signal showing early time-sidelobes and 14.1 dB compression gain. (b) High-power OBTR input showing early time-sidelobes, but also a limited reconstructed impulse and reduced gain. Switch used is Narda S213D.

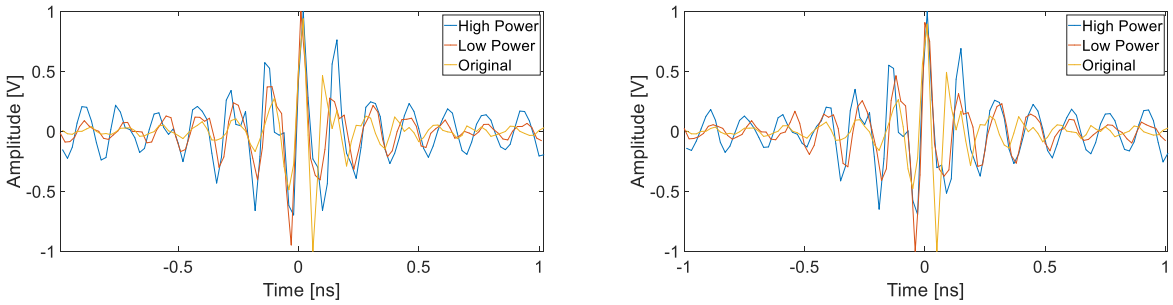

(a) (b)

Figure B-4. (a) Comparison of impulse responses from low-power and high-power measurements and the original impulse when the switch does not block any signal. (b) Comparison of impulse responses from low-power and high-power measurements and the original impulse when the switch performs the switching scheme from Figure B-1.

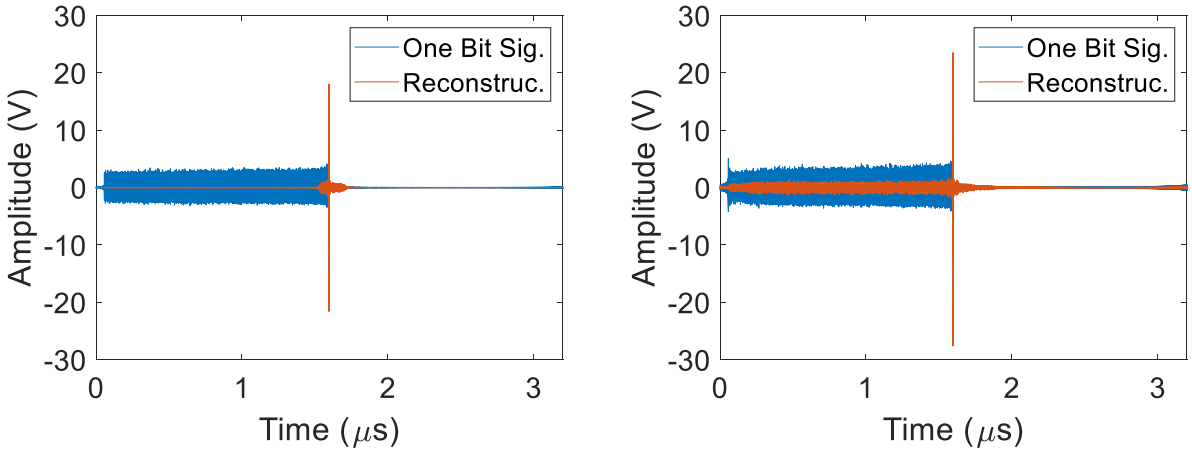

Gain [dB]: 14.3 Gain [dB]: 14.7

(a) (b)

Figure B-5. (a) Low-power OBTR input signal and reconstructed signal showing no early time-sidelobes and 14.3 dB compression gain. Switching is executed according to Figure B-1 for (b) Low-power OBTR input signal and reconstructed signal showing early time-sidelobes and 14.7 dB compression gain. Here, switch always allows signal to pass. Switch use is RF Lambda RFSP2TRDC18G.

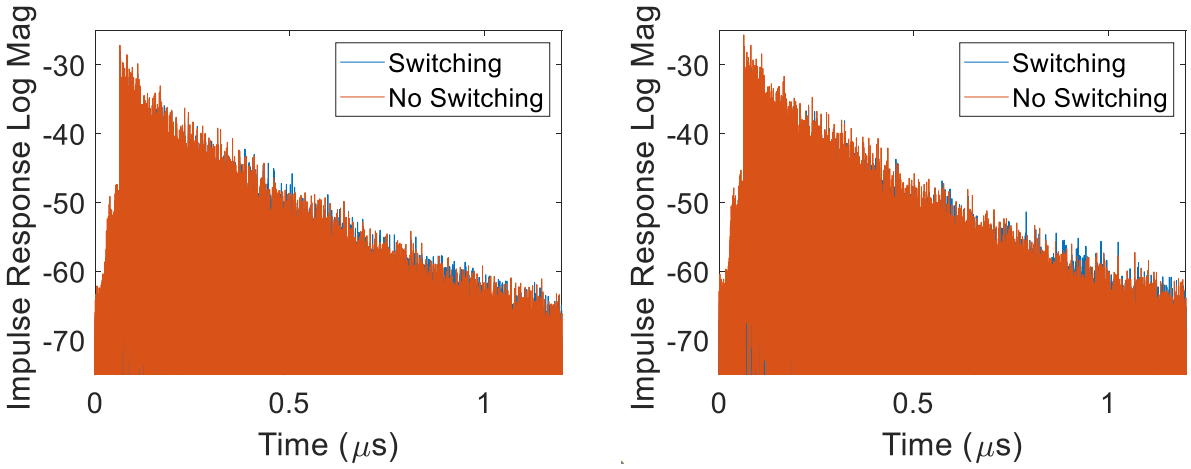

(a) (b)

Figure B-6. (a) Impulse response using RF Lambda RFQ135225 fast microwave switch. (b) Impulse response using Narda S213D fast microwave PIN-diode switch. In both, it is difficult to see the increase in the loaded quality factor when the switching technique is used.

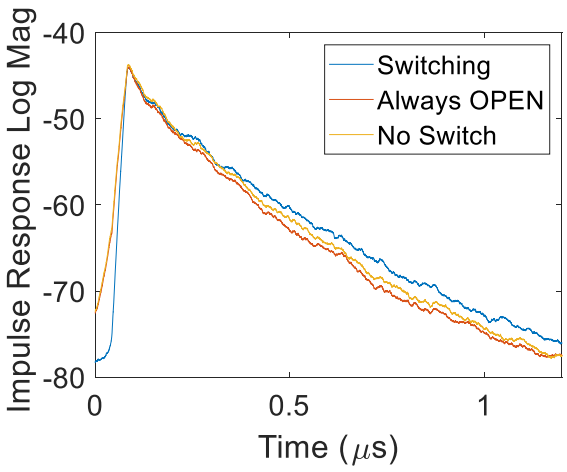

Condition	Quality Factor	Time Constant (τ) – [ns]
Switching	8912	120.7
No Switch	7997	108.3
Always Open	7836	106.1

(a) (b)

Figure B-7. (a) Impulse responses from Figure B-6(b) plus an impulse response with no switch as all with a moving average applied to show an increase in energy (leading to a higher quality factor) in the switching case. (b) Calculated loaded quality factors and time constants from the plots in (a).

References

[1] T. Zwick, W. Wiesbeck, J. Timmermann, and G. Adamiuk, *Ulta-wideband RF System Engineering*. Cambridge University Press, 2013.

[2] J. Reed, Ed. *An Introduction to Ultra Wideband Communication Systems* (Prentice Hall Communications Engineering and Emerging Technologies Series). Upper Saddle River, NJ: Prentice Hall, 2005, p. 653.

[3] J. D. Taylor, Ed. *Ultra-Wideband Radar Technology*, 1st ed. Boca Raton, FL 33431: CRC Press LLC, 2000, p. 424.

[4] J. D. Taylor, Ed. *Ultrawideband Radar: Applicat. and Design*, 1st ed. Boca Raton, FL: CRC Press, Taylor and Francis Group, 2001.

[5] S. Foo, A. Walsh, and S. Kashyap, "Ultra-wideband (UWB) Remote Sensing and Radar Imaging," Defense R&D Canada, Ottawa, 2004.

[6] P. Shrivastava, A. Agarwal, and R. K. Shevgaonkar, "Target Signature Recognition Using Ultra Short Pulse Radar," in *14th International Radar Syposium (IRS)*, Dresden, Germany, 2013.

[7] C. Nguyen and J. Han, *Time-Domain Ultra-Wideband Radar, Sensor and Components* (Springer Briefs in Electrical and Computer Engineering). Switzerland: Springer International, 2014, p. 133.

[8] J. D. Taylor, Ed. *Advanced Ultrawideband Radar: Signals, Targets, and Applicat.* Boca Raton, FL 33487: CRC Press, Talylor & Francis Group, 2017.

[9] Y. N. Lazarev and P. V. Petrov, "Generation of an intense, directed, ultrashort electromagnetic pulse," *Pis'ma Zh. Eksp. Teor Fiz,* vol. 60, no. 9, pp. 625-628, 1994.

[10] Y. N. Lazarev, P. V. Petrov, and Y. G. Syrtsova, "Microwave Generation by a Superluminal Source at Limiting Current Densities," *Plasma Physics Reports,* vol. 29, no. 6, pp. 491 - 502, 2003.

[11] I. V. Zotova *et al.*, "Amplification and Nonlinerar Compression of Ultrashort Microwave Pulses by Quasi-Stationary Electron Beams: Theory and Experiment," *J. of the Korean Physical Soc.*, vol. 59, no. 6, pp. 3503 - 3507, 2011.

[12] S. D. Korovin *et al.*, "Generation of Cherenkov superradiance pulses with a peak power exceeding the power of driving short electron beam," *Phys. Rev. E,* vol. 74, 2006.

[13] L. Zou, S. Gupta, and C. Caloz, "A Simple Picosecond Pulse Generator Based on a Pair of Step Recovery Diodes," *IEEE Trans. Microw. Wireless Compon. Lett.*, vol. 27, no. 5, pp. 467 - 469, 2017.

[14] M. S. Nikoo and S. M.-A. Hashemi, "A Compact MW-Class Short Pulse Generator," *A Compact MW-Class Short Pulse Generator*, vol. 46, no. 6, pp. 2059-2063, 2018.

[15] D. S. A. Boryssenko, "Tunable pulse generators based on Drift-Step Recovery effect in COTS power rectifier diodes," presented at the COMCAS'13, 2013.

[16] F. Arntz, M. Gaudreau, M. Kempkes, A. Krasnykh, and A. Kardo-Sysoev, "A Kicker Driver For The International Linear Collider," presented at the PAC07, 2014.

[17] V. Efanov, "Gigawatt All-Solid-State Nano- and Picosecond Pulse Generators for Radar Applications," vol. 14, ed. Savoy Place, London WC2R 0BL, UK: The Institution of Electrical Engineers, 2003.

[18] J. R. Andrews, "Picosecond Pulse Generation Techniques & Pulser Capabilities," *Picosecond Pulse Labs Application Note 19*, pp. 1 - 8, 2008.

[19] S. Kohler, V. Couderic, R. P. O'Connor, D. Arnaud-Cormos, and P. Leveque, "A Versatile High Voltage Nano- and Sub-nanosecond Pulse Generator," *IEEE Trans. Dielectr. Electr. Insul.*, vol. 20, no. 4, pp. 1201 - 1208, 2013.

[20] G. Mourou, C. V. Stancampiano, and D. Blumenthal, "Picosecond microwave pulse generation," *Appl. Phys. Lett.*, vol. 38, no. 6, pp. 470 - 72, 1981.

[21] L. Zhang *et al.*, "Experimental Study of Microwave Pulse Compression Using a Five-fold Helically Corrugated Waveguide," *IEEE Trans. Microw. Theory Tech.*, vol. 63, no. 3, pp. 1090 - 1096, 2015.

[22] R. Paschotta, "Encyclopedia of Laser Physics and Technology," ed: RP Photonics.

[23] E. Mokole, L., "Examples of Ultrawideband Definitions and Waveforms," in *Principles of Waveform Diversity and Design*, M. M. Wicks, Eric, L.; Blunt, Shannon ; Schneible, Richard; Amuso, Vincent Ed. Raleigh, NC: Scitech Publishing, 2010.

[24] B. P. Bogert, "Demonstration of Delay Distortion Correction by Time-Reversal Techniques," Bell Telephone Laboratories, Inc., Murray Hill, New Jersey, 1957.

[25] M. Fink, C. Prada, and D. Cassereau, "Self-Focusing in Inhomogeneous Media with Time Reversal Acoustic Mirrors," in *Ultrasonics Symposium*, Paris, France, 1989.

[26] D. R. Jackson and D. R. Dowling, "Phase conjugation in underwater acoustics," *Journal of the Acoustical Society of America*, vol. 89, no. 1, pp. 172 - 181, 1991.

[27] M. Fink, "Time Reversal of Ultrasonic Fields-Part I: Basic Principles," *IEEE Transactions on Ultrasonics, Ferroelectrics,a nd Frequency Control*, vol. 39, no. 5, pp. 555 - 566, 1992.

[28] G. Lerosey, J. de Rosny, A. Tourin, A. Derode, G. Montaldo, and M. Fink, "Time Reversal of Electromagnetic Waves," *Phys. Rev. Lett.*, vol. 92, no. 19, 2004.

[29] S. K. Hong, E. Lathrop, V. M. Mendez, and J. Kim, "Ultrashort Microwave Pulse Generation by Passive Pulse Compression in a Compact Reverberent Cavity," *Progress in Electromagnetic Research*, vol. 153, pp. 113 - 121, 2015.

[30] H. Vallon, "Focusing High-Power ElectroMagnetic Waves Using Time-Reversal," Doctoral, Electrical, Optical, Bio-Physics and Engineering, L'université Paris-Saclay, France, 2016SACLC006, 2016.

[31] S. K. Hong and H. S. Park, "Ultra-compact pulse compressor for generating ultrawideband short pulses," *Electronics Letters*, vol. 54, no. 12, pp. 768 - 770, 2018.

[32] S. Smith, L. ; Licklider, J. C., R. , "Noneffect upon Speech Intelligibility of Phase Distortortion Produced by HighPass and Low-Pass Filters," *The Journal of the Acoustical*

Society of America, vol. 26, no. 138, 1954. [Online]. Available: https://doi.org/10.1121/1.1917771.

[33] G. d. R. Lerosey, J.; Tourin, A.; Derode, A. ; Fink, M. , "Time reversal of wideband microwaves," *Applied Physics Letters,* vol. 88, no. 15, p. 3, 2006, doi: 10.1121/1.1421342.

[34] M. d. R. Davy, Julien; Fink, Mathias "Focusing and amplification of electromagnetic waves by time-reversal in an leaky reverberation chamber," 2009.

[35] S. K. Hong, B. T. Taddese, Z. B. Drikas, S. M. Anlage, and T. D. Andreadis, "Focusing an arbitrary RF pulse at a distance using time-reversal techniques," *Journal of Electromagnetic Waves and Applications,* vol. 27, no. 10, pp. 1262 - 1275, 2013.

[36] H. T. Nguyen, J. B. Andersen, G. F. Pedersen, P. Kyritsi, and P. C. F. Eggers, "Time Reversal in Wireless Communications - A Measurement-based Investigation," *IEEE Trans. Wireless Commun.,* vol. 5, no. 8, pp. 2242 - 2252, 2006.

[37] R. L. Razzaghi, G.; Paolone, M.; Rachidi, F., "Electromagnetic Time Reversal Applied to Fault Location in Power Networks," in *Electromagnetic Time Reversal*, F. R. Rachidi, Marcos; Paolone, Mario Ed. Hoboken, NJ: John Wiley & Sons, 2017, ch. 7, pp. 217-274.

[38] A. Derode, A. Tourin, and M. Fink, "Ultrasonic pulse compression with one-bit time reversal through multiple scattering " *Journal of Applied Physics,* vol. 85, no. 9, pp. 6343 - 6352, 1999.

[39] S. Hemmady, "Statisical Prediction and Measurement of Induced Voltages on Components within Complicated Enclosures: A Wave-Chaotic Approach," *IEEE Trans. Electromagn. Compat.,* vol. 54, no. 4, pp. 758 - 771, 2012.

[40] L. Arnaut, R, "Statistics of the Quality Factor of a Rectangular Reverberation Chamber," *IEEE Trans. Electromagn. Compat.,* vol. 45, no. 1, pp. 61 - 76, 2003.

[41] L. Arnaut, R; Besnier, Philippe; Sol, Jerome; Ionut, Andries, M, "On the Uncertainty Quantification of the Quality Factor of Reverberation Chambers," *IEEE Trans. Electromagn. Compat.,* 2018.

[42] A. Cozza, "Statistics of the performance of time reversal in a lossy reverberating medium," *Physical Review E,* vol. 80, no. 056604, 2009.

[43] M. Davy, M. Fink, and J. d. Rosny, "Amplification of Electromagnetic Waves using Time Reversal," in *Electromagnetic Time Reversal*, F. Rachidi, M. Rubinstein, and M. Paolone Eds. Hoboken, NJ: John Wiley & Sons, Inc., 2017, ch. 4, pp. 145 - 167.

[44] M. Fink, "Time-reversal waves and super resolution," *J. Phys.: Conf. Ser.,* vol. 124, no. 012004, 2008.

[45] G. T. Montaldo, M.; Fink, M., "Real time inverse filter focusing through iterative time reversal," *J. Acoust. Soc. Am.,* vol. 115, no. 2, pp. 768-775, 2004.

[46] B. Taddese, T.; Antonsen, T., M.; Ott, E.; Anlage, S., M., "Iterative Time Reversal with Tunable Convergence," *Electronics Letters,* vol. 47, no. 21, 2011.

[47] Z. Drikas, B.; Addissie, Bisrat, D.; Mendez, Victor, M.; Raman, Sanjay, "A Compact, High-Gain, High-Power, Ultra-Wideband Microwave Pulse Compressor using Time-

Reversal Techniques," *IEEE Trans. Microw. Theory Techn.,* 2020, doi: 10.1109/TMTT.2020.3003037.

[48] J. Ladbury, M.; Hill, David, A., "Enhanced Backscatter in a Reveberation Chamber," National Institute of Standards and Technology (NIST), 325 Broadway MS818.02 Boulder, CO 80305 USA.

[49] A. Cozza, "Power Loss in Reverberation Chambers by Antennas and Receivers," *IEEE Trans. Electromagn. Compat. Lett.,* vol. 60, 6, pp. 2041 - 2044, 2018.

[50] D. Hill, A., *Electromagnetic Fields in Cavities: Deterministic and Statistical Theories* (The IEEE Press Series on Electromagnetic Wave Theory). Hoboken, New Jersey.: Published by John Wiley & Sons, Inc., 2009, p. 280.

[51] J.-B. L. Gros, Oliver; Mortessagne, Fabrice; Richalot, Elodie; Selemani, Kamardine, "Universal Behavior of a wave chaos based electromoagnetic reverberation chamber," *Wave Motion,* vol. 51, pp. 664-672, 2013.

[52] G. Y. Gradoni, Jen-Hao; Xiao, Bo; Antonsen, Thomas, M.; Anlage, Steven, M.; Ott, Edward, "Predicting the statistics of wave transport through chaotic cavities by the random coupling model: A review and recent progress," *Wave Motion,* vol. 51, no. 4, pp. 606 - 621, 2014.

[53] S. M. A. Anlage, Bisrat; Antonsen, Thomas; Hart, James; Hemmady, Sameer; Yeh, Jen-Hao; Rodgers, John; Gradoni, Gabriele; Ott, Edward; Taddese, Biniyam; Xiao, Bo; Zheng, Xing; Zhou, Min. "The Random Coupling Model: A User's Guide." University of Maryland. http://anlage.umd.edu/RCM/ (accessed 05 July 2020, 2020).

[54] X. Zheng, T. M. Antonsen, and E. Ott, "Statistics of Impedance and Scattering Matrices in Chaotic Microwave Cavities: Single Channel Case," *Electromagnetics,* vol. 26, no. 1, pp. 3-35, 2006/01/01 2006, doi: 10.1080/02726340500214894.

[55] B. R. Addissie, John; Antonsen, Thomas, "Extraction of the coupling impedance in overmoded cavities," *Wave Motion,* vol. 87, pp. 123 - 131, 2019.

[56] J. Hart, A.; Antonsen, T., M.; Ott, E., "Effect of short ray trajectories on the scattering statistics of wave chaotic systems," *Physical Review E,* vol. 80, no. 4, pp. 041109(1-15), 2009.

[57] J.-H. H. Yeh, James, A.; Bradshaw, Elliott; Antonsen, Thomas, M.; Ott, Edward; Anlage, Steven, M., "Experimental examination of the effect of short ray trajectories in two-port wave-chaotic scattering systems," *Phys. Rev. E,* vol. 82, no. 4, p. 041114, 2010, doi: 10.1103/PhysRevE.82.041114.

[58] X. Zheng, T. M. Antonsen, and E. Ott, "Statistics of Impedance and Scattering Matrices of Chaotic Microwave Cavities with Multiple Ports," *Electromagnetics,* vol. 26, no. 1, pp. 37-55, 2006/01/01 2006, doi: 10.1080/02726340500214902.

[59] B. A. Xiao, Thomas, M.; Ott, Edward; Anlage, Steven, "Focusing waves at arbitrary locations in a ray-chaotic enclosure using time-reversed synthetic sonas," *Phys. Rev. E,* vol. 93, no. 5, p. 052205, 2016, doi: 10.1103/PhysRevE.93.052205.

[60] D. E. Goldberg and J. H. Holland, "Genetic Algorithms and Machine Learning," *Machine Learning,* vol. 3, no. 2, pp. 95 - 99, 1988.

[61] J. H. Holland. (1992) Genetic Algortihms. *Scientific American*.

[62] R. L. Haupt, "An Introduction to Genetic Algorithms for Electromagnetics," *IEEE Antennas and Propagation Magazine*, vol. 37, no. 2, pp. 7 - 15, 1995.

[63] R. L. Haupt and D. H. Werner, *Genetic Algorithms in Electromagnetics*. Hoboken, NJ: John Wiley & Sons, Inc., 2007.

[64] R. L. Haupt, J. J. Menozzi, and C. J. McCormack, "Thinned Arrays Using Genetic Algorothms," USAF Academy, Department of Electrical Engineering.

[65] M. J. Johnson and Y. Rahmat-Samii, "Genetic Algorithms in Engineering Electromagnetics," *IEEE Antennas and Propagation Magazine,* vol. 39, no. 4, pp. 7 - 21, 1997.